AutoCloud+, a "universal" physical and statistical model-based 2D spatial topology-preserving software toolbox for cloud/cloud-shadow detection in multi-sensor single-date Earth observation multi-spectral imagery eligible for systematic ESA EO Level 2 product generation

Andrea Baraldi [1,2,*] and Dirk Tiede [1]

[1] Department of Geoinformatics – Z_GIS, University of Salzburg, Schillerstr. 30, 5020 Salzburg, Austria; dirk.tiede@sbg.ac.at

[2] Italian Space Agency (ASI), Via del Politecnico, 00133 Rome RM, Italy.

* Correspondence: andrea6311@gmail.com; Tel.: +39-329-2648110

Abstract: The European Space Agency (ESA) defines as Earth observation (EO) Level 2 information product a single-date multi-spectral (MS) image corrected for atmospheric, adjacency and topographic effects, stacked with its data-derived scene classification map (SCM), whose thematic map legend includes quality layers cloud and cloud-shadow. ESA EO Level 2 product generation is an inherently ill-posed computer vision (CV) problem never accomplished to date in operating mode by any EO data provider at the ground segment. Herein, it is considered: (I) necessary not sufficient pre-condition for the yet-unaccomplished dependent problems of semantic content-based image retrieval (SCBIR) and semantics-enabled information/knowledge discovery (SEIKD) in multi-source EO *big data* cubes. (II) Synonym of EO Analysis Ready Data (ARD) format. (III) Equivalent to a horizontal policy for background developments in Space Economy 4.0. In compliance with the GEO-CEOS Quality Assurance Framework for EO Calibration/Validation guidelines, to contribute toward filling an analytic and pragmatic information gap from multi-sensor EO *big data* to timely, comprehensive and operational EO value-adding information products and services, this work presents an innovative AutoCloud+ CV software toolbox for cloud and cloud-shadow quality layer detection in ESA EO Level 2 product. In vision, spatial information dominates color information. Inspired by this true-fact, the inherently ill-posed AutoCloud+ CV software was conditioned, designed and implemented to be "universal", meaning fully automated (no human-machine interaction is required), near real-time, robust to changes in input data and scalable to changes in MS imaging sensor's spatial and spectral resolution specifications.

Keywords: artificial intelligence; color naming; color constancy; cognitive science; computer vision; object-based image analysis (OBIA); physical and statistical data models; radiometric calibration; semantic content-based image retrieval; spatial topological and spatial non-topological information components.

44   **Acronyms**

45   AI: Artificial Intelligence
46   AI4DIAS: Artificial Intelligence for Data and Information Access Services (at the ground
47   segment)
48   AI4Space: Artificial Intelligence for Space (segment)
49   ARD: Analysis Ready Data (format)
50   ATCOR: Atmospheric/Topographic Correction commercial sofwtare product
51   AVHRR: Advanced Very High Resolution Radiometer
52   BC: Basic Color
53   BIVRFTAB: Bivariate Frequency Table
54   Cal: Calibration
55   Cal/Val: Calibration and Validation
56   CBIR: Content-Based Image Retrieval
57   CEOS: Committee on Earth Observation Satellites
58   CESBIO: Centre d'Etudes Spatiales de la Biosphère
59   CFMask: C (programming language version of) Function of Mask
60   CLC: CORINE Land Cover (taxonomy)
61   CNES: Centre national d'études spatiales
62   CNN: Convolutional Neural Network
63   CORINE: Coordination of Information on the Environment
64   CV: Computer Vision
65   DCNN: Deep Convolutional Neural Network
66   DEM: Digital Elevation Model
67   DIAS: Data and Information Access Services
68   DLR: Deutsches Zentrum für Luft- und Raumfahrt (German Aerospace Center)
69   DN: Digital Number
70   DP: Dichotomous Phase (in the FAO LCCS taxonomy)
71   DRIP: Data-Rich, Information-Poor (syndrome)
72   EO: Earth Observation
73   EO-IU: EO Image Understanding
74   EO-IU4SQ: EO Image Understanding for Semantic Querying
75   ESA: European Space Agency
76   FAO: Food and Agriculture Organization
77   FIEOS: Future Intelligent EO imaging Satellites
78   FMask: Function of Mask
79   GEO: Intergovernmental Group on Earth Observations
80   GEOSS: Global EO System of Systems
81   GIGO: Garbage In, Garbage Out principle of error propagation
82   GIS: Geographic Information System
83   GIScience: Geographic Information Science
84   GUI: Graphic User Interface
85   IGBP: International Global Biosphere Programme
86   IU: Image Understanding
87   LAI: Leaf Area Index
88   LC: Land Cover
89   LCC: Land Cover Change
90   LCCS: Land Cover Classification System (taxonomy)
91   LCLU: Land Cover Land Use
92   LEDAPS: Landsat Ecosystem Disturbance Adaptive Processing System
93   MAACS: Multisensor Atmospheric Correction and Cloud Screening
94   MAJA: Multisensor Atmospheric Correction and Cloud Screening (MACCS)-
95   Atmospheric/Topographic Correction (ATCOR) Joint Algorithm

96   mDMI: Minimally Dependent and Maximally Informative (set of quality indicators)
97   MHP: Modular Hierarchical Phase (in the FAO LCCS taxonomy)
98   MIR: Medium InfraRed
99   MODIS: Moderate Resolution Imaging Spectroradiometer
100   MS: Multi-Spectral
101   MSI: (Sentinel-2) Multi-Spectral Instrument
102   NASA: National Aeronautics and Space Administration
103   NIR: Near InfraRed
104   NLCD: National Land Cover Data
105   NOAA: National Oceanic and Atmospheric Administration
106   NP: Non-Polynomial
107   OBIA: Object-Based Image Analysis
108   OGC: Open Geospatial Consortium
109   OP: Outcome (product) and Process
110   OP-Q^{2}I: Outcome and Process Quantitative Quality Index
111   QA4EO: Quality Accuracy Framework for Earth Observation
112   Q^{2}I: Quantitative Quality Indicator
113   RGB: monitor-typical Red-Green-Blue data cube
114   RMSE: Root Mean Square Error
115   RS: Remote Sensing
116   RTD: Research and Technological Development
117   SCBIR: Semantic Content-Based Image Retrieval
118   SCM: Scene Classification Map
119   SEIKD: Semantics-Enabled Information/Knowledge Discovery
120   Sen2Cor: Sentinel 2 (atmospheric) Correction Prototype Processor
121   SIAM™: Satellite Image Automatic Mapper™
122   STRATCOR: Stratified Topographic Correction
123   SURF: Surface Reflectance
124   TIR: Thermal InfraRed
125   TM (superscript): (non-registered) Trademark
126   TMask: Temporal Function of Mask
127   TOA: Top-Of-Atmosphere
128   TOARF: TOA Reflectance
129   UAV: Unmanned Aerial Vehicle
130   UML: Unified Modeling Language
131   USGS: US Geological Survey
132   Val: Validation
133   VAPS: Value-Adding information Products and Services
134   VQ: Vector Quantization
135   WGCV: Working Group on Calibration and Validation

136   **1. Introduction**

137   Radiometric calibration (*Cal*) is the process of transforming remote sensing (RS) sensory
138   data, consisting of non-negative dimensionless digital numbers (DNs, with DN ≥ 0) provided
139   with no physical meaning, into a physical variable provided with a community-agreed
140   radiometric unit of measure, such as top-of-atmosphere reflectance (TOARF), surface
141   reflectance (SURF) or surface albedo values in range [0, 1] [1-3].
142   To cope with the five Vs characterizing *big data* analytics, specifically, volume, variety,
143   veracity, velocity and value [4], radiometric *Cal* of Earth observation (EO) *big data* is considered
144   mandatory by the intergovernmental Group on Earth Observations (GEO)-Committee on
145   Earth Observation Satellites (CEOS) Quality Accuracy Framework for Earth Observation
146   (QA4EO) Calibration/Validation (*Cal/Val*) guidelines [3]. In agreement with the yet-

147   unaccomplished visionary goal of a GEO's implementation plan for years 2005-2015 of a Global
148   Earth Observation System of Systems (GEOSS) [5], the ambitious goal of the GEO-CEOS
149   QA4EO *Cal/Val* guidelines is systematic transformation of EO *big data* cubes into timely,
150   comprehensive and operational EO value-adding information products and services (VAPS).
151   Despite being considered a well-known "prerequisite for physical model-based analysis of
152   airborne and satellite sensor measurements in the optical domain" [1], EO data radiometric *Cal*
153   is largely oversighted in the RS common practice. A lack of EO input data *Cal* requirements
154   means that statistical model-based data analytics and inductive learning-from-data algorithms
155   are dominant in the RS community, including (geographic) object-based image analysis
156   (GEOBIA) applications [6, 7] in the domain of geographic information science (GIScience). On
157   the one hand, statistical model-based and inductive learning-from-data algorithms require as
158   input DNs provided with no physical meaning. On the other hand, inductive learning-from-
159   data algorithms are inherently semi-automatic and site-specific [2]. In practice, they require no
160   radiometric *Cal* data pre-processing, but they typically gain in robustness when input with
161   radiometrically calibrated data.
162   In compliance with the GEO-CEOS QA4EO *Cal/Val* requirements and with the GEO's
163   visionary goal of a GEOSS, the European Space Agency (ESA) has recently defined an ESA EO
164   Level 2 information product as follows [8, 9].
165   (i)   A single-date multi-spectral (MS) image, radiometrically corrected for atmospheric,
166   adjacency and topographic effects,
167   (ii)   stacked with its data-derived scene classification map (SCM), whose general-purpose,
168   user- and application-independent thematic map legend includes quality layers cloud and
169   cloud-shadow,
170   (iii)   to be systematically generated at the ground segment, automatically (without human-
171   machine interaction) and in near real-time.
172   Unlike the non-standard ESA EO Level 2 SCM legend adopted by the Sentinel 2 imaging
173   sensor-specific (atmospheric, adjacency and topographic) Correction Prototype Processor
174   (Sen2Cor), developed by ESA and distributed free-of-cost to be run on user side [8, 9], see Table
175   1, an alternative ESA EO Level 2 SCM legend proposed in [10-12], shown in Table 2, is selected
176   equal to an "augmented" 3-level 9-class Dichotomous Phase (DP) taxonomy of the Food and
177   Agriculture Organization of the United Nations (FAO) – Land Cover Classification System
178   (LCCS) [13], see Figure 1. Such an "augmented" land cover (LC) class taxonomy in the 4D
179   geospatial-temporal scene-domain encompasses the standard fully-nested 3-level 8-class FAO
180   LCCS-DP legend, , see Figure 1, in addition to a thematic layer "other" or "rest of the world",
181   which includes quality layers cloud and cloud-shadow. In traditional EO image classification
182   system design and implementation requirements [14], the presence of output class "unknown"
183   is considered mandatory to cope with uncertainty in inherently equivocal *information-as-data-*
184   *interpretation* (classification) tasks [15].
185
186   **Table 1.** Non-standard general-purpose, user- and application-independent ESA EO Level 2
187   SCM legend adopted by the sensor-specific Sentinel 2 (atmospheric, adjacency and
188   topographic) Correction (Sen2Cor) Prototype Processor [8, 9], developed and distributed free-
189   of-cost by ESA to be run on user side.

Label	Classification
0	NO_DATA
1	SATURATED_OR_DEFECTIVE
2	DARK_AREA_PIXELS
3	CLOUD_SHADOWS
4	VEGETATION
5	BARE_SOILS
6	WATER
7	CLOUD_LOW_PROBABILITY
8	CLOUD_MEDIUM_PROBABILITY
9	CLOUD_HIGH_PROBABILITY
10	THIN_CIRRUS
11	SNOW

190
191
192   **Table 2.** Standard general-purpose, user- and application-independent ESA Level 2 SCM
193   legend proposed in [10-12]. "Augmented" 3-level 8-class FAO LCCS Dichotomous Phase (DP)
194   taxonomy (identified as classes A11 to B48) + quality layers Cloud and Cloud-shadow + Others
195   = 8 land cover (LC) classes + 2 LC classes (Cloud-shadow, Others) + 1 non-LC class (Cloud).

Pseudocolor

A11	1.	Cultivated and Managed Terrestrial (non-aquatic) Vegetated Areas
A12	2.	Natural and Semi-Natural Terrestrial Vegetation
A23	3.	Cultivated Aquatic or Regularly Flooded Vegetated Areas
A24	4.	Natural and Semi-Natural Aquatic or Regularly Flooded Vegetation
B35	5.	Artificial Surfaces and Associated Areas
B36	6.	Bare Areas
B47	7.	Artificial Waterbodies, Snow and Ice
B48	8.	Natural Waterbodies, Snow and Ice.
	9.	Quality layer: Cloud
	10.	Quality layer: Cloud-shadow
	11.	Others

196
197
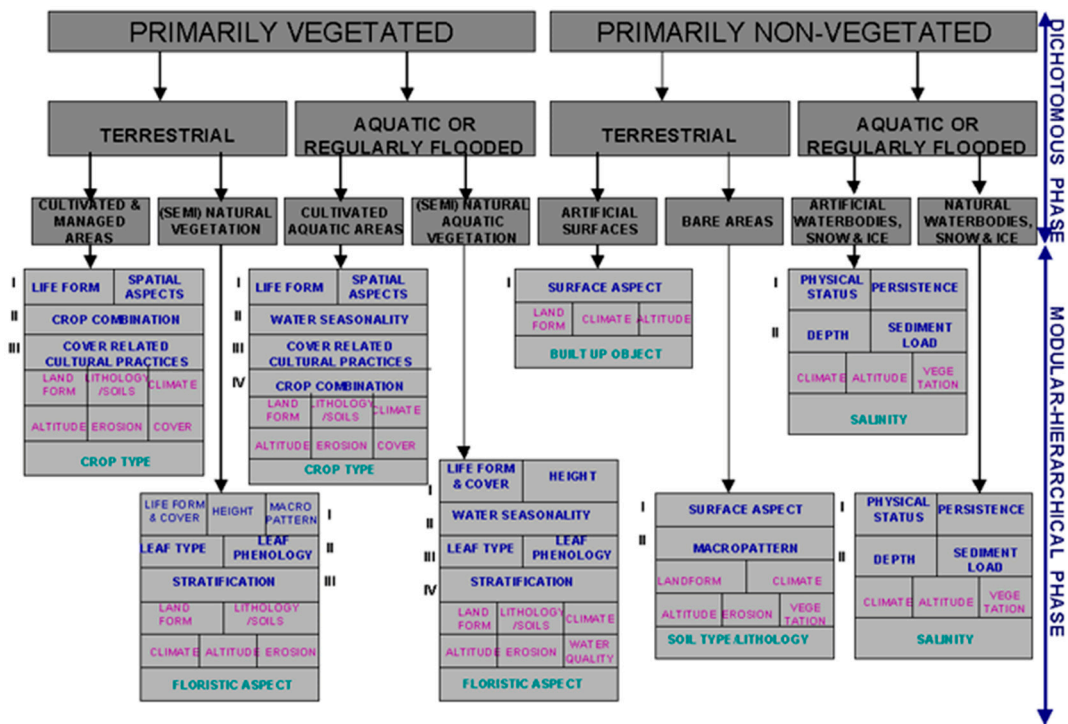
Figure 1. Two-stage fully-nested FAO Land Cover Classification System (LCCS) taxonomy [13]. The first-stage fully-nested 3-level 8-class FAO LCCS Dichotomous Phase (DP) taxonomy is general-purpose, user- and application-independent. It consists of a sorted set of 3 dichotomous layers: (i) vegetation versus non-vegetation, (ii) terrestrial versus aquatic, and (iii) managed versus natural or semi-natural. These 3 dichotomous layers deliver as output the following 8-class FAO LCCS-DP taxonomy. (A11) Cultivated and Managed Terrestrial (non-aquatic) Vegetated Areas. (A12) Natural and Semi-Natural Terrestrial Vegetation. (A23) Cultivated Aquatic or Regularly Flooded Vegetated Areas. (A24) Natural and Semi-Natural Aquatic or Regularly Flooded Vegetation. (B35) Artificial Surfaces and Associated Areas. (B36) Bare Areas. (B47) Artificial Waterbodies, Snow and Ice. (B48) Natural Waterbodies, Snow and Ice. The general-purpose user- and application-independent 3-level 8-class FAO LCCS-DP taxonomy is preliminary to a second-stage FAO LCCS Modular Hierarchical Phase (MHP) taxonomy, consisting of a battery of user- and application-specific one-class classifiers, equivalent to one-class grammars (syntactic classifiers) [16].

Shown in Figure 1, the standard two-phase fully-nested FAO LCCS hierarchy consists a first-stage fully-nested general-purpose, user- and application-independent 3-level 8-class FAO LCCS-DP legend, preliminary to a second-stage application-dependent and user-specific FAO LCCS Modular Hierarchical Phase (MHP) taxonomy, consisting of a hierarchical (deep) battery of one-class classifiers [13]. The standard first-stage 3-level 8-class FAO LCCS-DP hierarchy is "fully nested". It comprises three dichotomous LC class-specific information layers, equivalent to a world ontology, world model or mental model of the world [10, 13, 16-21]: DP Level 1 – Vegetation versus non-vegetation, DP Level 2 – Terrestrial versus aquatic and DP Level 3 – Managed versus natural or semi-natural. In recent years, the two-phase FAO LCCS taxonomy has become increasingly popular [22]. One reason of its popularity is that the FAO LCCS hierarchy is "fully nested" while alternative LC class hierarchies, such as the Coordination of Information on the Environment (CORINE) Land Cover (CLC) taxomony [23], the U.S. Geological Survey (USGS) Land Cover Land Use (LCLU) taxonomy by J. Anderson [24], the International Global Biosphere Programme (IGBP) DISCover Data Set Land Cover Classification System [25] and the EO Image Librarian LC class legend [26], start from a Level 1 taxonomy which is already multi-class. In a hierarchical EO image understanding (EO-IU) system architecture submitted to a garbage in, garbage out (GIGO) information principle,

229   synonym of error propagation through an information processing chain, the fully-nested two-
230   phase FAO LCCS hierarchy makes explicit the full dependence of high-level LC class estimates,
231   performed by any high-level (deep) LCCS-MHP data processing module, on the operational
232   quality (in accuracy, efficiency, robustness, etc.) of lower-level LCCS modules, starting from
233   the initial FAO LCCS-DP Level 1 vegetation/non-vegetation information layer whose relevance
234   in thematic mapping accuracy (vice versa, in error propagation) becomes paramount for all
235   subsequent LCCS layers. The GIGO commonsense principle applied to hierarchical semantic
236   dependence is neither trivial nor obvious to underline [27]. On the one hand, it agrees with a
237   minor portion of the RS literature where supervised data learning classification of EO image
238   datasets at continental or global spatial extent into binary LC class vegetation/non-vegetation
239   is considered very challenging [28]. On the other hand, it is at odd with the RS mainstream,
240   where the semantic information gap from sub-symbolic EO data to multi-class LC taxonomies
241   is typically filled in one step, implemented as a supervised data learning classifier [29, 30], e.g.,
242   a support vector machine, random forest or deep convolutional neural network (DCNN) [31],
243   which is equivalent to an unstructured black box [27], inherently semi-automatic and site-
244   specific [2] and whose opacity contradicts the well-known engineering principles of
245   modularity, regularity and hierarchy typical of scalable systems [32]. "No Free Lunch"
246   theorems have shown that inductive learning-from-data algorithms cannot be universally
247   good [33, 34].
248   Over land surfaces of the Earth, the global cloud cover is approximately 66% [35]. In the
249   ESA EO Level 2 product definition, cloud and cloud-shadow quality layer requirements
250   specification accounts for a well-known prerequisite of clear-sky multi-temporal EO image
251   compositing and understanding (classification) solutions proposed by the RS community,
252   where accurate masking of cloud and cloud-shadow phenomena is considered necessary not
253   sufficient pre-condition [9, 10, 36-56]. Intuitively, in single-date and multi-temporal MS image
254   analysis, cloud and cloud-shadow preliminary detection is a relevant problem, because
255   unflagged cloud and cloud-shadow phenomena may be mapped onto erroneous LC classes or
256   false LC change (LCC) occurrences. Noteworthy, cloud/cloud-shadow detection is a typical
257   example of physical model-based cause-effect relationship, expected to be very difficult to
258   solve by inductive machine learning-from-data algorithms, such as increasingly popular
259   DCNNs [31], suitable for learning complex correlations between input and output features, but
260   capable of no inherent representation of causality [27, 57], in agreement with the well-known
261   dictum that correlation does not imply causation and vice versa [10, 16, 27, 30, 57, 58].
262   In the last decade, many different cloud/cloud-shadow detection algorithms were
263   presented in the RS literature to run either on a single-date MS image or on an MS image time-
264   series, typically acquired by either one EO spaceborne/airborne MS imaging sensor or a single
265   family (e.g., Landsat) of MS imaging sensors [9, 10, 36-53]. To be accomplished in operating
266   mode at the ground segment (midstream) by EO data providers in support of the downstream
267   sector in an era of Space Economy 4.0 [59], systematic radiometric *Cal* of multi-source multi-
268   angular MS big image data cubes [1, 3, 10, 60-62], encompassing either single-date or multi-
269   temporal cloud and cloud-shadow detection as a necessary not sufficient pre-condition, is
270   regarded by the RS community as an open problem to date [54-56].
271   To overcome conceptual limitations and well-known failure modes of existing cloud and
272   cloud-shadow detection algorithms [37, 40, 54-56], such as the single-date open source
273   Function of Mask (FMask) algorithm [51, 52], the free-of-cost single-date ESA Sen2Cor software
274   toolbox to be run on user side [8, 9, 37] and the multi-date Multisensor Atmospheric Correction
275   and Cloud Screening (MACCS)-Atmospheric/Topographic Correction (ATCOR) Joint
276   Algorithm (MAJA) developed by the Centre national d'études spatiales (CNES)/ Centre
277   d'Etudes Spatiales de la Biosphère (CESBIO)/ Deutsches Zentrum für Luft- und Raumfahrt
278   (German Aerospace Center, DLR) [39-41], which incorporates capabilities of the ATCOR
279   commercial software toolbox [63-66], this work presents an innovative AutoCloud+ computer
280   vision (CV) software toolbox for cloud and cloud-shadow quality layer detection, suitable for

281 systematic ESA EO Level 2 product generation at the ground segment [36, 60, 67]), in
282 compliance with the GEO-CEOS QA4EO *Cal/Val* requirements [3].
283   Synonym of inherently ill-posed scene-from-image reconstruction and understanding [10,
284 20, 68, 69]), vision is a cognitive (*information-as-data-interpretation*) process [15], encompassing
285 both biological vision and CV, where CV is *subset-of* artificial (general) intelligence (AI) [70-74],
286 i.e., AI ⊃ CV. In vision, spatial information dominates color information [20]. This
287 unquestionable true-fact is familiar to all human beings wearing sunglasses: in perceptual
288 terms, human panchromatic and chromatic visions are nearly as effective [10]. Based on this
289 observation, an inherently ill-posed AutoCloud+ CV subsystem was constrained, designed and
290 implemented to be "universal" in operating mode, i.e., automated (no human-machine
291 interaction is required to run), near real-time, robust to changes in input data and scalable to
292 cope with changes in MS imaging sensor's spatial and spectral resolution specifications.
293   The rest of this paper is organized as follows. Provided with a relevant survey value,
294 Section 2 reviews the interdisciplinary problem background of systematic ESA EO Level 2
295 product generation, regarded as necessary not sufficient pre-condition for a yet-
296 unaccomplished GEOSS development. Related works in cloud/cloud-shadow detection are
297 critically revised in Section 3. Adopted AutoCloud+ methods and materials are proposed in
298 Section 4 and 5 respectively. Collected results are presented in Section 6 and discussed in
299 Section 7. Conclusions are reported in Section 8.

300 **2. Problem background**

301   Featuring a relevant survey value, this Section aims at providing a critical review of the
302 interdisciplinary problem background of systematic ESA EO Level 2 product generation,
303 regarded as necessary not sufficient pre-condition for a yet-unaccomplished GEOSS
304 development, in agreement with the GEO-CEOS QA4EO *Cal/Val* requirements [3]. In this
305 critical review, our second original contribution highlights the several degrees of novelty of
306 the ESA EO Level 2 product definition (refer to Section 1) in comparison with, for example,
307 alternative EO Analysis Ready Data (ARD) format definitions proposed by the RS community.
308 Next, structural limitations in system design of existing open source or commercial software
309 products for EO image radiometric correction are underlined, to be overcome by an alternative
310 solution as our third original contribution.
311
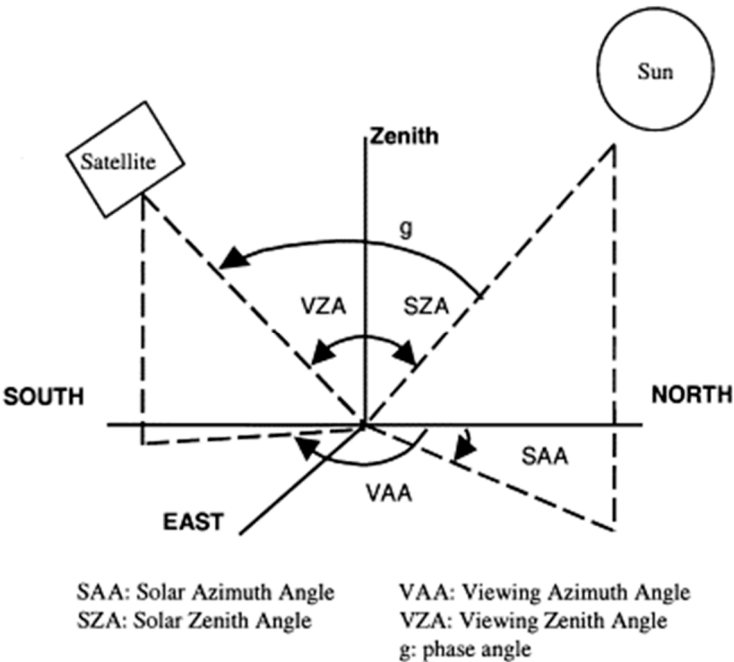
312 **Figure 2.** Solar illumination geometries and viewpoint geometries in spaceborne and airborne
313   EO image acquisition.

314   To successfully cope with the five Vs of EO *big data* analytics, specifically, volume, variety,
315   veracity, velocity and value [4], multi-sensor analysis of multi-temporal multi-angular EO
316   sensory data cubes depends upon the ability to distinguish between relevant changes and no-
317   changes occurring at the Earth surface through time [61, 62]. Necessary not sufficient pre-
318   condition for EO *big data* transformation into timely, comprehensive and operational EO data-
319   derived VAPS, expected by GEO to be pursued by a GEOSS never accomplished to date [5], is
320   radiometric *Cal*, considered mandatory by the GEO-CEOS QA4EO *Cal/Val* requirements [3]. In
321   short, radiometric *Cal* guarantees EO sensory data interoperability (consistency,
322   "normalization") through time, geographic space and sensors. In greater detail, the capability
323   to detect and quantify change/no-change in terms of either qualitative (nominal, categorical)
324   Earth surface variables, such as LC classes belonging to a finite and discrete LC class taxonomy
325   (legend), or quantitative (numeric) Earth surface variables, such as biophysical variables, e.g.,
326   leaf area index (LAI), biomass, etc. [75], depends on the radiometric *Cal* of EO sensory data,
327   equivalent to non-negative dimensionless DNs ≥ 0, provided with no physical meaning and
328   typically affected at sensor-level by ever-varying atmospheric conditions, solar illumination
329   conditions, spaceborne/airborne viewing geometries and Earth surface topography, into a
330   physical variable provided with a community-agreed radiometric unit of measure, such as
331   SURF or surface albedo values in range [0, 1] [1-3]. Solar illumination conditions are typically
332   parameterized by metadata *Cal* parameters, such as image acquisition time, solar
333   exoatmospheric irradiance, solar zenith angle and solar azimuth angle, see Figure 2. Sensor
334   viewing characteristics are typical metadata *Cal* parameters, such as sensor zenith angle and
335   sensor azimuth angle, see Figure 2. Atmospheric conditions are described by categorical
336   variables, such as aerosol type, haze, cloud and cloud-shadow, and by numeric variables, such
337   as water vapor, temperature and aerosol optical thickness (AOT) [61, 62]. Finally, Earth surface
338   geometries must be inferred from ancillary data, such as a digital elevation model (DEM), in
339   combination with solar and viewing conditions [76], see Figure 2.
340   Adopted by different scientific disciplines, such as machine learning-from-data [30], AI as
341   *superset-of* CV [70], i.e., AI $\supset$ CV, and RS [2, 10], popular synonyms of deductive inference are
342   top-down inference, prior knowledge-based inference, learning-by-rule inference and physical
343   model-based inference. Synonyms of inductive inference are bottom-up inference, learning-
344   from-data inference, learning-from-examples inference and statistical model-based inference.
345   On the one hand, non-calibrated sensory data, provided with no physical meaning, can
346   be investigated by statistical data models and inductive inference algorithms, exclusively. On
347   the other hand, although they do not require physical variables as input, statistical data models
348   and inductive learning-from-data algorithms can benefit from input data *Cal* in terms of
349   augmented robustness to changes in the input data set acquired through time, space and
350   sensors. On the contrary, radiometrically calibrated data, provided with a physical meaning,
351   can be interpreted by either inductive, deductive (physical model-based) or hybrid (combined
352   deductive and inductive) inference algorithms. Although it is considered a well-known
353   "prerequisite for physical model-based (and hybrid) analysis of airborne and satellite sensor
354   measurements in the optical domain" [1, 10, 60-62], EO data *Cal* is largely neglected in the RS
355   common practice. For example, in major portions of the RS literature, including the GEOBIA
356   sub-domain of GIScience [6, 7], no reference to radiometric *Cal* issues is found. This lack of
357   input EO data *Cal* requirements proves that, to date, EO image analytics mainly consists of
358   inductive learning-from-data algorithms, starting from scratch because no *a priori* physical
359   knowledge is exploited in addition to data. This is in contrast with biological cognitive systems,
360   where "there is never an absolute beginning" [77], because *a priori* genotype provides initial
361   conditions (that reflect properties of the world, embodied through evolution, based on
362   evolutionary experience) to learning-from-examples phenotype, according to a hybrid
363   inference paradigm, where phenotype explores the neighborhood of genotype in a solution
364   space [10, 71]. Hybrid inference combines deductive and inductive inference to take advantage
365   of each and overcome their shortcomings [2]. Inductive inference is typically semi-automatic

366 and site-specific [2]. Deductive inference is static (non-adaptive to data) and typically lacks
367 flexibility to transform ever-varying sensory data (sensations) into stable percepts (concepts)
368 in a world model [10, 20, 78, 79].
369   In compliance with the GEO-CEOS QA4EO *Cal/Val* requirements and the visionary goal
370 of a GEOSS ([5]), ESA has recently provided an original ESA EO Level 2 information product
371 definition, refer to Section 1 [8, 9]. The ESA EO Level 2 product definition is non-trivial.
372 Noteworthy, it is more restrictive than the National Aeronautics and Space Administration
373 (NASA) EO Level 2 product definition of "a data-derived geophysical variable at the same
374 resolution and location as Level 1 source data" [80]. According to the standard Unified
375 Modeling Language (UML) for graphical modeling of object-oriented software [81], where
376 symbol '→' denotes relationship *part-of* pointing from the supplier to the client (vice versa, it
377 would denote relationship *depend-on*), not to be confused with relationship *subset-of*, whose
378 symbol is '⊃', meaning specialization with inheritance from the superset to the subset,
379 dependence relationship 'NASA EO Level 2 product → ESA EO Level 2 product' holds true,
380 see Figure 3. It means that a NASA EO Level 2 product can be accomplished although no ESA
381 EO Level 2 product exists, whereas the vice versa does not hold.
382
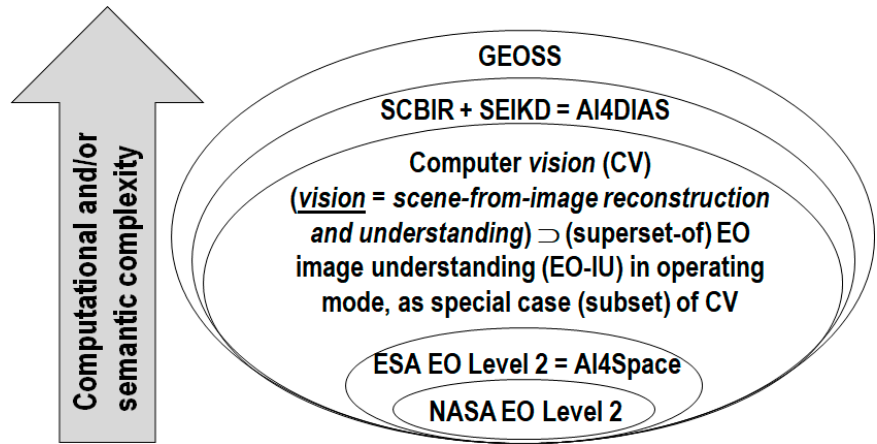
383 **Figure 3.** In agreement with the standard Unified Modeling Language (UML) for graphical
384 modeling of object-oriented software ([81]), relationship *part-of*, denoted with symbol '→'
385 pointing from the supplier to the client, should not to be confused with relationship *subset-of*,
386 '⊃', meaning specialization with inheritance from the superset to the subset [81]. A NASA EO
387 Level 2 product is defined as "a data-derived geophysical variable at the same resolution and
388 location as Level 1 source data" [80]. Herein, it is considered *part-of* an ESA EO Level 2 product
389 defined as [8, 9]: (a) a single-date multi-spectral (MS) image whose digital numbers (DNs) are
390 radiometrically corrected into surface reflectance (SURF) values for atmospheric, adjacency
391 and topographic effects, stacked with (b) its data-derived general-purpose, user- and
392 application-independent scene classification map (SCM), whose thematic map legend includes
393 quality layers cloud and cloud-shadow. In this paper, ESA EO Level 2 product is regarded as
394 an information primitive to be accomplished by Artificial Intelligence for the Space segment
395 (AI4Space), such as in future intelligent small satellite constellations, rather than at the ground
396 segment in an AI for data and information access services (AI4DIAS) framework. In this
397 graphical representation, additional acronyms of interest are computer vision (CV), whose
398 special case is EO image understanding (EO-IU) in operating mode, semantic content-based
399 image retrieval (SCBIR) [10, 82-87], semantics-enabled information/knowledge discovery
400 (SEIKD), where SCIR + SEIKD is considered synonym of AI4DIAS, and Global Earth
401 Observation System of Systems (GEOSS), defined by the Group on Earth Observations [5]. Our
402 working hypothesis postulates that 'NASA EO Level 2 product → ESA EO Level 2 product =
403 AI4Space ⊂ EO-IU in operating mode ⊂ CV → [EO-SCBIR + SEIKD = AI4DIAS] → GEOSS'. It
404 means that GEOSS, whose *part-of* are the still-unsolved (open) problems of SCBIR and SEIKD,
405 cannot be achieved until the necessary not sufficient pre-condition of CV in operating mode,
406 specifically, systematic ESA EO Level 2 product generation, is accomplished in advance.

407 Encompassing both biological vision and CV, vision is synonym of scene-from-image
408 reconstruction and understanding. Vision is a cognitive *(information-as-data-interpretation)*
409 problem [15] very difficult to solve because: (i) non-polynomial (NP)-hard in computational
410 complexity [88, 89], (ii) inherently ill-posed in the Hadamard sense [90], i.e., vision admits no
411 solution, multiple solutions or, if the solution exists, the solution's behavior changes
412 continuously with the initial conditions [20, 68]. Vision is inherently ill-posed because affected
413 by: (I) a 4D-to-2D data dimensionality reduction from the scene-domain to the image-domain,
414 e.g., responsible of occlusion phenomena, and (II) a semantic information gap from ever-
415 varying sub-symbolic sensory data (sensations) in the physical world to stable symbolic
416 percepts in the mental model of the physical world (modeled world, world ontology, world
417 model) [10, 16-21]. Since it is inherently ill-posed, vision requires *a priori* knowledge in addition
418 to sensory data to become better posed for numerical solution [30]. If the aforementioned
419 working hypothesis holds true, then the complexity of SCBIR + SEIKD is not inferior to the
420 complexity of vision, acknowledged to be inherently ill-posed and NP-hard. To make the
421 inherently-ill-posed CV problem better conditioned for numerical solution, a CV system is
422 required to comply with human visual perception. In other words, a CV system is constrained
423 to include a computational model of human vision, i.e., 'Human vision → CV'. Hence,
424 dependence relationship: 'Human vision → CV ⊃ EO-IU in operating mode ⊃ NASA EO Level
425 2 product → ESA EO Level 2 product → [EO-SCBIR + SEIKD = AI4DIAS] → GEOSS' is our
426 working hypothesis.

427 An improved ("augmented") and more restrictive ESA EO Level 2 product definition
428 could be defined to account for bidirectional reflectance distribution function (BRDF) effect
429 correction, in addition to atmospheric, topographic and adjacency effects correction, to model
430 surface anisotropy in multi-temporal multi-angular EO image data cubes [2, 61, 62, 66, 91-94].
431 A surface that reflects the incident energy equally in all directions is said to be Lambertian,
432 where reflectance is invariant with respect to illumination and viewing conditions, see Figure
433 2. On the contrary, a surface is said to be anisotropic when its reflectance varies with respect
434 to illumination and/or viewing geometries. These changes are driven by the optical and
435 structural properties of the surface material. In other words, in EO image pre-processing
436 (enhancement) for radiometric *Cal*, BRDF effect correction is LC class-specific [61, 62, 66, 91-
437 94]. The LC class-specific task of BRDF correction is to derive, for non-Lambertian surfaces,
438 spectral albedo (bi-hemispherical reflectance, BHR) values, defined over all directions [2, 66,
439 91-94], from either SURF or TOARF values where the Lambertian surface assumption holds
440 [63-66, 91].
441 Our first original contribution is to consider an ESA EO Level 2 information product a
442 baseline information unit (information primitive) whose systematic generation is of
443 paramount importance to contribute toward filling an analytic and pragmatic information gap
444 from multi-sensor, multi-temporal and multi-angular EO *big image data cubes* into timely,
445 comprehensive and operational EO data-derived VAPS, in compliance with the yet-
446 unaccomplished visionary goal of a GEOSS [3, 5]. In Figure 3, our working hypothesis
447 postulates that systematic ESA EO Level 2 product generation is an inherently ill-posed CV
448 problem, where CV ⊃ EO-IU, whose solution in operating mode is necessary not sufficient pre-
449 condition for the yet-unaccomplished dependent problems of semantic content-based image
450 retrieval (SCBIR) [10, 82-87] and semantics-enabled information/knowledge discovery (SEIKD)
451 in large-scale EO image data cubes, with SCBIR + SEIKD considered synonym of artificial
452 intelligence for data and information access services (AI4DIAS), where AI4DIAS is *part-of* a
453 yet-unaccomplished GEOSS. The closed-loop AI4DIAS system architecture, suitable for
454 semantics-enabled incremental learning [10, 87], is sketched in Figure 4 [10].
455
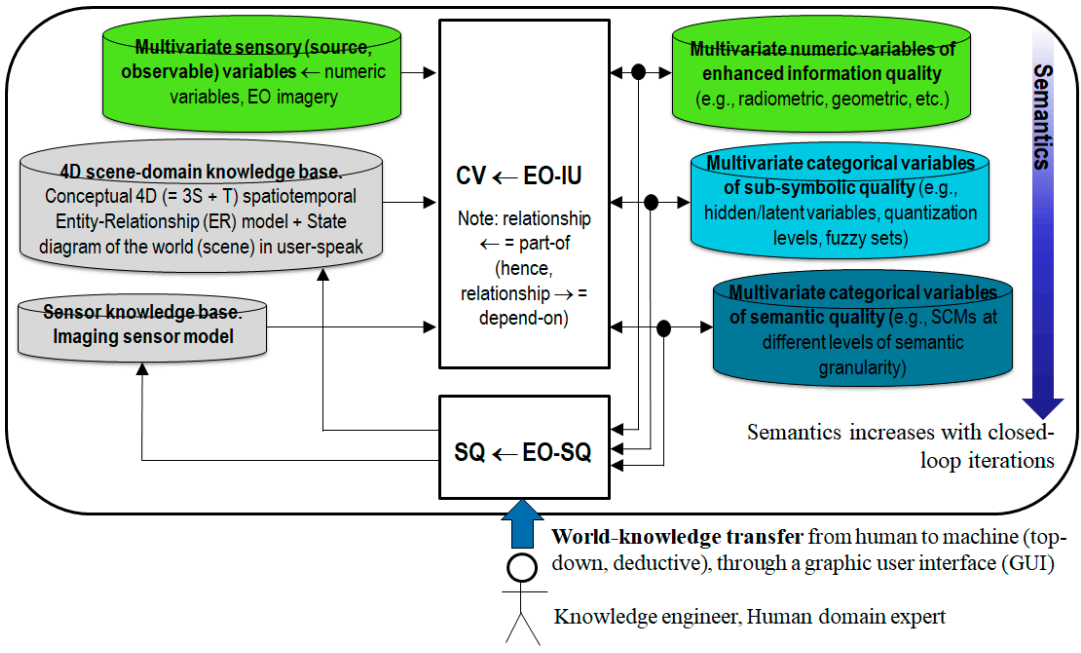
Figure 4. Artificial intelligence (AI) for data and information access services (AI4DIAS), synonym of semantics-enabled DIAS or closed-loop EO image understanding (EO-IU) for semantic querying (EO-IU4SQ) system architecture. At the Marr level of system understanding known as system design (architecture) [69], AI4DIAS is sketched as a closed-loop EO-IU4SQ system architecture, suitable for incremental semantic learning. It comprises a primary (dominant, necessary not sufficient) hybrid (combined deductive and inductive) feedback (provided with feedback loops) EO-IU subsystem in closed-loop with a secondary (dominated) hybrid feedback EO-SQ subsystem. *Subset-of* a computer vision (CV) system, where CV ⊃ EO-IU, the EO-IU subsystem is required to be automatic (no human-machine interaction is required by the CV system to run) and near real-time to provide the EO-SQ subsystem with useful information products, including thematic maps of symbolic quality, such as single-date ESA EO Level 2 Scene Classification Map (SCM) considered necessary not sufficient pre-condition to semantic querying, synonym of semantics-enabled information/knowledge discovery (SEIKD) in massive multi-source EO image databases. The EO-SQ subsystem is provided with a graphic user interface (GUI) to streamline: (i) top-down knowledge transfer from-human-to-machine of an *a priori* mental model of the 4D geospatial-temporal real-world, (ii) high-level user- and application-specific EO semantic content-based image retrieval (SCBIR) operations. Output products generated by the closed-loop EO-IU4SQ system are expected to monotonically increase their value-added with closed-loop iterations, according to Bayesian updating where Bayesian inference is applied iteratively [95, 96]: after observing some evidence, the resulting posterior probability can be treated as a prior probability and a new posterior probability computed from new evidence. One of Marr's legacies is the notion of computational constraints required to make the typically ill-posed non-polynomial (NP)-hard problem of intelligence, encompassing vision [89], better conditioned for numerical solution [30]. Marr's computational constraints that reflect properties of the world are embodied through evolution, equivalent to genotype [71], into the human visual complex system, structured as a hierarchical network of networks with feedback loops [89, 97-102, 181]). Marr's computational constraints are Bayesian priors in a Bayesian inference approach to vision [69, 95, 103], where ever-varying sensations (sensory data) are transformed into stable percepts (concepts) about the world in a world model [20], to perform successfully in the world [15].

To justify our working hypothesis sketched in Figure 3, specifically, 'Human vision → CV ⊃ EO-IU in operating mode ⊃ NASA EO Level 2 product → ESA EO Level 2 product → [EO-SCBIR + SEIKD = AI4DIAS] → GEOSS', let us introduce, first, the definition proposed for an

490   EO-IU system to be considered in operating mode and, second, the background knowledge of
491   vision in the multidisciplinary domain of cognitive science [70-74].
492   Based on scientific literature [10-12, 60, 78, 79, 104], a CV $\supset$ EO-IU system is defined in
493   operating mode if and only if it scores "high" in every index of a minimally dependent and
494   maximally informative (mDMI) set of EO outcome and process (OP) quantitative quality
495   indicators (Q^2Is), to be community-agreed upon to be used by members of the RS community,
496   in agreement with the GEO-CEOS QA4EO *Cal/Val* guidelines [3]. A proposed instantiation of
497   an mDMI set of EO OP-Q^2Is includes:

498   (i)   degree of automation, inversely related to human-machine interaction, e.g.,
499   inversely related to the number of system's free-parameters to be user-defined
500   based on heuristics,
501   (ii)   effectiveness, e.g., thematic mapping accuracy,
502   (iii)   efficiency in computation time and in run-time memory occupation,
503   (iv)   robustness (vice versa, sensitivity) to changes in input data,
504   (v)   robustness to changes in input parameters to be user-defined,
505   (vi)   scalability to changes in user requirements and in sensor specifications,
506   (vii)   timeliness from data acquisition to information product generation,
507   (viii)   costs in manpower and computer power,
508   (ix)   value, e.g., semantic value of output products, economic value of output services,
509   etc.

510   According to the Pareto formal analysis of multi-objective optimization problems,
511   optimization of an mDMI set of OP-Q^2Is is an inherently-ill posed problem in the Hadamard
512   sense [90], where many Pareto optimal solutions lying on the Pareto efficient frontier can be
513   considered equally good [105]. Any EO-IU system solution lying on the Pareto efficient frontier
514   can be considered in operating mode, therefore suitable to cope with the five Vs of spatial-
515   temporal EO *big data*, namely, volume, variety, veracity, velocity and value [4].
516
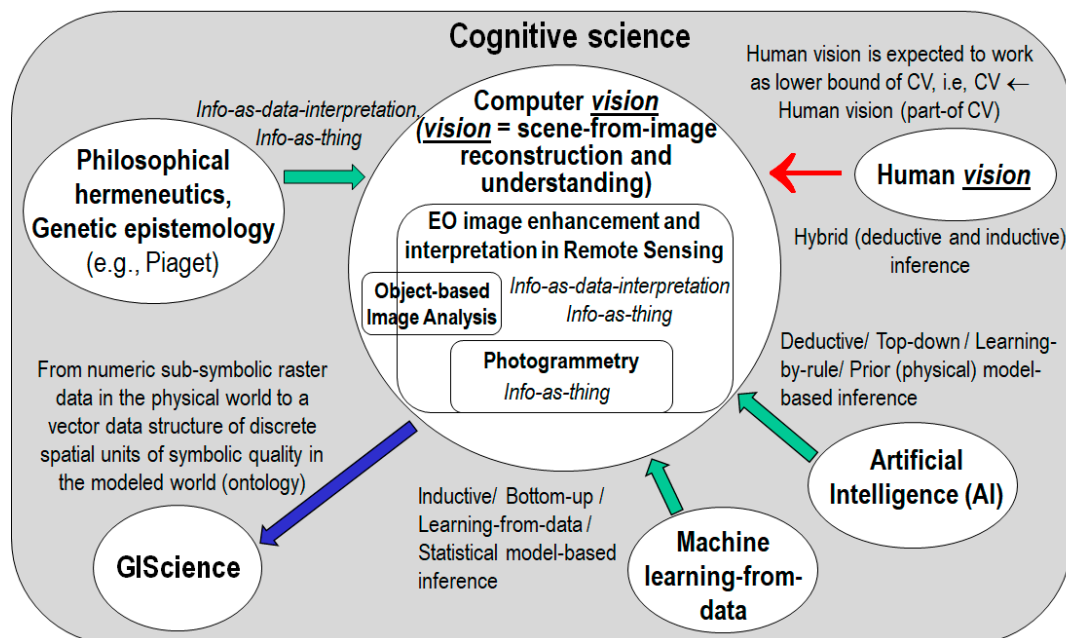
517   **Figure 5.** Multi-disciplinary cognitive science domain, where it is postulated that 'Human
518   vision → computer vision (CV)', where symbol '→' denotes relationship *part-of* pointing from
519   the supplier to the client, not to be confused with relationship *subset-of*, '$\supset$', meaning
520   specialization with inheritance from the superset to the subset, in agreement with the standard
521   Unified Modeling Language (UML) for graphical modeling of object-oriented software [81].
522   Working hypothesis 'Human vision → CV' means that human vision is expected to work as
523   lower bound of CV, i.e., a CV system is required to include as *part-of* a computational model

of human vision. In practice, to become better conditioned for numerical solution, an inherently ill-posed CV system is required to comply with human visual perception phenomena in the multi-disciplinary domain of cognitive science. Cognitive science is the interdisciplinary scientific study of the mind and its processes. It examines what cognition (learning, adaptation, self-organization) is, what it does and how it works [15, 70-74]. It especially focuses on how information/knowledge is represented, acquired, processed and transferred either in the neuro-cerebral apparatus of living organisms or in machines, e.g., computers. Like engineering, remote sensing (RS) is a meta-science [106], whose goal is to transform knowledge of the world, provided by other scientific disciplines, into useful user- and context-dependent solutions in the world. Neuroscience, in particular neurophysiology, studies the neuro-cerebral apparatus of living organisms. Neural network (NN) is synonym of distributed processing system, consisting of neurons as elementary processing elements and synapses as lateral connections. Is it possible and even convenient to mimic biological mental functions, e.g., human reasoning, by means of an artificial mind whose physical support is not an electronic brain implemented as an artificial NN (ANN)? The answer is no according to the "connectionists approach" promoted by traditional cybernetics, where a complex system always comprises an "artificial mind-electronic brain" combination. This is alternative to a traditional approach to artificial intelligence (AI), whose so-called symbolic approach investigates an artificial mind independently of its physical support [70].

In the multidisciplinary domain of cognitive science (see Figure 5), vision is synonym of scene-from-image reconstruction and understanding [20], see Figure 6. Encompassing both biological vision and CV, vision is a cognitive (*information-as-data-interpretation*) problem [15], very difficult to solve because: (i) non-polynomial (NP)-hard in computational complexity [88, 89], (ii) inherently ill-posed in the Hadamard sense [90], i.e., vision admits no solution, multiple solutions or, if the solution exists, the solution's behavior changes continuously with the initial conditions [20, 68]. Vision is inherently ill-posed because affected by: (I) a 4D-to-2D data dimensionality reduction, from the spatial-temporal scene-domain to the (2D) image-domain, for example responsible of occlusion phenomena, and (II) a semantic information gap, from ever-varying sub-symbolic sensory data (sensations) in the physical world to stable symbolic percepts in the mental model of the physical world (modeled world, world ontology, world model) [16-21]. Since it is inherently ill-posed, vision requires *a priori* knowledge in addition to sensory data to become better posed for numerical solution [30]. For example, in inherently ill-posed CV systems, a valuable source of *a priori* knowledge is reverse engineering primate visual perception [89, 97-102], so that a CV system is constrained to include a computational model of human vision, i.e., 'Human vision → CV', see Figure 5. According to cognitive science, AI ⊃ CV is not a problem in statistics [107], which is tantamount to saying there is no (qualitative, equivocal, nominal) semantics in (quantitative, unequivocal, numeric) sensory data [10]. These principles are implicit in the dual meaning of word information, either quantitative (unequivocal) *information-as-thing*, typical of the Shannon data communication/transmission theory [108], or qualitative (equivocal) *information-as-data-interpretation*, typical of AI ⊃ CV tasks investigated by philosophical hermeneutics [15].
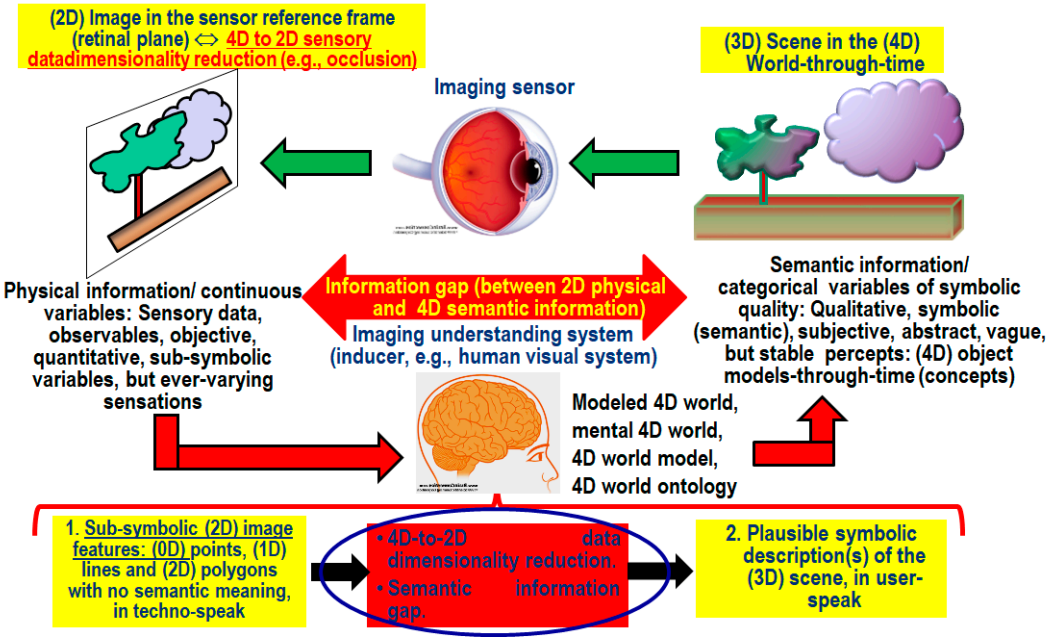
566 **Figure 6.** Synonym of scene-from-image reconstruction and understanding, vision is a
567 cognitive *(information-as-data-interpretation)* problem [15] very difficult to solve because: (i)
568 non-polynomial (NP)-hard in computational complexity [88, 89], and (ii) inherently ill-posed
569 [20, 68] in the Hadamard sense [90]. Vision is inherently ill-posed because affected by: (I) a
570 4D-to-2D data dimensionality reduction from the scene-domain to the image-domain, e.g.,
571 responsible of occlusion phenomena, and (II) a semantic information gap from ever-varying
572 sub-symbolic sensory data (sensations) in the physical world-domain to stable symbolic
573 percepts in the mental model of the physical world (modeled world, world ontology, world
574 model) [16, 21]. Since it is inherently ill-posed, vision requires *a priori* knowledge in addition
575 to sensory data to become better posed for numerical solution [30].

576 Largely oversighted by the RS and CV literature, an unquestionable true-fact
577 (observation) is that spatial information dominates color information in vision [20]. This
578 commonsense knowledge is obvious, but not trivial. For example, it is familiar to all human
579 beings wearing sunglasses: human panchromatic vision is nearly as effective as chromatic
580 vision in scene-from-image reconstruction and understanding [10]. This true-fact means that
581 spatial information dominates both the 4D geospatial-temporal scene-domain and the (2D)
582 image-domain involved with the cognitive task of vision, whose goal is scene-from-image
583 reconstruction and understanding, see Figure 6. This evidence is also acknowledged by the
584 Tobler's first law (TFL) of geography, familiar to geographers. The TFL of geography states
585 that "all things are related, but nearby things are more related than distant things"[109],
586 although certain phenomena clearly constitute exceptions [110]. Obscure to many geographers
587 familiar with the TFL formulation, the statistical concept of spatial autocorrelation is the
588 quantitative counterpart of the qualitative TFL of geography [10]. The relevance of spatial
589 autocorrelation in both the 4D geospatial-temporal scene-domain and the (2D) image domain
590 involved with vision is at the very foundation of the (GE)OBIA approach to CV, originally
591 conceived around year 2000 by the GIScience community as a viable alternative to traditional
592 1D spatial-context insensitive (pixel-based) image analysis [6, 7]. Unfortunately, rather than
593 starting from past background knowledge in the multi-disciplinary domain of cognitive
594 science, the GEOBIA approach was started from scratch by a self-referencing GEOBIA sub-
595 community within the GIScience domain, see Figure 5 [6, 7, 111, 112]. As a consequence of its
596 lack of interdisciplinarity, the GEOBIA community showed an increasing tendency to "re-
597 invent the wheel" in ever-varying implementations of the same sub-optimal EO-IU system
598 architecture, although the CV community clearly acknowledged that the linchpin of success of
599 any CV solution is system design together with information/knowledge representation, rather

than algorithm or implementation [16, 69]. Based on these observations, to enforce a 'Human vision → CV' paradigm, see Figure 5, the following constraint can be adopted to make an inherently ill-posed CV system better conditioned for numerical solution [10].

> If a chromatic CV ⊃ EO-IU system does not down-scale seamlessly to achromatic image analysis, then it tends to ignore the paramount spatial information in favor of subordinate (secondary) spatial context-insensitive color information, such as MS signatures typically investigated in traditional pixel-based single-date or multi-temporal EO-IU algorithms. In other words, a necessary and sufficient condition for a CV ⊃ EO-IU system to fully exploit primary spatial topological information (e.g., adjacency, inclusion, etc.) and spatial non-topological information (e.g., spatial distance, angle distance) components, in addition to secondary colorimetric information, is to perform nearly as well when input with either panchromatic or color imagery [10].

Supported by this background knowledge about vision, a true-fact is that ESA EO Level 2 product generation is an inherently ill-posed CV problem (*chicken-and-egg* dilemma), whose inherently ill-posed CV subtask is cloud and cloud-shadow quality layer detection. Since it is ill-posed, ESA EO Level 2 product generation is, first, very difficult to solve; in fact, no ESA EO Level 2 product has ever been accomplished in operating mode by any EO data provider at the ground segment to date. Second, it requires *a priori* knowledge in addition to sensory data to become better conditioned for numerical solution.

Our conclusion is that systematic ESA EO Level 2 product generation, at the core of the present work, is of potential interest to relevant portions of the RS community, involved with EO *big data* transformation into timely, comprehensive and operational EO data-derived VAPS [3, 5]. Regarded as necessary not sufficient pre-condition for a GEOSS to cope with the five Vs of EO *big data* analytics, see Figure 3, systematic ESA EO Level 2 product generation is still open for solution in operating mode.
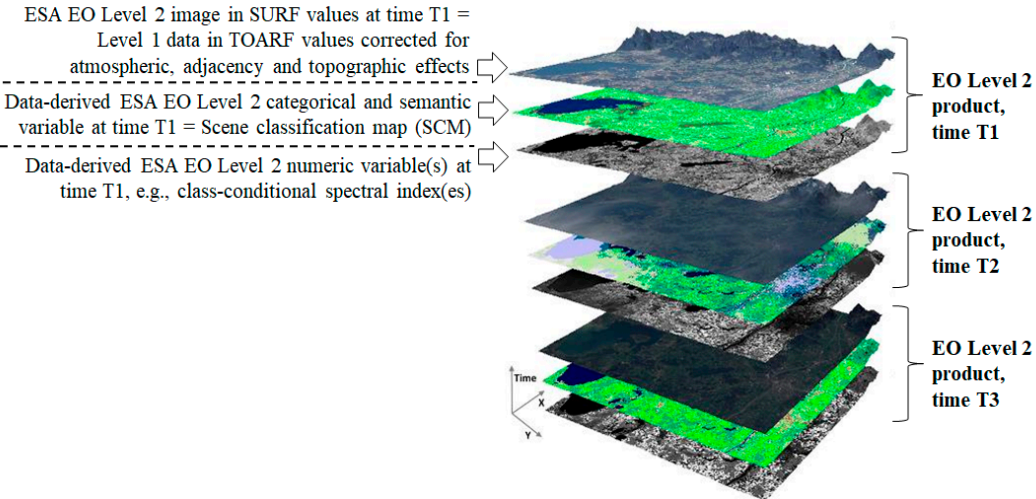
Figure 7. Semantics-enabled EO data cube, synonym of artificial intelligence for data and information access services (AI4DIAS). Each single-date EO Level 1 source image, radiometrically calibrated into top-of-atmosphere reflectance (TOARF) values and stored in the database, is automatically transformed into an ESA EO Level 2 product comprising: (i) a single-date multi-spectral (MS) image radiometrically calibrated from top-of-atmosphere reflectance (TOARF) into surface reflectance (SURF) values, corrected for atmospheric, adjacency and topographic effects, stacked with (ii) its EO data-derived value-adding scene classification map (SCM), equivalent to a sensory data-derived categorical/qualitative variable of semantic quality, where the thematic map legend is general-purpose, user- and application-independent and comprises quality layers such as cloud and cloud-shadow. It is eventually

638   stacked with (iii) its EO data-derived value-adding numeric variables, such as biophysical
639   variables, e.g., LAI [75], class-conditional spectral indexes, e.g., vegetation class-conditional
640   greenness index [113, 114], categorical variables of sub-symbolic quality (geographic field-
641   objects), e.g., fuzzy sets/discretization levels low/medium/high of a numeric variable, etc.
642   [115].

643   The several degrees of novelty of the ESA EO Level 2 product definition (refer to Section
644   1) are highlighted below.
645   First, the ESA EO Level 2 product definition is innovative because it overtakes the
646   traditional concept of EO data cube with an innovative EO data cube stacked with its data-
647   derived value-adding information cube, synonym of semantics-enabled data cube or AI4DIAS,
648   see Figure 7. A semantics-enabled EO data cube is alternative to existing EO data cubes,
649   affected by the so-called data-rich information-poor (DRIP) syndrome [116], such as the
650   existing first generation of the European Commission (EC) data and information access
651   services (DIAS) [117, 118]. Intuitively, EC-DIAS is affected by the DRIP syndrome because it is
652   provided with no CV system in operating mode as inference engine, capable of transforming
653   geospatial-temporal EO *big data*, characterized by the five Vs of volume, variety, veracity,
654   velocity and value [4], into VAPS, starting from semantic information products, such as the
655   ESA EO Level 2 SCM baseline product. Sketched in Figure 4, AI4DIAS complies with the
656   Marr's intuition that "vision goes symbolic almost immediately… without loss of information"
657   [69] (p. 343).
658   Second, in our understanding the ESA EO Level 2 product definition is synonym of EO
659   Analysis Ready Data (ARD) format. This ARD definition is in contrast with the Committee on
660   Earth Observation Satellites (CEOS) ARD for Land (CARD4L) products definition [119], where
661   atmospheric effect removal is required exclusively, whereas no data-derived SCM is
662   demanded as additional output. It is also in contrast with the U.S. Landsat ARD format [120,
663   121], where atmospheric effect removal is required, but no SCM is provided as output. In
664   practice, the CARD4L and U.S. Landsat ARD definitions are *part-of* the ESA EO Level 2 product
665   definition. The latter includes the former. When the latter is accomplished, so is the former, but
666   the vice versa does not hold.
667
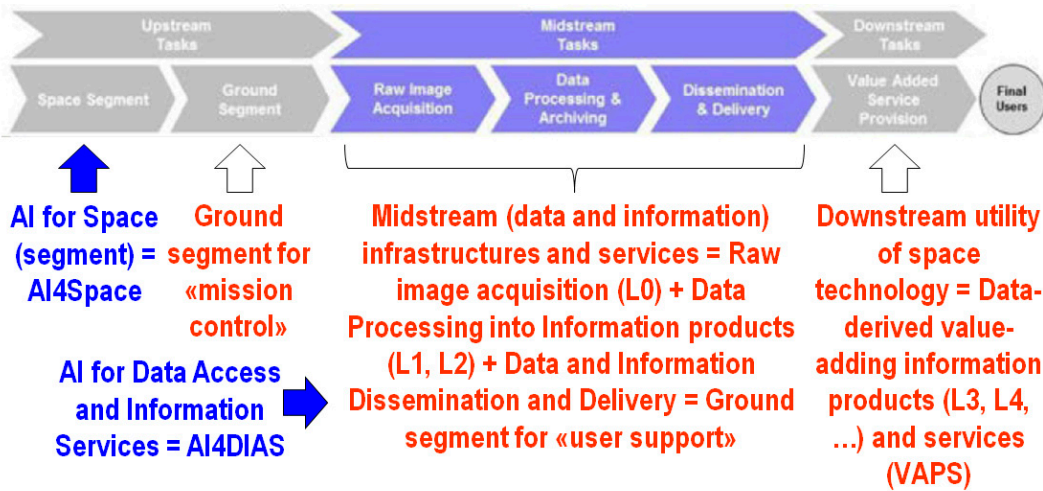
668   **Figure 8.** Definitions in Space Economy 4.0: space segment, ground segment for «mission
669   control» = upstream, ground segment for «user support» = midstream (infrastructures and
670   services), downstream (utility of space technology) [59] (pp. 6, 57).

671   Third, we consider ESA EO Level 2 product generation a horizontal policy for background
672   developments in support of a "new" Space Economy 4.0 [59], see Figure 8. In Space 4.0, global
673   value chains will require both vertical and horizontal policies. Vertical policies are more
674   directional and 'active', focussing on directing change, often through mission-oriented policies

675 that require the active creation and shaping of markets. Horizontal policies are more focused
676 on the background conditions necessary for innovation, correcting for different types of market
677 and system failures [59].
678   Fourth, in an "old" mission-oriented (vertical) space economy [59], the ground segment
679 is typically defined as consisting of upstream and midstream, defined as the portion of ground
680 segment for mission support and user support respectively, see Figure 8. ESA expects ESA EO
681 Level 2 product generation to be accomplished by EO data providers at midstream. Actually,
682 ESA EO Level 2 product generation should occur as early as possible in the information
683 processing chain, e.g., in the space segment preliminary to the ground segment, in compliance
684 with the Marr's intuition that "vision goes symbolic almost immediately… without loss of
685 information" [69] (p. 343). Hence, in Figure 3, ESA EO Level 2 product generation becomes
686 synonym of AI applications for the space segment, AI4Space, where AI ⊃ CV. AI4Space comes
687 before the application of AI techniques to the ground segment, specifically, AI4DIAS. If a CV
688 ⊂ AI application in operating mode is implemented onboard a spaceborne platform of an EO
689 imaging sensor to provide imagery with intelligence (semantics), then Future Intelligent EO
690 imaging Satellites (FIEOS), conceived in the early 2000s [122], become realistic, such as future
691 intelligent EO small satellite constellations. In EO small satellite constellations provided with
692 no on-board radiometric *Cal* subsystem, improved time resolution is counterbalanced by
693 inferior radiometric *Cal* capabilities, considered mandatory by the GEO-CEOS QA4EO *Cal*/*Val*
694 guidelines [3] to guarantee interoperability of multiple platforms and sensors within and
695 across constellations. The visionary goal of AI4Space is realistic, based on the recent
696 announcement of a research and technological development (RTD) project focused on future
697 intelligent small satellite constellations. The quote is: "an Earth-i led consortium will develop
698 a number of new Earth Observation technologies that will enable processes, such as the
699 enhancement of image resolution, cloud-detection, change detection and video compression,
700 to take place on-board a small satellite rather than on the ground. This will accelerate the
701 delivery of high-quality images, video and information-rich analytics to end-users. On-board
702 cloud detection will make the tasking of satellites more efficient and increase the probability
703 of capturing a usable and useful image or video. To achieve these goals, 'Project OVERPaSS'
704 will implement, test and demonstrate very high-resolution optical image analysis techniques,
705 involving both new software and dedicated hardware installed onboard small satellites to
706 radically increase their ability to process data in space. The project will also determine the
707 extent to which these capabilities could be routinely deployed on-board British optical imaging
708 satellites in the future" [123].
709   Fifth, in the RS common practice, the potential impact of the ESA EO Level 2 product
710 definition is relevant because it makes explicit once and for all the undisputable true-fact that
711 atmospheric effect correction [9, 49, 61-66, 124], adjacency and topographic effect corrections
712 [76, 125-129], BRDF effect correction [61, 62, 66, 91-94]; [92], in addition to cloud/cloud shadow
713 quality layer detection [9, 10, 36-39, 41-56], are inherently ill-posed CV problems [20, 68] in the
714 Hadamard sense [90], whose solution does not exist or, if it exists, it is not unique or it is not
715 robust to small changes in the initial condition, including changes to the input dataset. Since
716 they are inherently ill-posed, atmospheric, topographic, adjacency and BRDF effect
717 corrections, in addition to cloud/cloud shadow quality layer mapping, require *a priori*
718 knowledge in addition to sensory data to become better posed for numerical solution [30]. This
719 is tantamount to saying that radiometric *Cal* of EO imagery, encompassing ESA EO Level 2
720 product generation, is a *chicken-and-egg* dilemma [10, 125]. On the one hand, no EO image
721 understanding (classification) into a finite and discrete taxonomy of LC classes, in addition to
722 categorical layers cloud and cloud-shadow, is possible in operating mode if radiometric *Cal* is
723 not accomplished in advance, where dimensionless DNs are transformed into a physical unit
724 of radiometric measure to guarantee data interoperability through space, time and sensors, in
725 agreement with the GEO QA4EO *Cal*/*Val* requirements [5]. On the other hand, no radiometric
726 *Cal* of EO imagery is possible without knowing in advance LC classes and nominal quality

727 layers, such as cloud and cloud-shadow masks, since atmospheric, topographic and BRDF
728 effect corrections are LC class-dependent. This is tantamount to saying that, to become better
729 posed for automatic numerical solution (requiring no human-machine interaction), an
730 inherently ill-conditioned CV algorithm for EO image correction from atmospheric,
731 topographic, adjacency and BRDF effects ought to be run on a stratified (layered, class-
732 conditional) basis, i.e., it should run separately on informative EO image strata (masks, layers).
733 A stratified (layered, class-conditional) approach to CV complies with well-known criteria in
734 the equivocal domain of *information-as-data-interpretation* [15].

735 • Well known in statistics, the principle of statistic stratification. It states that "stratification
736   will always achieve greater precision provided that the strata have been chosen so that
737   members of the same stratum are as similar as possible in respect of the characteristic of
738   interest" [130].

739 • The popular problem solving criterion known as divide-and-conquer (*dividi-et-impera*) [29],
740   to be accomplished in agreement with the engineering principles of modularity, hierarchy
741   and regularity considered necessary for scalability in structured system design [32].

742 • A Bayesian approach to CV, where driven-without-knowledge (unconditional) data
743   analytics is replaced by driven-by-(prior) knowledge (class-conditional) data analytics [69,
744   95, 103, 131]. In the words of Quinlan: "one of David Marr's key is the notion of constraints.
745   The idea that the human visual system embodies constraints that reflect properties of the
746   world is foundational. Indeed, this general view seemed (to me) to provide a sensible way
747   of thinking about Bayesian approaches to vision. Accordingly, Bayesian priors are Marr's
748   constraints. The priors/constraints have been incorporated into the human visual system
749   over the course of its evolutionary history (according to the "levels of understanding of an
750   information processing system" manifesto proposed by Marr and extended by Tomaso
751   Poggio in 2012)" [103, 131]. In agreement with a Bayesian approach to CV, our working
752   hypothesis, sketched in Figure 3, postulates that CV includes a computational model of
753   human vision, i.e., 'Human vision → CV'. In practice, a CV system is constrained to comply
754   with human visual perception. This CV requirement agrees with common sense, although
755   it is largely oversighted in the RS and CV literature. In the words of Marcus: "there is no
756   need for machines to literally replicate the human mind, which is, after all, deeply error
757   prone, and far from perfect. But there remain many areas, from natural language
758   understanding to commonsense reasoning, in which humans still retain a clear advantage.
759   Learning the mechanisms underlying those human strengths could lead to advances in AI,
760   even if the goal is not, and should not be, an exact replica of human brain. For many people,
761   learning from humans means neuroscience; in my view, that may be premature. We don't
762   yet know enough about neuroscience to literally reverse engineer the brain, per se, and
763   may not for several decades, possibly until AI itself gets better. AI can help us to decipher
764   the brain, rather than the other way around. Either way, in the meantime, it should
765   certainly be possible to use techniques and insights drawn from cognitive and
766   developmental psychology, now, in order to build more robust and comprehensive AI,
767   building models that are motivated not just by mathematics but also by clues from the
768   strengths of human psychology" [27]. According to Iqbal and Aggarwal: "frequently, no
769   claim is made about the pertinence or adequacy of the digital models as embodied by
770   computer algorithms to the proper model of human visual perception... This enigmatic
771   situation arises because research and development in computer vision is often considered
772   quite separate from research into the functioning of human vision. A fact that is generally
773   ignored is that biological vision is currently the only measure of the incompleteness of the
774   current stage of computer vision, and illustrates that the problem is still open to solution"
775   [132]. For example, according to Pessoa, "if we require that a CV system should be able to
776   predict perceptual effects, such as the well-known Mach bands illusion where bright and
777   dark bands are seen at ramp edges, then the number of published vision models becomes
778   surprisingly small" [133], see Figure 9. In the CV and RS common practice, constraint

779 'Human vision → CV' is a viable alternative to heuristics typically adopted to constrain
780 inherently ill-posed inductive learning-from-data algorithms, where *a priori* knowledge is
781 typically encoded by design based on empirical criteria [27, 30, 57]. For example, state-of-
782 the-art DCNNs [31] encode *a priori* knowledge by design, where architectural
783 metaparameters must be user-defined based on heuristics. In inductive DCNNs, number
784 of layers, number of filters per layer, spatial filter size, inter-filter spatial stride, local filter
785 size for spatial pooling, spatial pooling filter stride, etc., are typically selected by users
786 based on trial-and-error strategies. As a consequence, inductive DCNNs work as black
787 boxes [27, 57], whose opacity contradicts the well-known engineering principles of
788 modularity, regularity and hierarchy typical of scalable systems [32]. In general, inductive
789 learning-from-data algorithms are inherently semi-automatic (requiring human-machine
790 interactions to define system's free-parameters, such as architectural metaparameters) and
791 site-specific (data-dependent) [2]. "No Free Lunch" theorems have shown that inductive
792 learning-from-data algorithms cannot be universally good [33, 34].
793
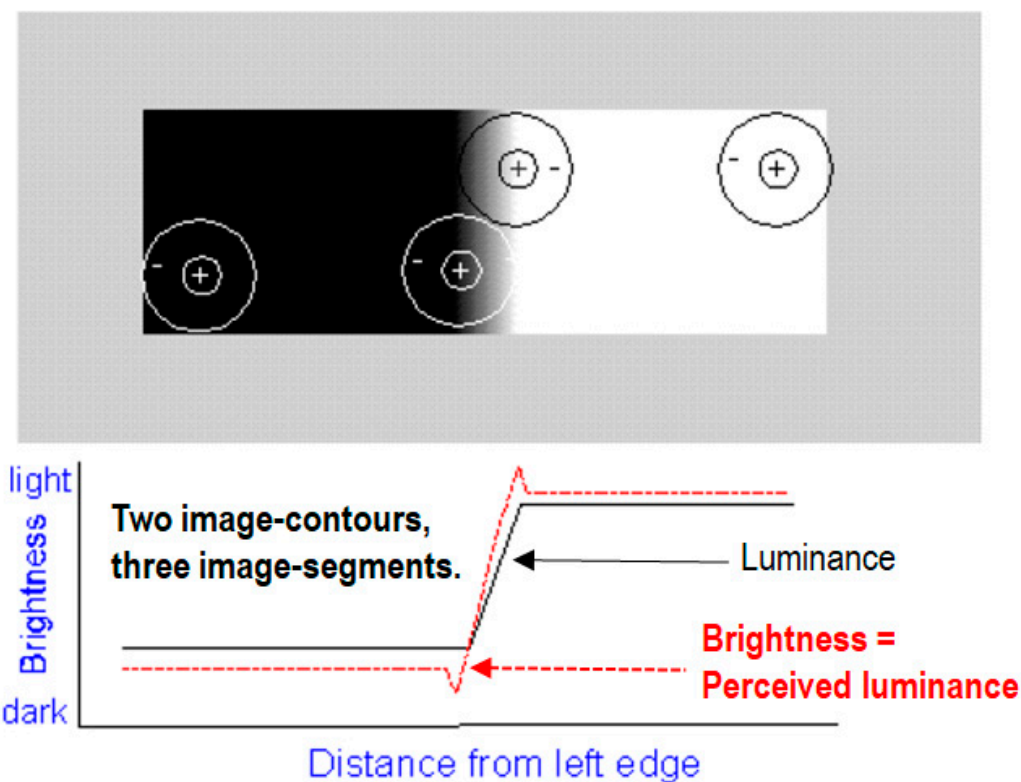
794 **Figure 9.** Mach bands illusion. In black: Ramp in luminance units across space. In red:
795 Brightness (perceived luminance) across space. One of the best-known brightness illusions,
796 where brightness is defined as a subjective aspect of vision, i.e., brightness is the perceived
797 luminance of a surface, is the psychophysical phenomenon of the Mach bands: where a
798 luminance (radiance, intensity) ramp meets a plateau, there are spikes of brightness, although
799 there is no discontinuity in the luminance profile. Hence, human vision detects two
800 boundaries, one at the beginning and one at the end of the ramp in luminance. Since there is
801 no discontinuity in luminance where brightness is spiking, the Mach bands effect is called a
802 visual "illusion". Along a ramp, no image-contour is perceived by human vision, irrespective
803 of the ramp's local contrast (gradient) in range (0, +∞). In the words of Pessoa, "if we require
804 that a brightness model should at least be able to predict Mach bands, the bright and dark
805 bands which are seen at ramp edges, the number of published models is surprisingly small"
806 [133]. In 2D signal (image) processing, the important lesson to be learned from the Mach
807 bands illusion is that local variance, contrast and first-order derivative (gradient) are statistical
808 features (data-derived numeric variables) computed locally in the (2D) image-domain NOT

809   suitable to detect image-objects (segments, closed contours) required to be perceptually
810   "uniform" ("homogeneous") in agreement with human vision. In other words, these popular
811   local statistics are not suitable visual features if detected image-segments/image-contours are
812   required to be consistent with human visual perception, including ramp-edge detection. This
813   straightforward (obvious), but not trivial observation is at odd with a large portion of the
814   existing computer vision (CV) and remote sensing (RS) literature, where many semi-
815   automatic image segmentation/image-contour detection algorithms are based on thresholding
816   the local variance, contrast or first-order gradient, e.g., [134-136], where a system's free-
817   parameter for thresholding image-objects or image-contours must be user-defined in range $\in$
818     $(0, +\infty)$ based on heuristics.

819   Although it is largely ignored by large portions of the RS community, the unequivocal
820 true-fact that inherently ill-posed CV $\supset$ EO-IU algorithms for radiometric *Cal* of DNs into SURF
821 or surface albedo values do require EO image classification to be performed in advance is
822 implicitly confirmed by existing open source or commercial software toolboxes for EO image
823 enhancement (pre-processing), reviewed hereafter.
824   Supported by NASA, the baseline of the U.S. Landsat ARD format [120, 121] is
825 atmospheric effect removal by the open source Landsat-4/5/7 Ecosystem Disturbance Adaptive
826 Processing System (LEDAPS). In LEDAPS, exclusion masks for water, cloud, shadow and
827 snow surface types were detected by an over-simplistic set of prior knowledge-based spectral
828 decision rules applied per pixel [124]. Quantitative analyses of LEDAPS products led by its
829 authors revealed that these exclusion masks were prone to errors, to be corrected in future
830 LEDAPS releases [124]. The same considerations hold for the Landsat 8 OLI/TIRS-specific
831 Landsat Surface Reflectance Code (LaSRC) adopted by the U.S. Landsat ARD format [137].
832 Unfortunately, suitable for testing or *Val* purposes, a multi-level image consisting of exclusion
833 masks has never been generated as output by either LEDAPS or LaSRC. To detect quality
834 layers cloud and cloud-shadow, in addition to snow/ice pixels, recent versions of LEDAPS and
835 LaSRC adopted the open source C Function of Mask (CFMask) algorithm [120, 121]. CFMask
836 was derived from the open source Function of Mask (FMask) algorithm [51, 52], translated into
837 the C programming language to facilitate its implementation in a production environment.
838 Unfortunately, to date, in a recent comparison of cloud and cloud-shadow detectors, those
839 implemented in LEDAPS scored low among alternative solutions [55]. By the way, potential
840 users of U.S. Landsat ARD imagery are informed by USGS in advance about typical CFMask
841 artifacts [56]. Like other cloud detection algorithms [54, 55], CFMask may have difficulties over
842 bright surface types such as building tops, beaches, snow/ice, sand dunes, and salt lakes.
843 Optically thin clouds will always be challenging to identify and have a higher probability of
844 being omitted by the U.S. Landsat ARD algorithm. In addition, the algorithm performance has
845 only been validated for cloud detection, and to a lesser extent for cloud shadows. No rigorous
846 evaluation of the snow/ice detection has ever been performed.
847   Transcoded into CFMask by the U.S. Landsat ARD processor, the open source Fmask
848 algorithm for cloud, cloud-shadow and snow/ice detection was originally developed for
849 single-date 30 m resolution 7-band (from visible blue, B, to thermal InfraRed, TIR) Landsat-
850 5/7/8 MS imagery, which includes a thermal band as key input data requirement [51]. In recent
851 years, FMask was extended to 10 m/20 m resolution Sentinel-2 MS imagery [52], featuring no
852 thermal band, and to Landsat image time-series (multiTemporal Mask, TMask) [53]. For more
853 details about the FMask software design and implementation, refer to the further Section 3.
854
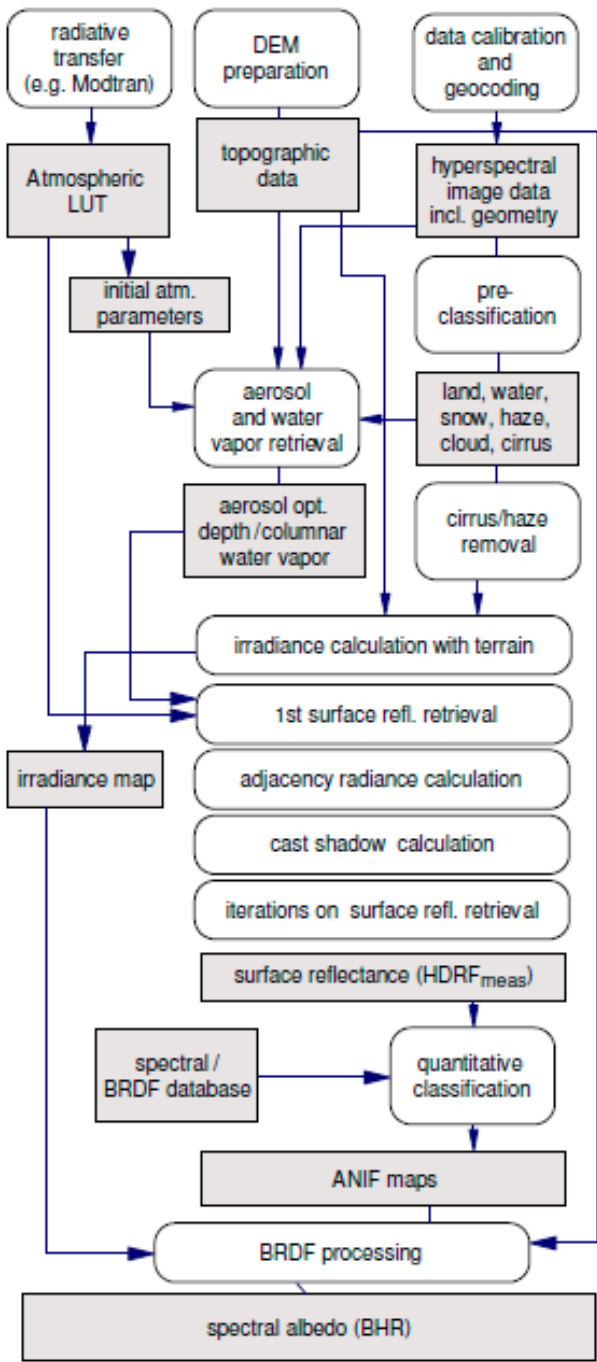
Figure 10. Same as in [66], courtesy of Daniel Schläpfer, ReSe Applications Schläpfer. A complete ("augmented") hybrid (combined deductive and inductive) inference workflow for MS image correction from atmospheric, adjacency and topographic effects. It combines a standard Atmospheric/Topographic Correction for Satellite Imagery (ATCOR) commercial software workflow [63, 64], with a bidirectional reflectance distribution function (BRDF) effect correction, which requires as input an image time-series of the same surface area acquired with different combinations of the sun and sensor positions. Processing blocks are represented as circles and output products as rectangles. This hybrid workflow alternates deductive/prior knowledge-based and inductive/learning-from-data inference units, starting from initial conditions provided by a first-stage prior knowledge-based decision tree for static (non-adaptive to data) color naming, such as the Spectral Classification of surface reflectance signatures (SPECL) decision tree [65] implemented within the ATCOR commercial software toolbox. Categorical variables generated as output by the two processing blocks identified as "pre-classification" and "classification" are employed as input by the subsequent processing

869 blocks to stratify (mask) unconditional numeric variable distributions, in line with the statistic
870 stratification principle [130]. Through statistic stratification, inherently ill-posed inductive
871 learning-from-data algorithms are provided with *a priori* knowledge required in addition to
872 data to become better posed for numerical solution, in agreement with the machine learning-
873 from-data literature [30].

874 In the Atmospheric/Topographic Correction for Satellite Imagery (ATCOR) commercial
875 software product, several per-pixel (spatial context-insensitive) deductive spectral rule-based
876 decision trees are implemented for use in different stages of an EO image enhancement
877 pipeline [63-66, 138, 139], see Figure 10. According to Richter and Schläpfer [63, 64], "pre-
878 classification as part of the atmospheric correction has a long history, e.g., in the NASA's
879 processing chain for MODIS" [50], also refer to [9, 49]. One of the ATCOR's prior knowledge-
880 based per-pixel decision trees delivers as output a haze/ cloud/ water (and snow) classification
881 mask file ("image_hcw.bsq"), see Table 3. In addition, ATCOR includes a so-called prior
882 knowledge-based decision tree for Spectral Classification of surface reflectance signatures
883 (SPECL) [65], see Table 4. Unfortunately, SPECL has never been tested by its authors in the RS
884 literature, although it has been validated by independent means [138, 139].
885
886 **Table 3.** Thematic map legend of the ATCOR-2/3/4 spectral pre-classification [63-66], whose
887 output product is identified as "image_hcw.bsq" (hcw = haze / cloud / water and snow) map.
888 According to Richter and Schläpfer, "pre-classification as part of the atmospheric correction
889 has a long history, e.g., as part of NASA's processing chain for MODIS", e.g., refer to [50].

890
891
892

Label	ATCOR-2/3/4 spectral pre-classification, Land Cover (LC) class definition	Order of detection
0	Background	
1	Cloud shadow	5
2	Cirrus – Thin over water	10
3	Cirrus – Medium over water	11
4	Cirrus – Thick over water	12
5	Land (if not 0 to 5 or 6 to 17)	17
6	Saturated (if (DN > 0.9 * DNmax), then saturated)	1
7	Snow / ice	6
8	Cirrus – Thin over land	7
9	Cirrus – Medium over land	8
10	Cirrus – Thick over land	9
11	Haze – Thin/medium over land	13
12	Haze – Thick/medium over land	14
13	Haze – Thin/medium over water	15
14	Haze – Thick/medium over water	16
15	Cloud over land	3
16	Cloud over water	4

893 **Table 4.** Rule set (structural knowledge) and order of presentation of the rule set (procedural
894 knowledge) adopted by the prior knowledge-based MS reflectance space quantizer, eligible
895 for MS reflectance space hyperpolyhedralization into MS color names, called Spectral
896 Classification of surface reflectance signatures (SPECL), implemented within the ATCOR
897 commercial software toolbox [63-65].

Index	Spectral Categories	Spectral Rule (based on reflectance measured at Landsat TM central wave bands: b1 is located at 0.48 μm, b2 at 0.56 μm, b3 at 0.66 μm, b4 at 0.83 μm, b5 at 1.6 μm, b7 at 2.2 μm)	Pseudo-color
1	Snow/ice	b4/b3 ≤ 1.3 AND b3 ≥ 0.2 AND b5 ≤ 0.12	
2	Cloud	b4 ≥ 0.25 AND 0.85 ≤ b1/b4 ≤ 1.15 AND b4/b5 ≥ 0.9 AND b5 ≥ 0.2	
3	Bright bare soil / sand / cloud	b4 ≥ 0.15 AND 1.3 ≤ b4/b3 ≤ 3.0	
4	Dark bare soil	b4 ≥ 0.15 AND 1.3 ≤ b4/b3 ≤ 3.0 AND b2 ≤ 0.10	
5	Average vegetation	b4/b3 ≥ 3.0 AND (b2/b3 ≥ 0.8 OR b3 ≤ 0.15) AND 0.28 ≤ b4 ≤ 0.45	

6	Bright vegetation	b4/b3 ≥ 3.0 AND (b2/b3 ≥ 0.8 OR b3 ≤ 0.15) AND b4 ≥ 0.45	
7	Dark vegetation	b4/b3 ≥ 3.0 AND (b2/b3 ≥ 0.8 OR b3 ≤ 0.15) AND b3 ≤ 0.08 AND b4 ≤ 0.28	
8	Yellow vegetation	b4/b3 ≥ 2.0 AND b2 ≥_b3 AND b3 ≥ 8.0 AND b4/b5 ≥ 1.5 [a]	
9	Mix of vegetation / soil	2.0 ≤ b4/b3 ≤ 3.0 AND 0.05 ≤ b3 ≤ 0.15 AND b4 ≥ 0.15	
10	Asphalt / dark sand	b4/b3 ≤ 1.6 AND 0.05 ≤ b3 ≤ 0.20 AND 0.05 ≤ b4 ≤ 0.20[a] AND 0.05 ≤ b5 ≤ 0.25 AND b5/b4 ≥ 0.7[a]	
11	Sand / bare soil / cloud	b4/b3 ≤ 2.0 AND b4 ≥ 0.15 AND b5 ≥ 0.15[a]	
12	Bright sand / bare soil / cloud	b4/b3 ≤ 2.0 AND b4 ≥ 0.15 AND (b4 ≥ 0.25b OR b5 ≥ 0.30[b])	
13	Dry vegetation / soil	(1.7 ≤ b4/b3 ≤ 2.0 AND b4 ≥ 0.25[c]) OR (1.4 ≤ b4/b3 ≤ 2.0 AND b7/b5 ≤ 0.83[c])	
14	Sparse veg. / soil	(1.4 ≤ b4/b3 ≤ 1.7 AND b4 ≥ 0.25[c]) OR (1.4 ≤ b4/b3 ≤ 2.0 AND b7/b5 ≤ 0.83 AND b5/b4 ≥ 1.2[c])	
15	Turbid water	b4 ≤ 0.11 AND b5 ≤ 0.05[a]	
16	Clear water	b4 ≤ 0.02 AND b5 ≤ 0.02[a]	
17	Clear water over sand	b3 ≥ 0.02 AND b3 ≥ b4 + 0.005 AND b5 ≤ 0.02[a]	
18	Shadow		
19	Not classified (outliers)		
[a] These expressions are optional and only used if b5 is present. [b] Decision rule depends on presence of b5. [c] Decision rule depends on presence of b7.			

898

899   Commissioned by ESA, the Sentinel-2 (atmospheric and topographic) Correction
900   Prototype Processor (Sen2Cor) is not run systematically at the ESA ground segment. Rather, it
901   can be downloaded free-of-cost from an ESA web site to be run on user side [8, 9, 37]. Hence,
902   the Sen2Cor software toolbox does not satisfy the ESA EO Level 2 product requirements
903   specification, refer to Section 1. The existing Sentinel-2 sensor-specific Sen2Cor prototype
904   processor, sketched in Figure 11, adopts the same feedforward workflow of the popular
905   ATCOR commercial software product [63-66]. The Sen2Cor software toolbox accomplishes,
906   first, one SCM product generation from TOARF values by means of a per-pixel (spatial context-
907   insensitive) prior spectral knowledge-based (static, non-adaptive to data) decision tree, whose
908   SCM legend is shown in Table 1. Next, a stratified (class-conditional, driven-by-knowledge)
909   MS image radiometric correction approach is adopted to transform TOARF into SURF values,
910   where SURF values are sequentially corrected for atmospheric, adjacency and topographic
911   effects stratified by the same SCM product generated at first stage from TOARF values.
912
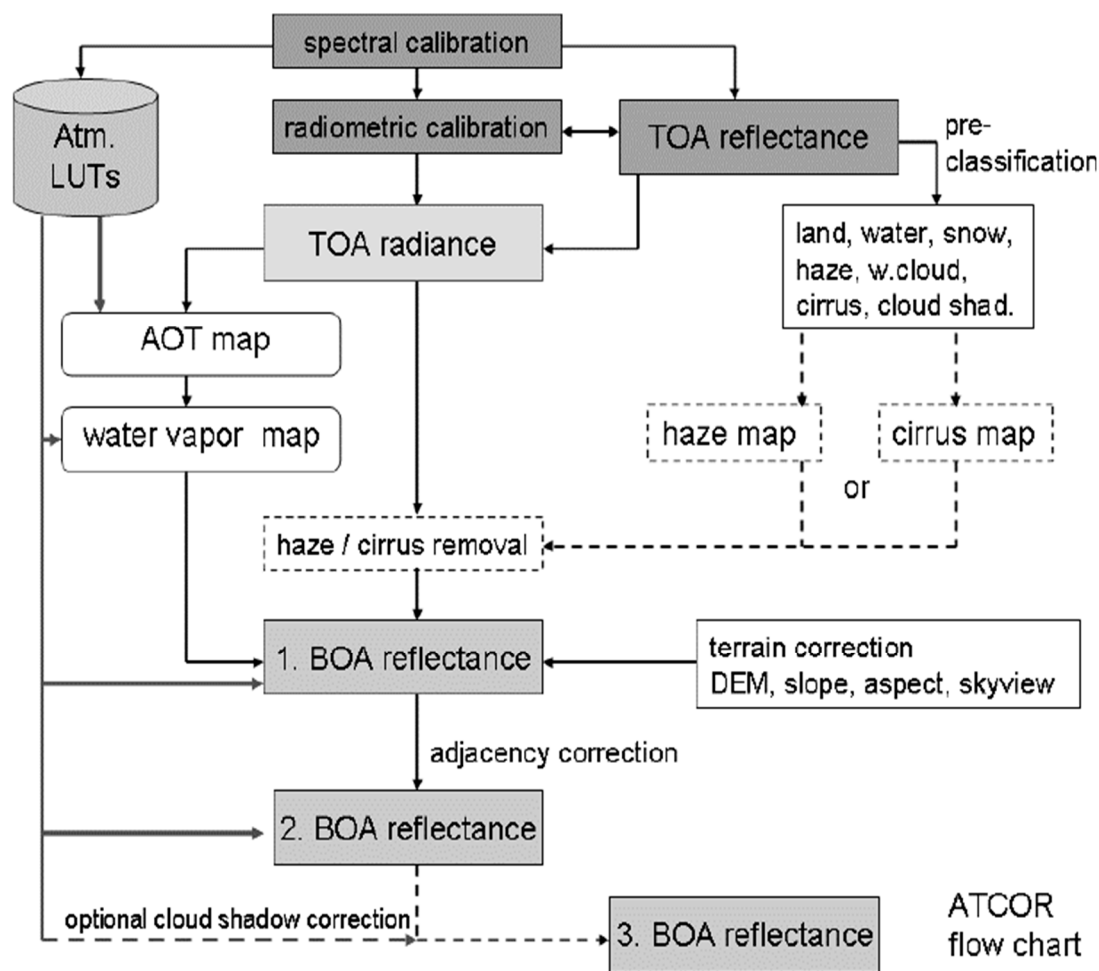
913 **Figure 11.** Sen2Cor flow chart for ESA Level 2 product generation from Sentinel-2 imagery [8,
914 9, 37], same as in the Atmospheric/Topographic Correction for Satellite Imagery (ATCOR)
915 commercial software toolbox [63, 64]. While sharing the same system design, Sen2Cor and
916 ATCOR differ at the levels of abstraction of algorithm and implementation [69]. First, a scene
917 classification map (SCM) is generated from top-of-atmosphere reflectance (TOARF) values.
918 Next, class-conditional MS image radiometric enhancement of TOARF into surface reflectance
919 (SURF) values, synonym of bottom-of-atmosphere (BOA) reflectance values, corrected for
920 atmospheric, adjacency and topographic effects is accomplished in sequence, stratified by the
921 same SCM product generated at first stage from TOARF values. More acronyms in this figure:
922 AOT = aerosol optical thickness, DEM = digital elevation model, LUT = look-up table.

923 Aa a viable alternative to the existing Sen2Cor, ATCOR, LEDAPS and LaSRC system
924 design and implementation solutions, an inherently ill-posed atmospheric, topographic,
925 adjacency and BRDF effect corrector for systematic ESA EO Level 2 product generation, where
926 EO image classification, including cloud/cloud-shadow quality layer detection, is required in
927 advance to be run on a LC class-specific basis [76, 125-127], is conceptually proposed as
928 sketched in Figure 12 [10, 78, 79]. The estimation from an input numeric variable, starting from
929 EO sensory data equivalent to DNs provided with no physical meaning, of an output numeric
930 variable provided with a physical meaning of increasing quality, such as EO data-derived
931 TOARF, SURF and spectral albedo values featuring increasing levels of radiometric *Cal* quality,
932 requires as additional input, at each stage of the EO image enhancement flow chart, a
933 categorical (nominal) variable belonging to a preliminary SCM automatically generated from
934 the EO image radiometrically corrected at the previous stage in the workflow. In other words,
935 equivalent to two sides of the same coin, categorical variables (e.g., SCMs at increasing levels
936 of mapping accuracy and semantics) and continuous variables (e.g., TOARF, SURF and

937   spectral albedo values) should be estimated from raw EO imagery (coded as dimensionless
938   DNs, provided with no physical meaning) alternately and iteratively. It means that, in an EO
939   image pre-processing workflow conceived as a hybrid inference feedback system, such as the
940   stratified topographic correction (STRATCOR) algorithm proposed in [76], numeric variables
941   are estimated on a categorical (stratified, masked, class-conditional) basis while (enhanced)
942   categorical variables are estimated from (enhanced) continuous variables, in addition to *a priori*
943   knowledge, which is required in addition to data to make the inherently ill-posed CV problem
944   of radiometric *Cal* better posed for numerical solution [10, 30, 91], see Figure 12.
945
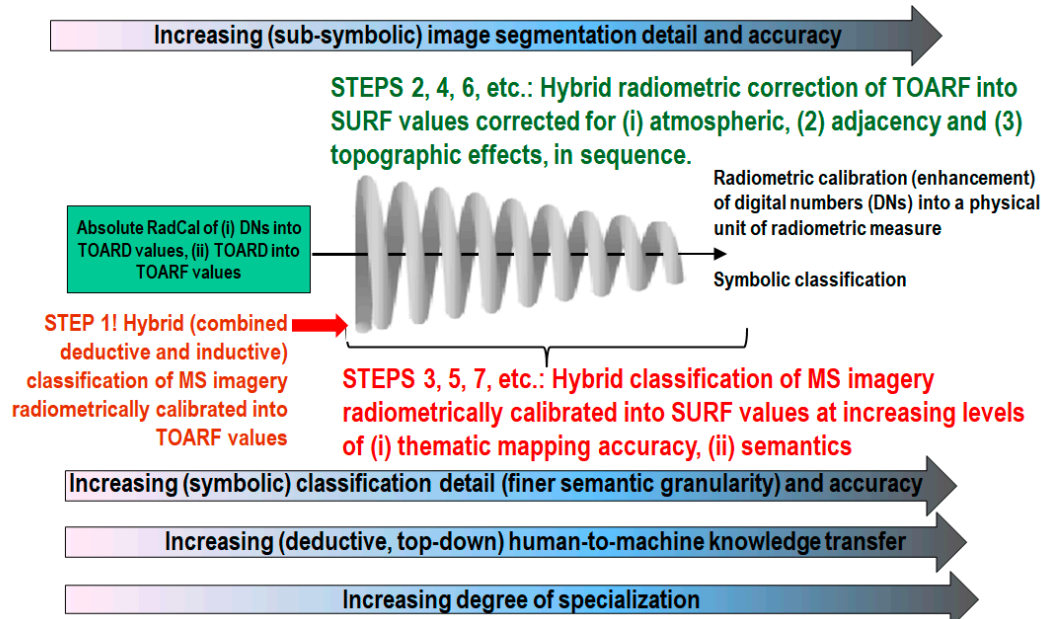
946   **Figure 12.** Ideal ESA EO Level 2 product generation design as a hierarchical alternating
947   sequence of: (A) hybrid (combined deductive and inductive) radiometric enhancement of
948   multi-spectral (MS) dimensionless digital numbers (DNs) into top-of-atmosphere reflectance
949   (TOARF), surface reflectance (SURF) values and spectral albedo values corrected in sequence
950   for (1) atmospheric, (2) adjacency, (3) topographic and (4) BRDF effects, and (B) hybrid
951   (combined deductive and inductive) classification of TOARF, SURF and spectral albedo values
952   into a sequence of ESA EO Level 2 scene classification maps (SCMs), whose legend (taxonomy)
953   of community-agreed land cover (LC) class names, in addition to quality layers cloud and
954   cloud-shadow, increases hierarchically. An implementation in operating mode of this EO
955   image pre-processing system design for stratified topographic correction (STRATCOR) is
956   presented and discussed in [10, 76, 78, 79]. In comparison with this desirable system design,
957   let us consider that, for example, the existing Sen2Cor software toolbox, developed by ESA to
958   support a Sentinel-2 sensor-specific Level 2 product generation on user side [8, 9, 37]), adopts
959   no hierarchical alternating approach between MS image classification and MS image
960   radiometric enhancement. Rather, Sen2Cor accomplishes, first, one SCM generation from
961   TOARF values based on a per-pixel (spatial context-insensitive) prior spectral knowledge-
962   based decision tree. Next, a class-conditional MS image radiometric enhancement of TOARF
963   into SURF values corrected for atmospheric, adjacency and topographic effects is
964   accomplished in sequence, stratified by the same SCM product generated at first stage from
965   TOARF values, see Figure 11.
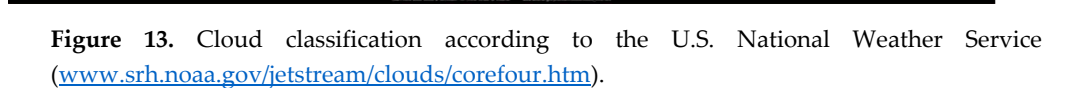
Figure 13. Cloud classification according to the U.S. National Weather Service (www.srh.noaa.gov/jetstream/clouds/corefour.htm).
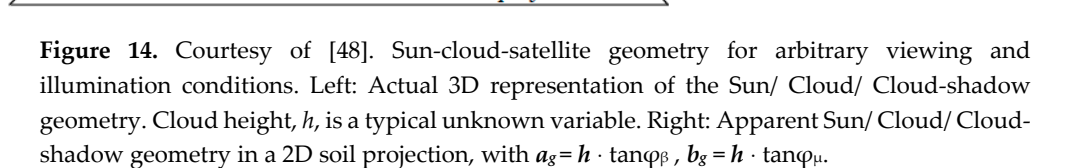
Figure 14. Courtesy of [48]. Sun-cloud-satellite geometry for arbitrary viewing and illumination conditions. Left: Actual 3D representation of the Sun/ Cloud/ Cloud-shadow geometry. Cloud height, h, is a typical unknown variable. Right: Apparent Sun/ Cloud/ Cloud-shadow geometry in a 2D soil projection, with $a_g = h \cdot \tan\varphi_\beta$, $b_g = h \cdot \tan\varphi_\mu$.

3. Related works

To contribute toward filling an analytic and pragmatic information gap from multi-sensor, multi-temporal and multi-angular EO *big data* cubes to systematic ESA EO Level 2 product generation never accomplished to date by any EO data provider at the ground segment (refer to Section 1), our attention focuses on the RTD of an inherently ill-posed CV subsystem for cloud and cloud-shadow quality layer detection (see Figure 13 and Figure 14) in operating mode (refer to Section 2), considered an open problem to date by the RS community [54-56]. Provided with a relevant survey value, this Section revises standard cloud/cloud-shadow detectors, available either open source or free of cost. To highlight their structural drawbacks and failure modes, if any, as our fourth original contribution, standard cloud/cloud-shadow detectors are critically reviewed at the Marr's four levels of system abstraction, known

984   as information/knowledge representation, system design, algorithm and implementation [10,
985   16, 69].
986   In the last decade, many different cloud/cloud-shadow detection algorithms were
987   presented in the RS literature, to be input with either a single-date MS image or an MS image
988   time-series typically acquired by either one EO spaceborne/airborne MS imaging sensor or a
989   single family of MS imaging sensors, e.g., spaceborne Landsat [9, 10, 36-39, 41-53].
990   Predated by a long history of deductive convolutional neural networks (CNNs), consisting
991   of "handcrafted" (physical model-based) multi-scale 2D spatial filter banks, developed since
992   the early 1980s for multi-scale image analysis (encoding, decomposition), synthesis (decoding,
993   reconstruction) [140] and classification [141], the recent hype about inductive end-to-end
994   learning-from-data Deep CNNs (DCNNs) in CV applications [31] is progressively affecting the
995   RS discipline, in spite of increasing disillusionment in the AI community [10, 27, 57, 97, 107,
996   142-145]. For example, an increasing number of DCNN applications for cloud detection can be
997   found in the RS literature, e.g., [35]. However, to our best knowledge, only one application of
998   DCNNs to the simultaneous detection of cloud and cloud-shadow phenomena exists to date
999   [146].
1000   To explain this fact, a non-trivial understanding of the information/knowledge
1001 representation in DCNNs is required, according to the Marr's four levels of understanding of
1002 an information processing system, specifically, information/knowledge representation, system
1003 design (architecture), algorithm per architectural block and implementation per algorithm [10,
1004 69, 78, 79]. In inductive learning-from-data DCNNs, 2D spatial filter profiles are learned end-
1005 to-end from supervised image examples whereas *a priori* knowledge is encoded by design
1006 based on heuristics, a.k.a. trial-and-error. In greater detail, the whole set of DCNN architectural
1007 metaparameters, specifically, number of layers, number of convolutional filters per layer, filter
1008 size, inter-filter stride, subsampling filter size, subsampling inter-filter stride, etc., is user-
1009 defined based on empirical criteria. Unfortunately, inductive learning-from-data algorithms,
1010 including DCNNs, are affected by inherent limitations [2, 10, 27, 30, 33, 34, 57, 97, 107, 142, 143]
1011 and known failure modes [144, 145], including the following. Suitable for learning complex
1012 correlations between input and output features, inductive learning-from-data systems are
1013 unable to learn representations of causality (cause-effect relationships, dependency), known
1014 that "correlation does not imply causation and vice versa" [10, 16, 27, 30, 57, 58]. This limitation
1015 implies that, first, it not straightforward to integrate *a priori* knowledge about the physical
1016 world onto a DCNN architecture, whose information representation pertains mainly to
1017 (largely opaque) correlations between input and output features. Second, DCNNs thus far
1018 have shown no self-organizing capability, e.g., based on combinations of cooperative with
1019 competitive learning-from-data policies [147], suitable for developing a syntactic hierarchical
1020 system [16, 27], structured as a network of specialized subnetworks [10], in agreement with the
1021 engineering principles of modularity, hierarchy and regularity considered necessary for
1022 scalability in structured system design [32]. In the words of Marcus, "the core problem, at least
1023 at present, is that deep learning learns correlations between sets of features that are themselves
1024 "flat" or non-hierarchical, as if in a simple, unstructured list, with every feature on equal
1025 footing. Hierarchical structures (e.g., syntactic trees that distinguish between main clauses and
1026 embedded clauses in a sentence) are not inherently or directly represented in such systems,
1027 and as a result deep learning systems are forced to use a variety of proxies that are ultimately
1028 inadequate, such as the sequential position of a word presented in a sequences " [27].
1029   Our straightforward, but not trivial conjecture is that cloud/cloud-shadow detection is a
1030 typical example of physical model-based cause-effect relationship expected to be very difficult
1031 to solve by inductive machine learning-from-examples algorithms, including DCNNs, suitable
1032 for learning complex correlations between input and output features, but unable to discover
1033 inherent representations of causality.
1034   This conjecture is perfectly confirmed by experimental conclusions reported in [146] (pp.
1035 32, 33): "The main problem of DCNN-based classification is cloud-shadow, e.g., in an image

1036   object-based Intersection over Union, IOU, classification quality measure assessment in range
1037   [0, 1], class cloud-shadow scored as low as IOU = 0.0212 in the validation image set at hand".
1038   Predicted by theory, these experimental results prove *a posteriori* the well-groundedness of our
1039   first-principles in the AI ⊃ CV domains. These expected results reveal that, based on
1040   knowledge of the first-principles in inference, specifically, induction, deduction and abduction
1041   [16, 19, 21], and in agreement with the increasing disillusionment of the AI community about
1042   deep learning-from-data [10, 27, 57, 97, 107, 142-145], the RS community should avoid
1043   exploring dead-end solutions where AI ⊃ CV algorithms, developed by other communities in
1044   the cognitive science domain (see Figure 5), are adopted as black-boxes by RS scientists and
1045   practitioners, such as increasingly popular DCNNs applied for detecting cloud and cloud-
1046   shadow cause-effect-relationships in EO imagery. Based on this rationale, although considered
1047   state-of-the-art by the mainstream CV and RS audience, DCNN solutions are excluded from
1048   any further review in this paper, focused on jointly cloud/cloud-shadow detection.

1049   For comparison purposes, three popular computer programs available free-of-cost for
1050   cloud/cloud-shadow detection in spaceborne MS imagery are critically revised hereafter, see
1051   Table 5.

1052   •   The open source single-date FMask algorithm [51], originally developed for single-date 30
1053   m resolution 7-band (from visible blue, B, to thermal InfraRed, TIR) Landsat-5/7/8 MS imagery,
1054   which includes a thermal band as key input data requirement. FMask was recently extended
1055   to 10 m/20 m resolution Sentinel-2 MS imagery [52], featuring no thermal band, and to Landsat
1056   image time-series (multiTemporal Mask, TMask) [53]. The potential relevance of FMask is
1057   augmented by considering that CFmask, an Fmask program version transcoded into the C
1058   programming language for increased efficiency, is adopted for cloud, cloud-shadow and
1059   snow/ice classification by the LEDAPS and LaSRC algorithms for atmospheric correction in the
1060   U.S. Landsat ARD product [120, 121, 137]. Unfortunately, CFMask is affected by known
1061   artifacts [56]. Moreover, in a recent comparison of cloud and cloud-shadow detectors, those
1062   implemented in LEDAPS scored low among alternative solutions [55].

1063   •   The single-date Sentinel-2 Multi-Spectral Instrument (MSI) sensor-specific Sen2Cor
1064   prototype processor, capable of automated atmospheric, adjacency and topographic effect
1065   correction and SCM product generation, including cloud and cloud-shadow detection, refer to
1066   the SCM legend shown in Table 1. The Sen2Cor prototype processor is distributed free-of-cost
1067   by ESA to be run on user side [8, 9]. Hence, it does not satisfy the ESA EO Level 2 product
1068   requirements specification proposed in Section 1. Sen2Cor incorporates capabilities of the
1069   ATCOR commercial software toolbox [63-65], see Figure 11. Sen2Cor is affected by known
1070   artifacts [37, 40, 54].

1071   •   The multi-date CNES/CESBIO/DLR Multisensor Atmospheric Correction and Cloud
1072   Screening (MACCS)-Atmospheric/Topographic Correction (ATCOR) Joint Algorithm (MAJA)
1073   [39, 41], which incorporates capabilities of the ATCOR commercial software toolbox [63-65]. It
1074   is affected by known artifacts [40, 54].

1075   Table 5 summarizes the Sen2cor, MAJA and FMask computer programs at the Marr levels
1076   of system understanding known as information/knowledge representation, system design
1077   (architecture) and algorithm [10, 69, 78, 79].

1078
1079   **Table 5.** Comparison of alternative cloud/cloud-shadow detection algorithms at the Marr
1080   levels of system understanding of information/knowledge representation, system design
1081   (architecture) and algorithm [10, 69, 78, 79]

Acronyms Digital number (featuring no physical meaning) = **DN** Top-of-atmosphere reflectance = **TOARF**.	Multi-spectral (MS) Sensor(s)	Radio metric calibration	Spatial resolution	Spectral resolution	Single-date (S) or Multi-temporal (MT)	Land cover (LC) class detection, in addition to classes cloud and cloud-shadow, if any	Cloud detection	Cloud-shadow detection

Surface reflectance = **SURF**, where TOARF ⊃ SURF, because TOARF ≈ SURF + atmospheric noise + topographic noise. Inductive = **I**. Deductive = **D**. Hybrid = Combined I + D = **H**. 1D Pixel-based (spatial context-insensitive and spatial topology non-preserving) = **P**. 1D Object-based (spatial context-sensitive, but spatial topology non-preserving) = **O**. 2D image analysis (spatial context-sensitive and spatial topology-preserving) = **2D**. Yes: **Y**. No: **N**.		Acronyms: **TOARF** or **SURF**, refer to cell at top left		Acronyms: Visible Blue, Green, Red = **B**, **G**, **R**. Near InfraRed (IR) = **NIR**. Medium IR = **MIR**. Thermal IR = **TIR**.		Acronyms: **I, D** or **H**, refer to cell at top left	Acronyms: **P, O** or **2D**, refer to cell at top left	Acronyms: **I, D** or **H**, refer to cell at top left	Acronyms: **P, O** or **2D**, refer to cell at top left	Acronyms: **I, D** or **H**, refer to cell at top left	Acronyms: **P, O** or **2D**, refer to cell at top left	**Spatial search of cloud-shadow pixels starting from cloud candidates**
Proposed approach, AutoCloud+	All MS past, present and future, airborne or spaceborne, whether or not provided with radiometric calibration metadata files	DN or TOARF or SURF or surface albedo	Any	From B, G, R, NIR, MIR to TIR, including Cirrus band (depending on the available spectral channels).	S	H, with LC classes: Water, Shadow, Bare soil, Built-up, Vegetation, Snow, Ice, Fire, Others	P + O + 2D	H	P + O + 2D	H	P + O + 2D	Y
Sen2Cor (including all cloud probability classes)	Sentinel-2 MSI	TOARF	10 m	B, G, R, NIR, MIR to TIR, including Cirrus band.	S	D, with LC classes: Water, Bare soil, Vegetation, Snow	P	D	P	D	P	Y
MAJA	Formosat2, LANDSAT 5/7/8, SPOT 4/5, Sentinel 2, VENµS.	TOARF	5.3 to 30 m	From B, G, R, NIR, MIR to TIR, including Cirrus band (depending on the available spectral channels)	MT	D, with LC classes: Water, Bare soil, Vegetation, Snow	P	D	P	D	P	Y
FMask	Landsat-7/8 (with thermal band) and Sentinel-2 (without thermal band)	TOARF	10 to 30 m	From B, G, R, NIR to MIR, plus TIR when available (in Landsat imagery)	S	D, with LC classes: Clear land, clear water, snow.	P	D	P + contextual to remove isolated pixels	H	P + O, due to Segmentation of the cloud layer	Y

ATCOR-4 [64]	Airborne, spaceborne	TOARF or SURF or spectral albedo	Any	From B, G, R, NIR to MIR, including Cirrus band (depending on the available spectral channels). No TIR is exploited.	S	D, with LC classes: Water, Land, Haze, Snow/Ice (depending on the available spectral channels)	P	H (D + I, e.g., I = image-wide histogram-based analytics)	P	H	P	N

1082

The first observation stemming from Table 5 is that the Sen2cor and MAJA computer programs employ deductive (top-down, prior knowledge-based) inference, exclusively, to map MS imagery onto LC classes, in addition to quality layers cloud and cloud-shadow. This is in contrast with biological cognitive systems [77], where hybrid inference combines deductive and inductive inference to take advantage of each and overcome their shortcomings [2, 10, 33, 34, 78, 79], refer to Section 2.

The second observation driven from Table 5 is that the Sen2cor, MAJA and FMask computer programs employ 1D image analysis algorithms exclusively, either pixel-based, i.e., spatial context-insensitive and spatial topology non-preserving, or spatial context-sensitive (e.g., image object-based or local window-based), but spatial topology non-preserving (non-retinotopic) [10, 89, 97, 147]. In CV programs, 1D image analysis is a methodological (structural) drawback because perceptual evidence proves that, in vision, primary spatial topological information (e.g., adjacency, inclusion, etc.) and spatial non-topological information (e.g., spatial distance, angle measure) components dominate secondary color information, which is the sole information available at the sensor's spatial resolution, i.e., at the pixel level of spatial analysis, refer to Section 2 [10]. Intuitively, 1D image analysis algorithms are invariant to permutations in the 1D vector data sequence generated from a (2D) image, where image is synonym of 2D gridded data set, see Figure 15 [31]. In short, 1D analysis of (2D) imagery is affected by a loss in data dimensionality.

1102

Dali's "Gala contemplating the Mediterranean Sea" at 20 mtr becomes the Lincoln portrait, RGB image, ≈ 18 × 13 = 234 Dali's square, 504 × 669 digital pixels

Pnchrmtc image.

Median filter, 35 × 35 pixels in size

2D grid, 35 × 35 pixels per local window

1D image analysis is invariant to permutations in the input sequence, i.e., insensitive to changes in the order of presentation of the input sequence!

1D image analysis = vector sequence / vector series analysis, where each vector data is either pixel-based or local window-based

Order of presentation in the input vector sequence

This is WHAT a traditional inductive 1D data-sequence learning classifier actually sees when watching the (2D) image at left.

1D image analysis = either local window-based (insensitive to spatial topological info) OR pixel-based (spatial context-insensitive, insensitive to spatial topological AND spatial non-topological information)

Figure 15. Example of 1D image analysis, which is spatial topology non-preserving (non-retinotopic) in a (2D) image-domain [10, 89, 97, 147]. Intuitively, 1D image analysis is insensitive to permutations in the input data set [31]. Synonym of 1D analysis of a 2D gridded data set, 1D image analysis is affected by spatial data dimensionality reduction. The (2D) image at left is transformed into the 1D vector data stream (sequence) shown at bottom, where

1108   vector data are either pixel-based or spatial context-sensitive, e.g., local window-based. This
1109   1D vector data stream means nothing to a human photointerpreter. When it is input to either
1110   an inductive learning-from-data classifier or a deductive learning-by-rule classifier, the 1D
1111   vector data sequence is what the classifier actually sees when watching the (2D) image at left.
1112   Undoubtedly, computers are more successful than humans in 1D image analysis. Nonetheless,
1113   humans are still far more successful than computers in 2D image analysis (see Figure 16).

1114   Alternative to 1D image analysis is 2D image analysis, which is spatial topology-
1115   preserving (retinotopic) [10, 89, 97, 147], i.e., it is sensitive to permutations in the order of
1116   presentation of the input data set [31], see Figure 16. In our understanding, 2D image analysis
1117   is the linchpin of success of multi-scale 2D spatial filter banks for image analysis (encoding,
1118   decomposition), synthesis (decoding, reconstruction) and classification, either
1119   deductive/physical model-based [140, 141] or end-to-end inductive learning-from-data, such
1120   as DCNNs [31].
1121
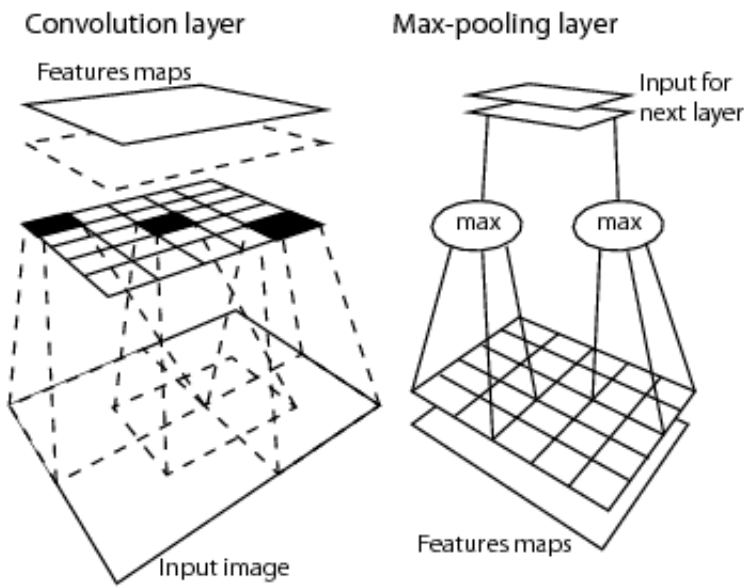
Figure 16. 2D image analysis as synonym of spatial topology-preserving (retinotopic) feature
mapping in a (2D) image-domain [10, 89, 97, 147]. Intuitively, 2D image analysis is sensitive to
permutations in the input data set [31]. Activation domains of physically adjacent processing
units in the 2D array of convolutional spatial filters are spatially adjacent regions in the 2D
visual field. Provided with a superior degree of biological plausibility in modelling 2D spatial
topological and spatial non-topological information components, distributed processing
systems capable of 2D image analysis, such as deep convolutional neural networks (DCNNs),
typically outperform traditional 1D image analysis approaches. Will computers ever become
as good as humans in 2D image analysis?

1131   The fundamental difference between 1D image analysis and 2D image analysis with
1132   regard to spatial topology-preserving (retinotopic) feature mapping [10, 89, 97, 147] is at the
1133   basis of a proposed revision of the loose GE(OBIA) paradigm [7] into a more restrictive
1134   definition of EO imagery for Geographical Sciences (EO4GEO), synonym of 2D analysis of EO
1135   (2D) imagery for GISCience applications [111, 112], see Figure 17.
1136
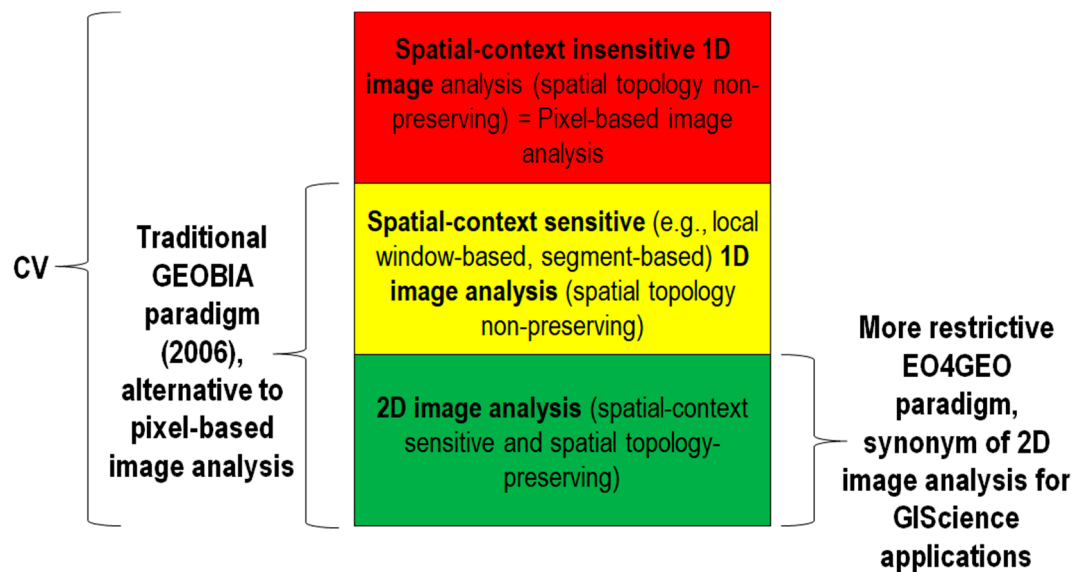
1137   **Figure 17.** EO for Geographical Sciences (EO4GEO, EO4GIScience) framework, meaning EO
1138   big data analytics in operating mode for GIScience applications, constrained by 2D
1139   (retinotopic, spatial topology-preserving) image analysis in cognitive science [111]. EO4GEO
1140   is more restrictive than the traditional GEOBIA paradigm, formalized in 2006 and 2014 as a
1141   viable alternative to 1D spatial context-insensitive (pixel-based) image analysis [6, 7, 112].

1142   At the Marr's less abstract levels of understanding of an information processing system,
1143   known as algorithm and implementation [10, 69, 78, 79], subsequent to the two more abstract
1144   levels of understanding of information/knowledge representation and system design
1145   (architecture), it is interesting to investigate the Sen2Cor's static (non-adaptive to data, prior
1146   knowledge-based) per-pixel spectral rule-based decision tree implementation for automated
1147   ESA EO Level 2 SCM product generation [9]. Noteworthy, the same considerations driven
1148   from the Sen2Cor's spectral knowledge-based decision tree implementation for SCM
1149   generation hold for the LEDAPS, LaSRC and ATCOR spectral knowledge-based decision trees,
1150   implemented for pixel-based pre-classification as necessary not sufficient pre-condition to
1151   make inherently ill-posed atmospheric and/or topographic correction algorithms better posed
1152   for numerical solution [30], see Section 2. According to Richter and Schläpfer [63, 64], "pre-
1153   classification as part of the atmospheric correction has a long history, e.g., in the NASA's
1154   processing chain for MODIS" [50].
1155   First, in the interdisciplinary domain of cognitive science [11, 12], it was highlighted that
1156   static (non-adaptive to data, prior knowledge-based) spectral rule-based decision trees aim at
1157   a mutually exclusive and totally exhaustive (hyper)polyhedralization of a MS reflectance
1158   (hyper)space, equivalent to (numeric) color space discretization into color names belonging to
1159   a categorical variable, known as color vocabulary. Within the domain of cognitive science (see
1160   Figure 5), color naming was deeply investigated by linguistics. Central to this consideration is
1161   Berlin and Kay's landmark study of a "universal" inventory of eleven basic color (BC) words
1162   in twenty human languages: black, white, gray, red, orange, yellow, green, blue, purple, pink
1163   and brown [148]. Suitable for color naming of MS imagery, MS reflectance (hyper)space
1164   (hyper)polyhedralization is difficult to think of and impossible to visualize when the MS data
1165   space dimensionality is superior to three, see Figure 18. This is not the case of basic color (BC)
1166   names adopted in human languages [148], whose mutually exclusive and totally exhaustive
1167   perceptual polyhedra, neither necessarily convex nor connected, are intuitive to think of and
1168   easy to visualize in a 3D monitor-typical red-green-blue (RGB) data cube [149], see Figure 19.
1169
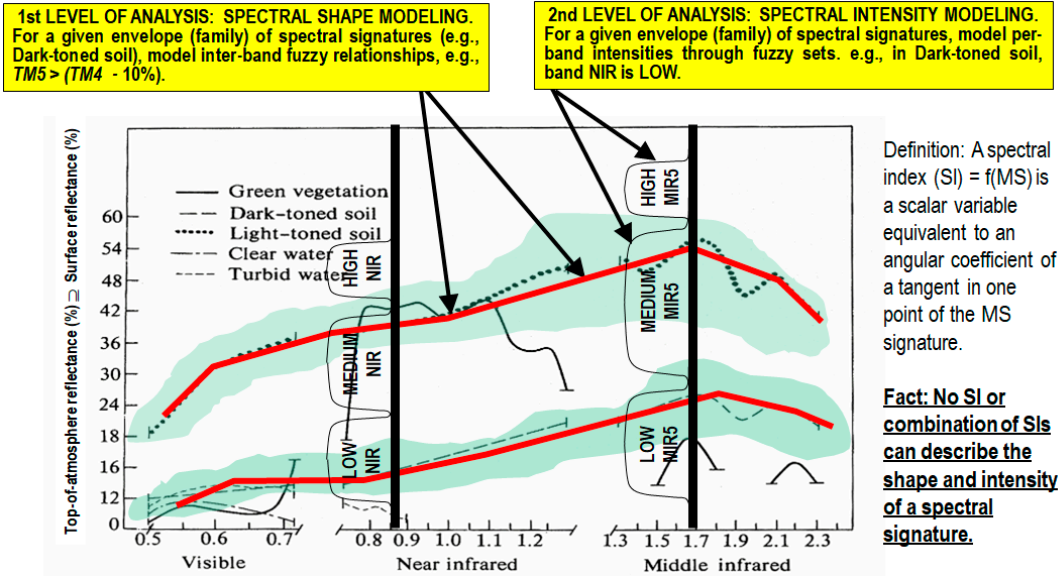
Figure 18. Examples of land cover (LC) class-specific families of spectral signatures [14] in top-of-atmosphere reflectance (TOARF) values, which include surface reflectance (SURF) values as a special case in clear sky and flat terrain conditions [150], i.e., in general, TOARF $\supseteq$ SURF, where TOARF $\approx$ SURF (depicted as an ideal "noiseless" spectral signature in red) + atmospheric and topographic noise. A within-class family of spectral signatures (e.g., dark-toned soil) in TOARF or SURF values forms a buffer zone (hyperpolyhedron, envelope, manifold, joint distribution), depicted in light green. Like a vector quantity has two characteristics, a magnitude and a direction, any LC class-specific MS manifold is characterized by a multivariate shape and a multivariate intensity information component. In the RS literature, typical prior knowedge-based spectral decision trees for MS reflectance space hyperpolyhedralization into a finite and discrete vocabulary of MS color names, such as Sen2Cor's [9], MAJA's [39, 41], ATCOR's [63, 64], LEDAPS' [120, 121, 124) and LaSRC's [120, 121, 137], typically adopt either a multivariate analysis of spectral indexes or a logical (AND, OR) combination of univariate variables, such as scalar spectral indexes or spectral channels, considered mutually independent. A typical spectral index is a scalar band ratio or band-pair difference equivalent to an angular coefficient of a tangent to the spectral signature in one point. It is well known that infinite functions can feature the same tangent value in one point. In practice, no spectral index or combination of spectral indexes can reconstruct the multivariate shape and multivariate intensity information components of a spectral signature. As a viable alternative to traditional static (non-adaptive to data) spectral rule-based decision trees found in the RS literature, the Satellite Image Automatic Mapper (SIAM)'s prior knowledge-based spectral decision tree [10, 11, 12, 76, 78, 79, 91, 113, 114, 138, 139, 151] adopts a convergence-of-evidence approach to model any target family (ensemble) of spectral signatures, forming a hypervolume of interest in the MS reflectance hyperspace, as a combination of multivariate shape information with multivariate intensity information components. For example, as shown above, typical spectral signatures of dark-toned soils and typical spectral signatures of light-toned soils form two MS envelopes in the MS reflectance hyperspace that approximately share the same multivariate shape information component, but whose pair of multivariate intensity information components does differ.
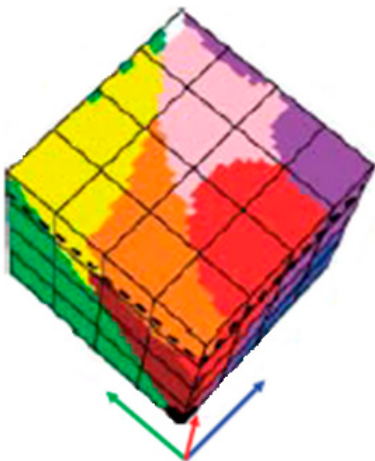
1199 **Figure 19.** Courtesy of [149]. Unlike a MS reflectance space hyperpolyhedralization difficult to
1200   think of and impossible to visualize when the number of channels is superior to three, an RGB
1201   data cube polyhedralization is intuitive to think of and straightforward to display. For example,
1202   based on psychophysical evidence, human basic color (BC) names can be mapped onto a
1203   monitor-typical RGB data cube. Central to this consideration is Berlin and Kay's landmark
1204   study of a "universal" inventory of eleven BC words in twenty human languages: black, white,
1205   gray, red, orange, yellow, green, blue, purple, pink and brown [148].

1206 In vision, where a (2D) image-domain and a 4D geospatial-temporal scene-domain co-
1207 exist, see Figure 6, a community-agreed discrete and finite vocabulary of MS color names,
1208 pertaining to a MS color space in the image-domain, such as the eleven BC names proposed by
1209 Berlin and Kay in the image-domain of visible bands RGB [148], see Figure 19, should never be
1210 confused with a vocabulary of classes of real-world objects in the scene-domain, such as a
1211 discrete and finite legend of LC classes. Color names provide a categorical (nominal)
1212 representation of the numeric photometric variable associated as attribute to any LC class
1213 belonging to a discrete and finite LC class legend. Encoded as a categorical variable, a color
1214 attribute of a (categorical) LC class should never be confused with the LC class it belongs to.
1215 On the hand, the same color name can be shared by several LC classes. On the other hand, a
1216 single LC class can feature several color names as photometric attribute [11, 12]. For example,
1217 Adams et al. correctly observed that discrete spectral endmembers typically adopted in hyper-
1218 spectral image interpretation "cannot always be inverted to unique LC class names" [152]. This
1219 commonsense knowledge is sketched in Table 6, where set A = DictionaryOfColorNames with
1220 cardinality |A| = a = ColorVocabularyCardinality = 11 and set B = LegendOfObjectClassNames
1221 with cardinality |B| = b = ObjectClassLegendCardinality = 3. Between the vocabulary A of
1222 color names in the image-domain and the vocabulary B of LC classes in the scene-domain there
1223 is a binary relationship, R: A ⇒ B, subset of the 2-fold Cartesian product A × B, i.e., R: A ⇒ B
1224 ⊆ A × B, where A ≠ B in general. The Cartesian product A × B is a set whose elements are
1225 ordered pairs of each instance of set A combined with each instance of set B. Hence, the size of
1226 the Cartesian product A × B is rows × columns = a × b, where a ≠ b in general. Noteworthy,
1227 Cartesian product A × B ≠ FrequencyCount(A × B), where FrequencyCount(A × B) is known as
1228 two-way contingency table, association matrix, cross tabulation, bivariate table, bivariate
1229 frequency table (BIVRFTAB) or confusion matrix [10, 22, 153-157].
1230
1231 **Table 6.** . Example of a binary relationship R: A ⇒ B ⊆ A × B from set A =
1232   DictionaryOfColorNames, with cardinality |A| = a = ColorVocabularyCardinality = 11, and
1233   the set B = LegendOfObjectClassNames, with cardinality |B| = b =
1234   ObjectClassLegendCardinality = 3, where A × B is the 2-fold Cartesian product between sets A
1235   and B. The Cartesian product of two sets A × B is a set whose elements are ordered pairs. The
1236   size of A × B is rows × columns = a × b. The dictionary LegendOfObjectClassNames is a

1237   superset of the typical taxonomy of land cover (LC) classes adopted by the RS community.
1238   "Correct" entry-pairs (marked with √) must be: (i) selected by domain experts based on a *hybrid*
1239   combination of deductive prior beliefs with inductive evidence from data and (ii) community-
1240   agreed upon, to be used by members of the community [11, 12].

			Target classes of individuals (entities in a conceptual model for knowledge representation built upon an ontology language)		
			Class 1, Water body	Class 2, Tulip flower	Class 3, Italian tile roof
Basic color (BC) names	black			√	
	blue		√	√	
	brown		√	√	√
	grey				
	green		√	√	
	orange			√	
	pink			√	
	purple			√	
	red			√	√
	white			√	
	yellow			√	

1241

1242   In spite of this commonsense knowledge, see Table 6, and in contrast with the
1243   unquestionable true-fact that, in vision, primary spatial information dominates secondary
1244   color information in both the image-domain and the scene-domain [10-12, 20], see Section 2,
1245   prior knowledge-based spectral decision trees for MS color space hyperpolyhedralization into
1246   color names implemented by the RS community typically assume that the vocabulary A of
1247   color names in the image-domain and the vocabulary B of LC classes in the scene-domain do
1248   coincide in cardinality, semantics and order of presentation. If hypothesis A = B holds true,
1249   then the binary relationship R: A $\Rightarrow$ B $\subseteq$ A × B ≠ FrequencyCount(A × B) becomes a bijective
1250   (injective and surjective) function, while the two-way confusion matrix FrequencyCount(A ×
1251   B) becomes square, where the main diagonal guides the interpretation process [11, 12]. This is
1252   the case of the LC map legend of an SCM product generated as output by a static decision tree
1253   of spectral rules implemented by the ATCOR software toolbox, see Table 3 and Table 4, and
1254   by the Sen2Cor software toolbox, see Table 1, where there is one spectral rule (or OR-
1255   combination of spectral rules) per LC class and vice versa. Since the unrealistic assumption
1256   that categorical variable A = DictionaryOfColorNames, with cardinality |A| = a =
1257   ColorVocabularyCardinality, coincides with categorical variable B =
1258   LegendOfObjectClassNames, with cardinality |B| = b = ObjectClassLegendCardinality, is
1259   undertaken at the abstract level of system understanding of information/knowledge
1260   representation, considered the linchpin of success of any information processing system [10,
1261   16, 69], it heavily affects all subsequent levels of abstraction, specifically, system design,
1262   algorithm and implementation, in agreement with well-known information principle known
1263   as garbage in, garbage out (GIGO), synonym of error propagation through an information
1264   processing chain [11, 12]. This error propagation effect affecting CV $\supset$ EO-IU applications
1265   increases as the imaging sensor's spatial resolution becomes finer, such as in EO high spatial
1266   resolution (HR, in range [1 m, 30 m]) and very high spatial resolution (VHR, < 1 m) image
1267   understanding tasks [14].
1268   In addition to the unrealistic assumption that vocabularies of color names and of LC class
1269   names do coincide at the level of system understanding of information/knowledge
1270   representation, the implementation of the Sen2Cor's spectral rules for MS reflectance space
1271   hyperpolyhedralization into MS color names appears inadequate to define mutually exclusive
1272   and totally exhaustive hyperpolyhedra, where each hyperpolyhedron is a multivariate data
1273   distribution (joint probability).
1274   First, Sen2Cor models each joint probability by a single spectral rule as an and/or-
1275   combination of univariate distributions. It assumes a joint distribution is equivalent to a
1276   product of univariate distributions, which holds true if and only if univariate variables are

mutually independent. This assumption is completely unrealistic when modeling manifolds of LC class-specific spectral signatures sampled at a discrete and finite set of spectral bands. These spectral band values are not statistically independent because they are LC class-dependent. In general, multivariate data statistics are more informative than a combination of univariate data statistics. For example, maximum likelihood data classification, accounting for multivariate data correlation and variance (covariance), is typically more accurate than parallelepiped data classification whose rectangular decision regions, equivalent to a concatenation of univariate data constraints, poorly fit multivariate data in the presence of bivariate cross-correlation [24]. As a typical example of this critical point, see Table 4, showing the SPECL decision tree instantiation proposed by the ATCOR software toolbox, where each spectral rule is implemented as a sequence of univariate statistics.

Second, in the Sen2Cor's spectral rule-based decision tree a spectral rule implementation typically adopts many spectral indexes in the definition of each hyperpolyhedron equivalent to a MS color name. Like a vector quantity has two characteristics, a magnitude and a direction, any LC class-specific MS manifold is characterized by a multivariate shape and a multivariate intensity information component, see Figure 18. A spectral index, implemented as either a band difference or a band ratio, is conceptually equivalent to the angular coefficient of a tangent to the spectral signature in one point. It is well known that infinite functions can pass through the same point with the same angular coefficient. It means that, although appealing due to its conceptual and numerical simplicity [2], any scalar spectral index, equivalent to a spectral slope, is a MS shape descriptor independent of the MS intensity. It is unable *per se* to represent either the multivariate shape information component or the multivariate intensity information component of a MS signature [10]. In other words, no spectral index or combination of spectral indexes provides a lossless reconstruction of the multivariate shape and multivariate intensity information components of a spectral signature [10-12]. Because of this spectral information loss, the number of scalar spectral indexes proposed in the RS literature is ever increasing [2], in the unrealistic attempt to extract a more informative scalar variable from a multivariate spectral signature. In some published works, the misuse of spectral indexes reaches its peak when, to simplify a multivariate spectral signature both conceptually and numerically, the number of univariate spectral indexes extracted from the spectral signature is superior to the number of spectral bands; in this no-win situation, no MS data compression is accomplished while a loss in spectral information is guaranteed. As a typical example of this second critical point, see Table 4, showing the SPECL decision tree instantiation proposed by the ATCOR software toolbox where several band ratios are employed for modeling a MS hyperpolyhedron of interest in the MS data hyperspace.

4. Methods

To contribute toward the RTD of the first (never accomplished to date) CV system in operating mode capable of systematic ESA EO Level 2 product generation from multi-sensor, multi-temporal and multi-angular EO *big data* cubes (see Section 1), where conceptual drawbacks and failure modes of available CV subsystems for cloud and cloud-shadow detection in EO optical imagery, such as Sen2Cor and MAJA, must be overcome (see Section 3), an inherently ill-posed AutoCloud+ CV subsystem development [10, 36, 67] was constrained in accordance to the following system requirements specification, at the levels of system understanding of information/knowledge representation, system architecture, algorithm and implementation in the multidisciplinary domain of cognitive science (see Figure 5).

- Combined deductive and inductive (hybrid) inference, where deductive and inductive inference alternate at increasing levels of specialization, see Figure 12, to take advantage of each and overcome their shortcomings [10, 76, 78, 79].
- 2D (retinotopic, spatial topology-preserving) image analysis, see Figure 16, where primary spatial information and secondary color information in vision are combined according

1328 to a convergence-of-evidence approach, consistent with human symbolic reasoning, where
1329 eventually weak, but independent sources of evidence can be combined to infer strong
1330 conjectures, and where it is acknowledged that "vision goes symbolic almost immediately"
1331 [10, 69].

1332 • Provided with feedback loops (feedback system) [89, 97-102, 181]. A hybrid feedback CV
1333 system is alternative to inductive feedforward CV systems, such as popular DCNNs [31],
1334 deductive feedforward CV systems, such as Sen2Cor, see Figure 11 and Table 5, and hybrid
1335 feedforward CV systems, such as the "augmented" ATCOR software toolbox, see Figure 12.

1336 • Suitable for cloud and cloud-shadow quality layer detection in MS imagery under
1337 operational constraints of "universality". To be considered "universal" in operating mode
1338 (refer to Section 2), AutoCloud+ was required to be: (i) "fully automated", i.e., it requires no
1339 human-machine interaction to run and no labeled data set for supervised inductive learning-
1340 from-data, (ii) near real-time, e.g., its computational complexity increases linearly with image
1341 size, (iii) robust to changes in MS imaging sensor's spatial and spectral resolution
1342 specifications, and (iv) robust to changes in radiometric *Cal* metadata parameters, i.e.,
1343 AutoCloud+ can be input with multi-source MS imagery whether or not radiometrically *Cal*
1344 into TOARF, SURF or surface albedo values, such as EO image acquired by multiple platforms,
1345 either spaceborne or airborne, including unmanned aerial vehicles (UAVs), whose lightweight
1346 imaging sensors typically do not provide any radiometric *Cal* metadata file.

1347 At the level of system understanding of information/knowledge representation, the
1348 AutoCloud+ CV subsystem adopts a convergence-of-evidence approach equivalent to a
1349 Bayesian naïve classifier. According to the Bayesian law, a naive Bayes classifier assumes the
1350 "naive" conditional independence of input features F_i, i = 1, …, I, hence,

1351 $$p(c|F_i, …, F_I) = p(c) \prod_{i=1}^{I} p(F_i|c). \tag{1}$$

1352 Deeply investigated by the CV community [16, 69, 88] and by those portions of the RS
1353 community involved with traditional content-based image retrieval (CBIR) [87, 158] and with
1354 EO-IU applications for Earth surface variables estimation [10-12, 20, 78, 79, 159-161], well-
1355 known visual features are: (i) color values, typically discretized by humans into a finite and
1356 discrete vocabulary of BC names [148, 149]; (ii) planar shape [10, 160-163]; (iii) texture, defined
1357 as the perceptual spatial grouping of texture elements known as texels [10, 16, 164-166] or
1358 tokens [69]; (iv) inter-object spatial topological relationships, e.g., adjacency, inclusion, etc., and
1359 (v) inter-object spatial non-topological relationships, e.g., spatial distance, angle measure, etc.
1360 [16-21]. In vision, color is the sole visual property available at the imaging sensor's spatial
1361 resolution, i.e., at pixel level. In other words, pixel-based information is spatial context-
1362 independent, i.e., per-pixel information is exclusively related to color properties. Among the
1363 aforementioned visual variables, per-pixel color values are the sole non-spatial (spatial context-
1364 insensitive) numeric variable. It is easy to prove that, irrespective of their Pearson inter-feature
1365 cross-correlation, if any, individual sources of visual evidence, specifically, color, local shape,
1366 texture and inter-object spatial relationships, are statistically independent because, in general,
1367 Pearson's linear cross-correlation does not imply causation [10, 16, 27, 30, 57, 58]. In the CV
1368 domain, if priors are ignored because considered equiprobable in a maximum class-conditional
1369 likelihood inference approach, alternative to a maximum *a posteriori* optimization criterion, and
1370 if a canonical interpretation based on frequentist statistics can be relaxed by fuzzy logic [167]
1371 into a membership function m(·) ∈ [0, 1], then the naive Bayes classifier, see Equation (1),
1372 becomes [10-12]:

1373 p(c| ColorValue(x), ShapeValue(x), TextureValue(x), SpatialRelationships(x,
1374 Neigh(x))) =
1375 $p(c|F_i, …, F_{I=4}) = p(c) \prod_{i=1}^{I=4} p(F_i|c) \propto$
1376 m(c| ColorValue(x), ShapeValue(x), TextureValue(x), SpatialRelationships(x,
1377 Neigh(x))) ∝

1378 $\quad\min\{\sum_{\text{ColorName}=1}^{\text{ColorVocabularyCardinality}} m_1(\text{ColorValue}(x)|\text{ColorName}) \cdot m_2(\text{ColorName}|c),$

1379 $\quad m_3(\text{ShapeValue}(x)\,|\,c),\ m_4(\text{TextureValue}(x)\,|\,c),\ m_5(\text{SpatialRelationships}(x,$

1380 $\quad \text{Neigh}(x))\,|\,c)\} =$

1381 $\quad \min\{m_2(\text{ColorName*}\,|\,c),\ m_3(\text{ShapeValue}(x)\,|\,c),\ m_4(\text{TextureValue}(x)\,|\,c),$

1382 $\quad m_5(\text{SpatialRelationships}(x,\ \text{Neigh}(x))\,|\,c)\},\ c = 1,\ \dots,\ \text{ObjectClassLegendCardinality},$

1383 $\quad$ where ColorName* $\in$ {1, ColorVocabularyCardinality}, such that $m_1(\text{ColorValue}(x)\,|$

1384 $\quad \text{ColorName*}) = 1$ and $m_2(\text{ColorName*}\,|\,c) \in \{0, 1\},$ $\qquad\qquad\qquad\qquad$ (2)

1385 where x is a spatial unit in the (2D) image-domain, either 0D point, 1D line or 2D polygon [168],
1386 Neigh(x) is a generic 2D spatial neighborhood of spatial unit x, colorValue(x) belongs to a MS
1387 measurement space $\Re^{MS}$, i.e., ColorValue(x) $\in \Re^{MS}$, and color space $\Re^{MS}$ is partitioned into a
1388 set of mutually exclusive and totally exhaustive hyperpolyhedra, equivalent to a discrete and
1389 finite vocabulary (categorical variable) of static color names, with ColorName = 1, ..,
1390 ColorVocabularyCardinality. About Equation (2), the following considerations hold.

1391 $\quad\triangleright\quad$ Each numeric ColorValue(x) is one point in a MS color space $\Re^{MS}$. In the MS color space,
1392 $\qquad$ each point belongs to a single color name (hyperpolyhedron), identified as ColorName* in
1393 $\qquad$ the static color vocabulary, i.e., $\forall$ ColorValue(x) $\in \Re^{MS}$, then
1394 $\qquad$ equality $\sum_{\text{ColorName}=1}^{\text{ColorVocabularyCardinality}} m_1(\text{ColorValue}(x)|\text{ColorName}) =$
1395 $\qquad m_1(\text{ColorValue}(x)|\text{ColorName*}) = 1$ holds, where $m_1(\text{ColorValue}(x)\,|\,\text{ColorName}) \in \{0, 1\}$
1396 $\qquad$ is a binary (crisp) membership function, with ColorName = 1, …,
1397 $\qquad$ ColorVocabularyCardinality.

1398 $\quad\triangleright\quad$ Equation (2) shows that any convergence-of-evidence approach is more selective than each
1399 $\qquad$ individual source of evidence, in line with a focus-of-visual attention mechanism [88].

1400 $\qquad\triangleright\quad$ In Equation (2), a vocabulary of color names, physically equivalent to a partition of
1401 $\qquad$ a numeric color hyperspace $\Re^{MS}$ into color name-specific hyperpolyhedra, is conceptually
1402 $\qquad$ equivalent to a latent/ hidden/ hypothetical categorical variable, see Figure 20. In statistics,
1403 $\qquad$ the popular concept of latent/hidden categorical variable was introduced to fill the
1404 $\qquad$ information gap from input numeric observables, e.g., sub-symbolic sensory data such as
1405 $\qquad$ color values in a color space, to an output categorical variable, such as a discrete and finite
1406 $\qquad$ dictionary of LC classes in the mental model of the physical world (world ontology, world
1407 $\qquad$ model). Latent/hidden variables are categorical variables not directly measured, but
1408 $\qquad$ inferred from lower level variables. "The terms hypothetical variable or hypothetical
1409 $\qquad$ construct may be used when latent variables correspond to abstract concepts, like
1410 $\qquad$ perceptual categories or discrete mental states" [10, 169, 170]. Hence, to fill the semantic
1411 $\qquad$ gap from input sub-symbolic sensory data to an output categorical variable of symbolic
1412 $\qquad$ quality, an hypothetical categorical variable, such as a discrete and finite dictionary of BC
1413 $\qquad$ names [148, 149], is considered to be of "semi-symbolic" quality, i.e., superior to zero
1414 $\qquad$ semantics, but inferior to the symbolic quality of the output categorical variable.

1415
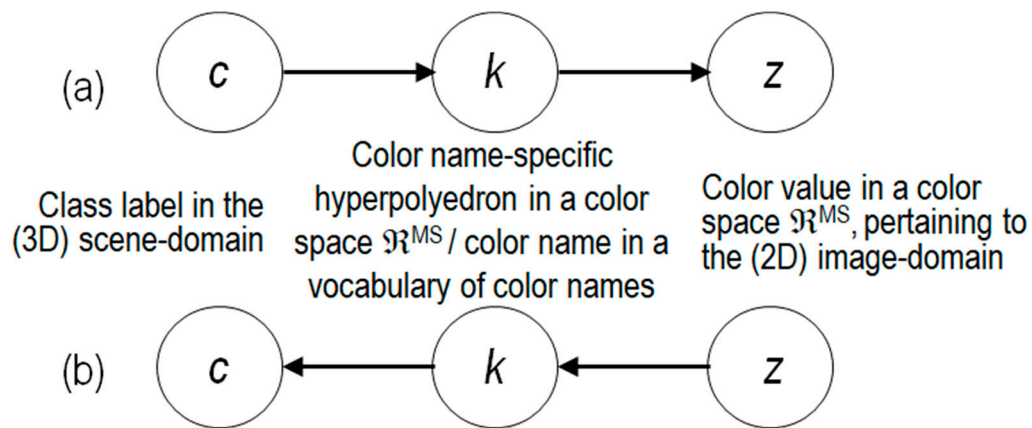
1416 **Figure 20.** Graphical model of color naming, adapted from [169]. Let us consider z as a (sub-
1417 symbolic) numeric variable, such as MS color values of a population of spatial units, with
1418 vector data $z \in \Re^{MS}$, where $\Re^{MS}$ represents the MS data space, while c represents a categorical
1419 variable of symbolic classes in the physical world, with c = 1, ...,
1420 ObjectClassLegendCardinality. (a) According to Bayesian theory, posterior probability $p(c|z)$
1421 $\propto p(z|c)p(c) = p(c) \sum_{ColorName=k=1}^{ColorVocabularyCardinality} p(z|k)p(k|z)$, where color names, equivalent to
1422 color hyperpolyhedra in a numeric color space $\Re^{MS}$, provide a partition of the domain of
1423 change, $\Re^{MS}$, of numeric variable z. (b) For discriminative inference, the arrows in the graphical
1424 model are reversed using Bayes rule. Hence, a vocabulary of color names, physically
1425 equivalent to a partition of a numeric color space $\Re^{MS}$ into color name-specific hyperpolyhedra,
1426 is conceptually equivalent to a latent/ hidden/ hypothetical variable linking observables (sub-
1427 symbolic sensory data) in the real world, specifically, color values, to a categorical variable of
1428 semantic (symbolic) quality in the mental model of the physical world (world ontology, world
1429 model).

1430 ➤ Equation (2) shows that for any spatial unit x in the image-domain, when a hierarchical
1431 CV classification approach estimates posterior m(c| ColorValue(x), ShapeValue(x),
1432 TextureValue(x), SpatialRelationships(x, Neigh(x))) starting from an *a priori* knowledge-
1433 based near real-time color naming first stage, where condition m_1(ColorValue(x)|
1434 ColorName*) = 1 holds, if condition m_2(ColorName*| c) = 0 is true according to a static
1435 community-agreed binary relationship R: VocabularyOfColorNames ⇒
1436 LegendOfObjectClassNames (and vice versa) known *a priori* at first stage, see Table 6, then
1437 the output membership function m(c| ColorValue(x), ShapeValue(x), TextureValue(x),
1438 SpatialRelationships(x, Neigh(x))) = 0 irrespective of any second-stage assessment of
1439 spatial terms ShapeValue(x), TextureValue(x) and SpatialRelationships(x, Neigh(x)),
1440 whose computational model is typically difficult to find and computationally expensive.
1441 Intuitively, Equation (2) shows that first-stage static color naming of any spatial unit x in
1442 the image-domain, either (0D) pixel, (1D) line or (2D) polygon, allows the color-based
1443 stratification of unconditional multivariate spatial variables into color class-conditional
1444 multivariate data distributions, in agreement with the statistic stratification principle [130]
1445 and the divide-and-conquer (*dividi-et-impera*) problem solving approach [29, 30, 32]. Well
1446 known in statistics, the principle of statistic stratification guarantees that "stratification will
1447 always achieve greater precision provided that the strata have been chosen so that
1448 members of the same stratum are as similar as possible in respect of the characteristic of
1449 interest" [130].

1450 At the levels of understanding of system design, algorithm and implementation, the
1451 AutoCloud+ CV subsystem requirements specification listed above is ambitious, but realistic,
1452 because AutoCloud+ can rely upon several CV ⊃ EO-IU software units (modules) already
1453 implemented, tested (by their authors) and validated (by independent third-parties) in recent
1454 years [10-12]. These existing CV ⊃ EO-IU software units can be combined according to an

1455   original six-stage hybrid feedback EO-IU system architecture, hereafter identified as
1456   QuickMap™ technology, see Figure 21, in compliance with the engineering principles of
1457   modularity, hierarchy and regularity considered mandatory by structured system design to
1458   guarantee scalability [32]. The six-stage hybrid feedback CV ⊃ EO-IU system shown in Figure
1459   21 constitutes the core of the inference engine required by the closed-loop EO-IU4SQ system
1460   to systematically provide sub-symbolic EO *big data* cubes with meanings (semantics,
1461   intelligence), to transform a traditional DIAS into an innovative AI4DIAS framework, see
1462   Figure 4 [10, 82-86].
1463
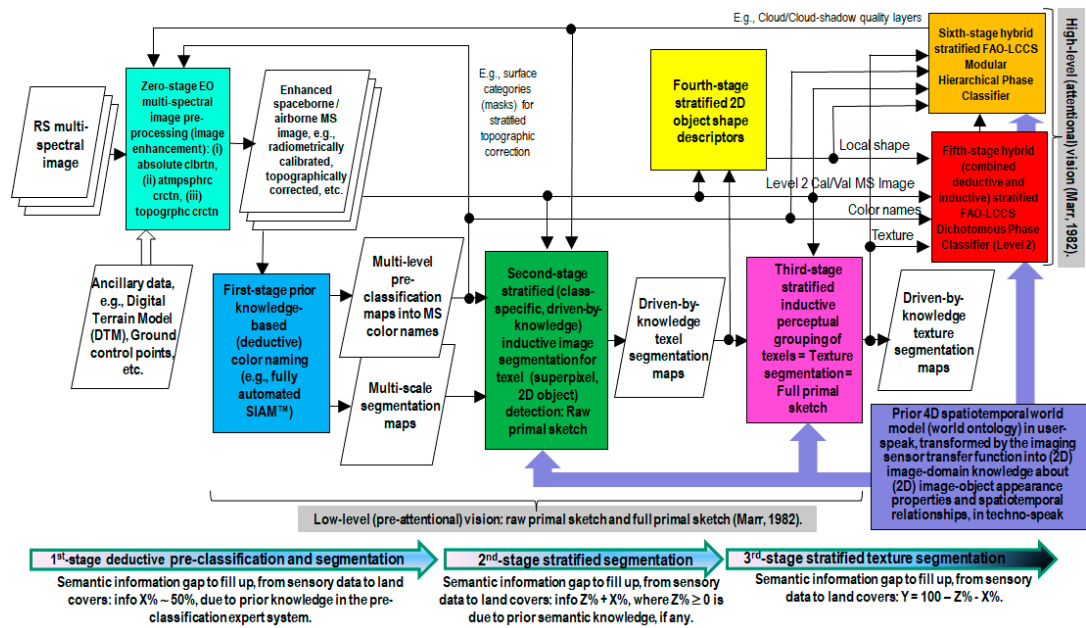
1464   **Figure 21.** Six-stage hybrid (combined deductive and inductive) feedback EO image
1465   understanding (EO-IU) system design, identified as QuickMap™ technology. It is based on a
1466   convergence-of-evidence approach to vision, consistent with Bayesian naïve classification
1467   ([10]). Alternative to inductive feedforward EO-IU system architectures adopted by the RS
1468   mainstream, such as Deep Convolutional Neural Networks (DCNNs) [31], it supports a
1469   hierarchical approach to a first-stage general-purpose, sensor-, application- and user-
1470   independent EO image understanding (classification) subsystem, followed by a second-stage
1471   sensor-, application- and user-specific EO image understanding subsystem, consistent with
1472   the standard two-stage fully-nested Land Cover Classification System (LCCS) taxonomy
1473   promoted by the Food and Agriculture Organization (FAO) of the United Nations, where a
1474   first-stage 3-level 8-class Dichotomous Phase (DP) is preliminary to a second-stage Modular
1475   Hierarchical Phase (MHP) [13]. For the sake of visualization, each of the six data processing
1476   stages plus stage-zero for EO data pre-processing (enhancement) is depicted as a rectangle
1477   with a different color fill. Visual evidence stems from multiple information sources,
1478   specifically, numeric color values quantized into categorical color names, local shape, texture
1479   and inter-object spatial relationships, either topological or non-topological. An example of
1480   first-stage general-purpose, user- and application-independent EO image classification
1481   taxonomy required by an ESA EO Level 2 Scene Classification Map (SCM) product is the 3-
1482   level 8-class FAO LCCS-DP legend, in addition to quality layers cloud and cloud-shadow.
1483   Second-stage EO image classification is user- and application-specific, where an SCM product
1484   of Level 3 or superior is provided with a map legend consistent with the FAO LCCS-MHP
1485   taxonomy [13], see Figure 1. In this figure, acronym SIAM stays for Satellite Image Automatic
1486   Mapper (SIAM), a lightweight computer program for MS reflectance space
1487   hyperpolyhedralization into a static vocabulary of MS color names, superpixel detection and
1488   vector quantization (VQ) quality assessment [10, 11, 12, 76, 78, 79, 91, 113, 114, 138, 139, 151].

1489   At the levels of system understanding of algorithm and implementation, the six-stage
1490   hybrid feedback CV ⊃ EO-IU system architecture shown in Figure 21 employs the following
1491   ensemble of existing CV software functions.

1492 (i)   Zero-stage EO image pre-processing (enhancement), to guarantee multi-source multi-
1493   temporal and multi-angular EO image harmonization and interoperability [10].

1494   I.   Required input data set: MS image provided with a radiometric *Cal* metadata file,
1495   in agreement with the GEO-CEOS QA4EO *Cal* requirements [3].

1496   a. Absolute radiometric *Cal* of DNs into TOARF values, based on
1497   radiometric *Cal* gain and offset metadata parameters.

1498   b. Automated stratified atmospheric, stratified adjacency and stratified
1499   topographic correction (STRATCOR) of TOARF into SURF values, see
1500   Figure 22, e.g., refer to [10, 76].

1501

(a)   (b)

(c)   (d)
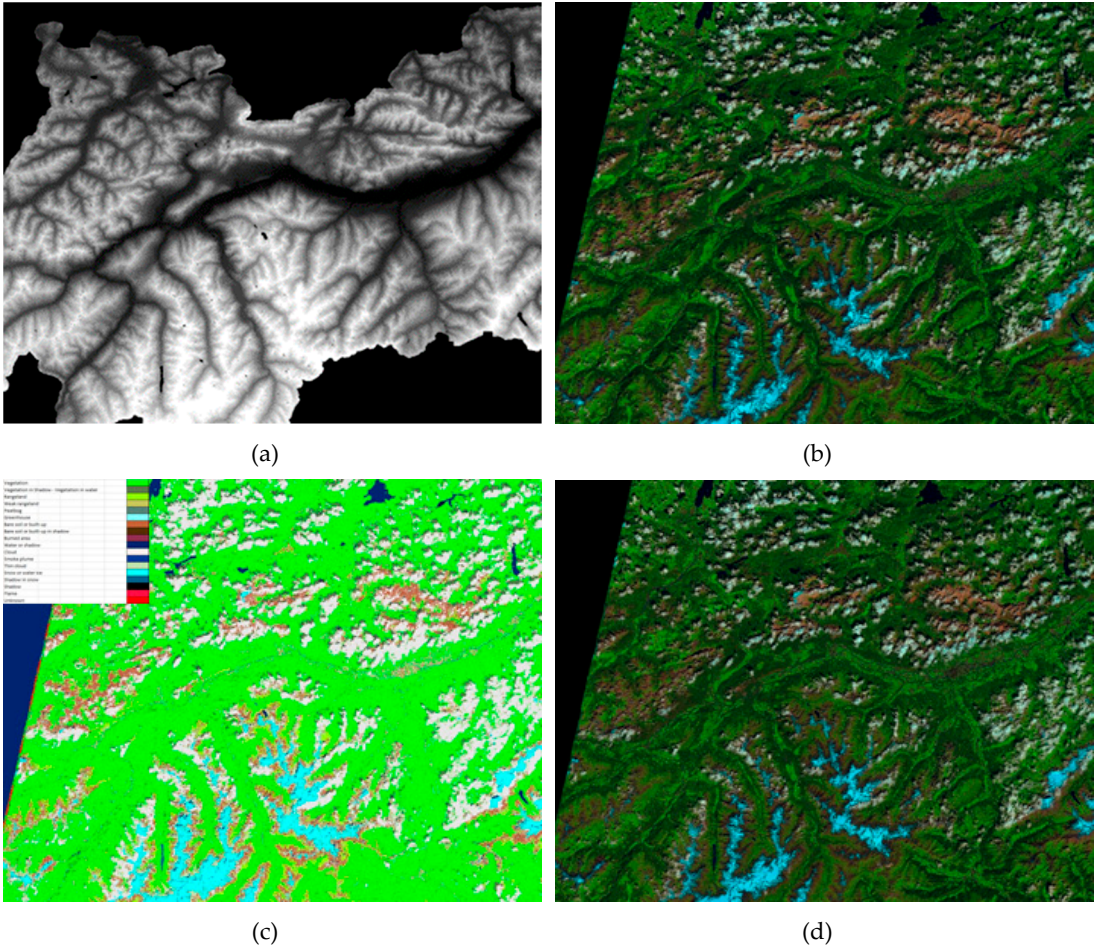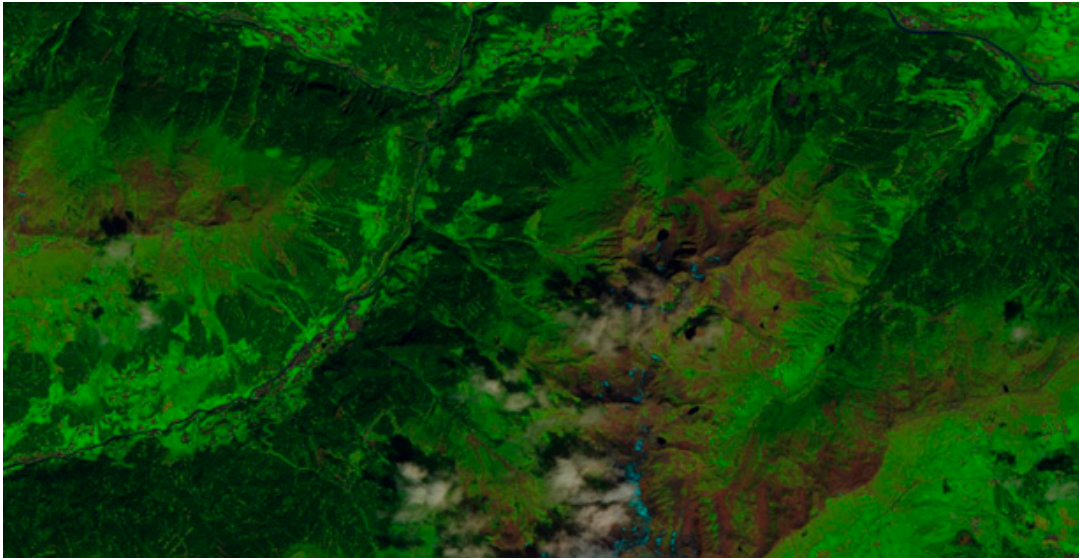
(e)
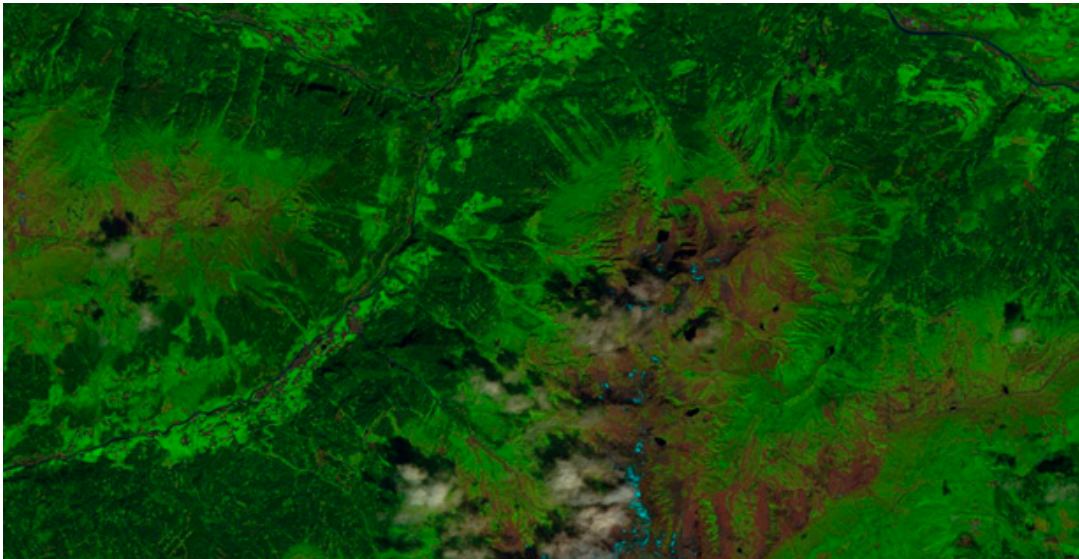
(f)

Figure 22. Automated stratified topographic correction (STRATCOR) of TOARF into SURF values, see Figure 23, e.g., refer to [10, 76]. (a) Input data set 1: Digital Terrain Model (DTM) of Tirol, Austria. 10 m resolution. (b) Input data set 2: Sentinel-2 Multi-Spectral Instrument (MSI) image of Austria (acquisition date: 2016-08-07), depicted in false colors (R: band MIR, G: band NIR, B: band Blue), 10 m resolution, calibrated into TOARF values. No histogram stretching is applied for visualization purposes. (c) Input data set 3: Satellite Image Automatic Mapper (SIAM) output map in color names [10, 11, 12, 76, 78, 79, 91, 113, 114, 138, 139, 151], automatically generated from the input Sentinel-2 image in TOARF values. Output map legend at coarse granularity, 18 spectral categories, depicted in false colors: (d) STRATCOR output product. Sentinel-2 MSI image of Austria, depicted in false colors (R: band MIR, G: band NIR, B: band Blue), 10m resolution, radiometrically calibrated into TOARF values and automatically corrected for topographic effects. No histogram stretching is applied for visualization purposes. (e) Zoom-in of the input image shown in (b). (f) Zoom-in of the output image shown in (d).

II.   Required input data set: panchromatic image or MS image provided with no radiometric *Cal* metadata file. In this case, an inherently ill-posed color constancy

algorithm must be run to guarantee input data interoperability through time, space and sensors, see Figure 23. In human vision, color constancy ensures that the perceived color of objects remains relatively constant under varying illumination conditions, so that they appear identical to a "canonical" (reference) image subject to a "canonical" (known) light source (of controlled quality), e.g., under a white light source [171]. In short, solution of the color constancy problem is the recovery "of an illuminant-independent representation of the reflectance values in a scene" [172]. In practice, color constancy supports image harmonization and interoperability when a radiometric *Cal* metadata file is not available to transform dimensionless DNs into a physical unit of radiometric measure. Computational color constancy is an under-constrained problem in the Hadamard sense [171, 173], hence it is difficult to solve. Since it does not have a unique solution, color constancy requires *a priori* knowledge in addition to sensory data to become better conditioned for numerical solution [30]. Unfortunately, biophysical mechanisms of color constancy remain largely unknown to date. Hence, inherently ill-posed computational color constancy cannot be constrained by prior knowledge of biological color constancy mechanisms to become better posed for numerical solution. For these reasons, there has been a large number of alternative color constancy algorithms proposed in the CV literature in the last 30 years [171, 173]. Inspired by human vision, a novel self-organizing statistical algorithm for multi-band image color constancy was recently implemented, as reported in [10, 174, 175].
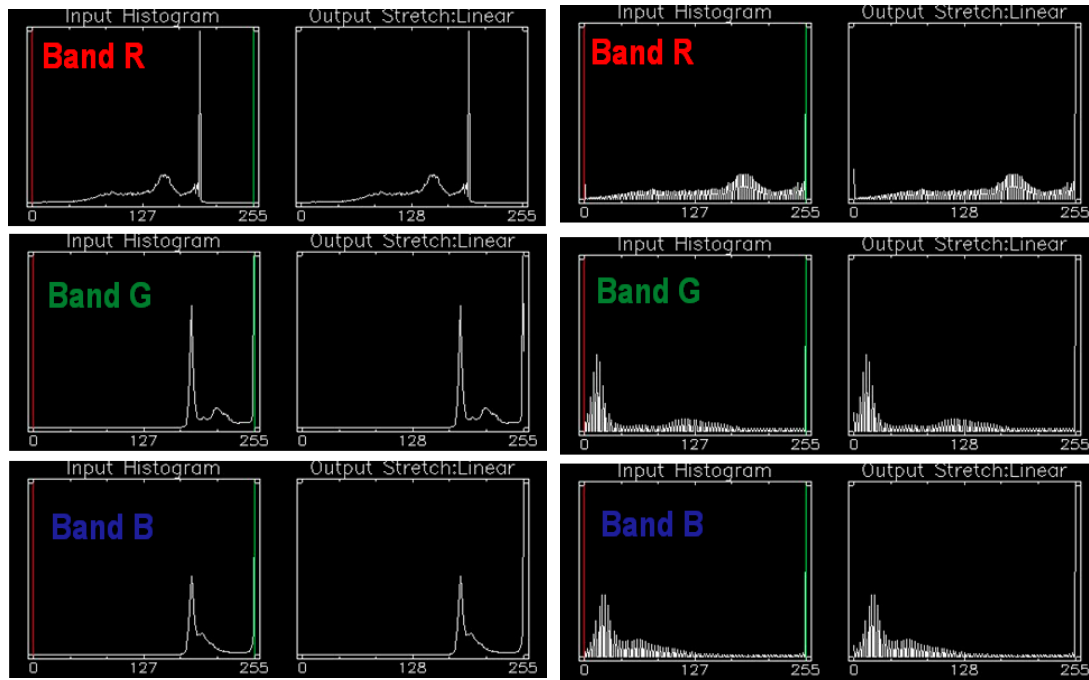
1541 **Figure 23.** Top left: RGB image, source: Akiyoshi Kitaoka @AkiyoshiKitaoka, web page:
1542 http://nymag.com/selectall/2017/02/strawberries-look-red-without-red-pixels-color-
1543 constancy.html. Strawberries appear to be reddish, though the pixels are not. No histogram
1544 stretching is applied for visualization purposes, see the monitor-typical RGB input-output
1545 histograms shown at bottom left. Top right: Output of the self-organizing statistical model-
1546 based color constancy algorithm, as reported in [10, 174, 175], input with the image shown
1547 top left. No histogram stretching is applied for visualization purposes, see the monitor-typical
1548 RGB input-output histograms shown at bottom right.

1549 (ii)   First-stage prior knowledge-based color naming.

1550   I.   Required input data set: MS image radiometrically *Cal* into TOARF, SURF or
1551   surface albedo values. Proposed to the RS community in recent years, the Satellite
1552   Image Automatic Mapper™ (SIAM™) is a lightweight computer program for
1553   automated near real-time MS reflectance space hyperpolyhedralization into MS
1554   color names, superpixel detection and vector quantization (VQ) quality
1555   assessment [10, 11, 12, 76, 78, 79, 91, 113, 114, 138, 139, 151], see Figure 24, Figure
1556   25 and Figure 26. SIAM claims its scalability to MS imaging sensors featuring
1557   different spectral resolution specifications, see Table 7 and Table 8. Moreover, the SIAM's
1558   spectral knowkedge-based decision tree for MS reflectance space hyperpolyhedralization
1559   outperforms its counterparts in terms of spectral quantization capability at different
1560   quantization levels, parameterized by the total number of detected color names at different
1561   levels of color gramularity, see Table 7 in comparison with Table 1 for Sen2Cor, Table 3 for
1562   ATCOR and Table 4 for ATCOR-SPECL. To accomplish a superior scalability to changes in
1563   sensor's specifications and a superior robustness to changes in input data, ranging from
1564   TOARF to SURF and surface albedo values, SIAM features a superior degree of redundancy
1565   of its multivariate spectral rules [11, 12]. For example, among the spectral knowledge-based
1566   decision trees under comparison, the SIAM decision tree is the sole to adopt two different
1567   sets of spectral rules to model the multivariate shape and the multivariate intensity
1568   components of a target manifold (hypervolume) of MS signatures, see Figure 18.

1569
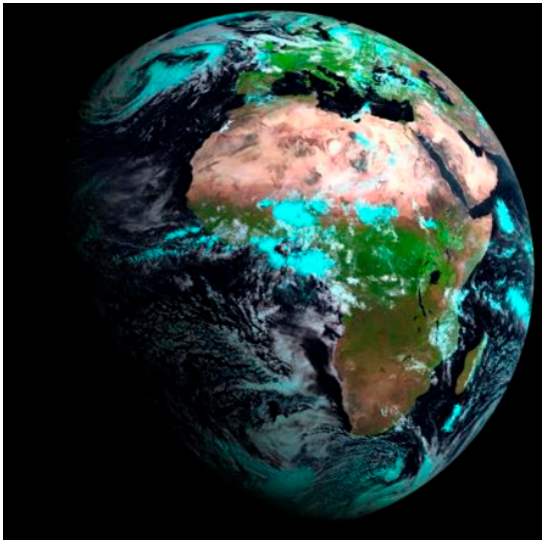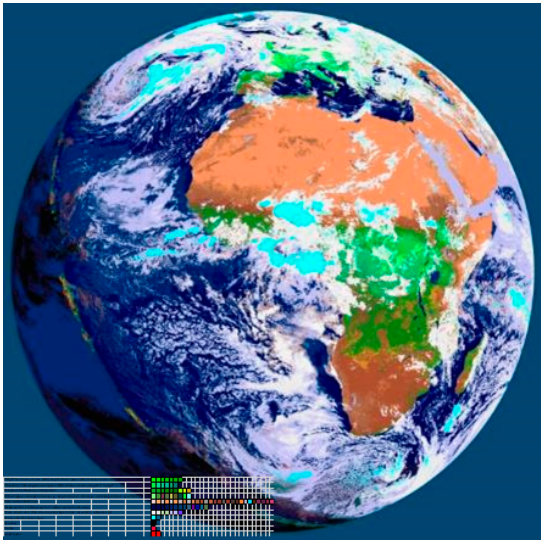
(a)   (b)
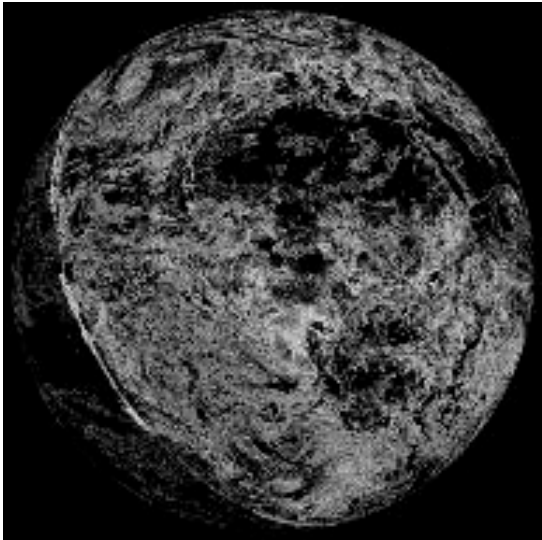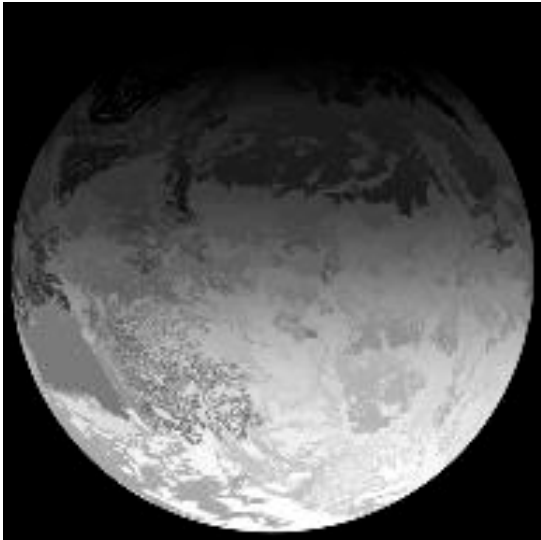
(c)   (d)
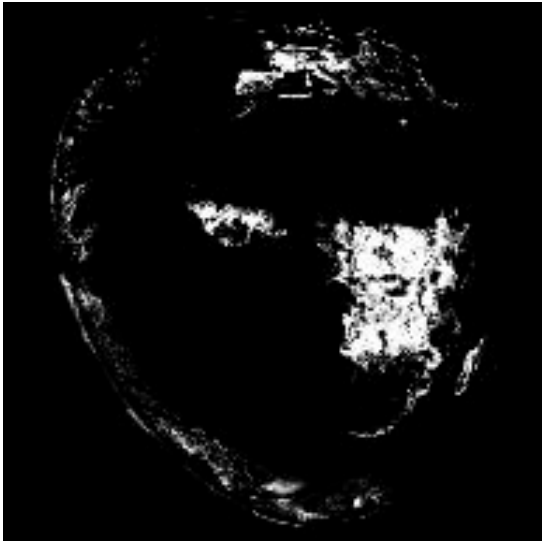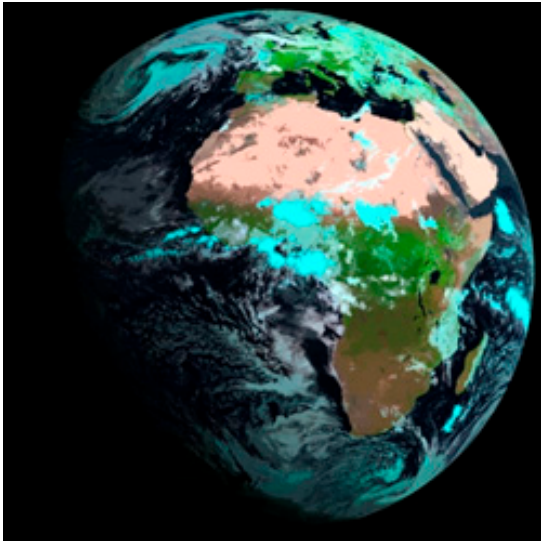
(e)   (f)

Figure 24. (a) Meteosat Second Generation (MSG) SEVIRI image acquired on 2012-05-30, radiometrically calibrated into TOARF values and depicted in false colors (R: band MIR, G: band NIR, B: band Blue), spatial resolution: 3 km. No histogram stretching is applied for visualization purposes. (b). Advanced Very High Resolution Radiometer (AVHRR)-like SIAM (AV-SIAM) hyperpolyhedralization of the MS reflectance hyperspace and prior color map of the input MS image. The AV-SIAM map legend, consisting of 83 ~~~~~~~~~~~~~~ Table
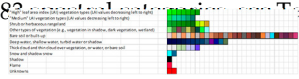
7, is depicted in pseudocolors. Map legend, similar to Table 8:   (c) To visualize contours of image-segments automatically detected in the multi-level SIAM color map-domain by a deterministic two-pass connected-component multi-level image labeling algorithm [16, 176], see Figure 25, an automatic 4- or 8-adjacency cross-aura measure is estimated in linear time, see Figure 26. (d) Segmentation map deterministically generated from the SIAM multi-level output map shown in (b). Each segment is identified by a monotonically increasing (from top to bottom) integer number. (e). Vegetation binary mask, automatically generated from the SIAM multi-level output map shown in (b). On the left, pixel candidates for vegetation belong to spectral category: vegetation in shadow. (f) Piecewise-constant image reconstruction, where each pixel is replaced by the mean reflectance value of the segment that pixel belongs to ("object-mean view"). If the color quantization error (equal to the per-pixel absolute difference between the input image and the piecewise-constant image reconstruction) is "low", then the quality of the prior knowledge-based SIAM's color space partitioning is "high". No histogram stretching is applied for visualization purposes.

Multi-level image, e.g., 3-level thematic map with map legend {1. Water, Acronym = W, Pseudocolor = Blue; 2. Vegetation, Acronym = V, Pseudocolor = Green; 3. Bare soil, Acronym = BS, Pseudocolor = Brown}.

Segmentation map = {S1, …, S9}. Acronym S means segment.
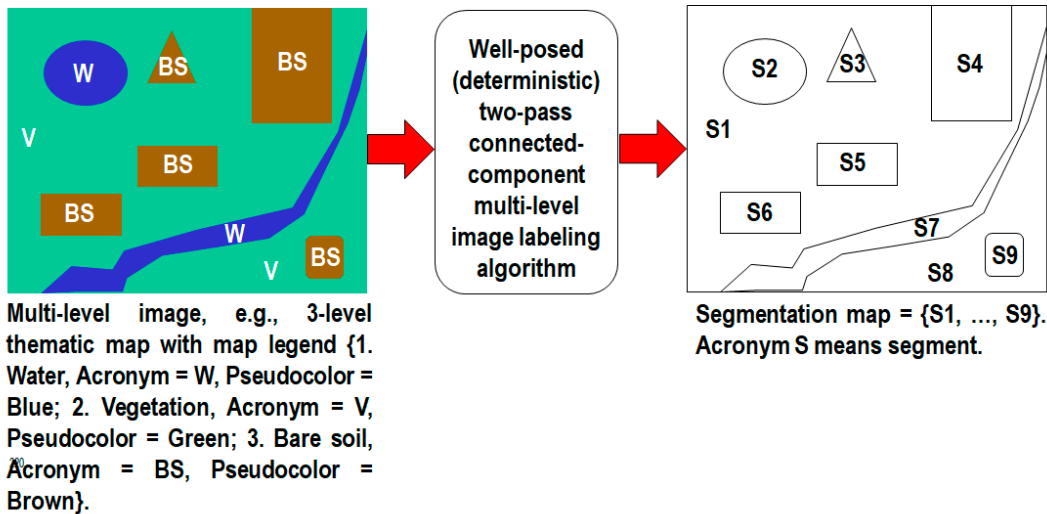
Figure 25. One segmentation map is deterministically generated from one multi-level (e.g., binary) image, such as a thematic map, but the vice versa does not hold, i.e., many multi-level images can generate the same segmentation map. To accomplish the determinist task of segmentation map generation from a multi-level image, the two-pass connected-component multi-level image labeling algorithm [16, 76] requires two raster scans of the input data set. In the figure above, as an example, nine image-objects/segments S1 to S9 can be detected in the 3-level thematic map shown at left. Each segment (image-object) consists of a connected set of pixels sharing the same multi-level map label. An image-object is either (0D) pixel, (1) line or (2D) polygon [168]. Each stratum/layer/level consists of one or more segments, e.g., stratum Vegetation (V) consists of two disjoint segments, S1 and S8. In general, a stratum is a multi-part polygon. Hence, in any multi-level (categorical, nominal, qualitative) image domain, three labeled spatial primitives (spatial units) co-exist and are provided with parent-child relationships: (i) pixel with a level-label and a pixel identifier (ID, e.g., the row-column coordinate pair), (ii) segment (either 0D, 1D, or 2D) with a level-specific label and a segment ID, and (iii) stratum (multi-part polygon) with a level-specific label, equivalent to a stratum ID. This overcomes the ill-fated dichotomy between traditional unlabeled sub-symbolic pixels

1606   versus labeled sub-symbolic segments in the numeric (quantitative) image domain
1607   traditionally coped with by the object-based image analysis (OBIA) paradigm [7].

1608
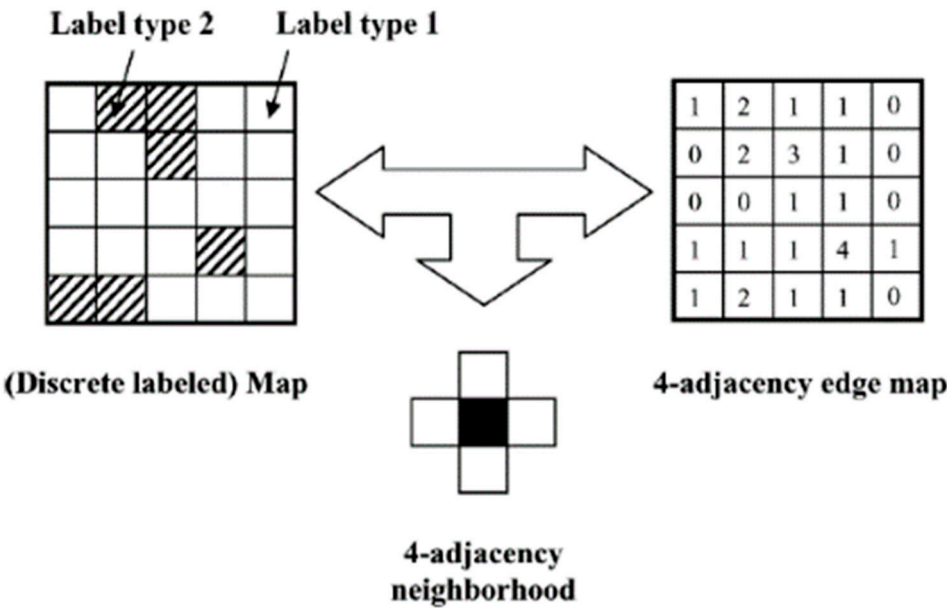
1609   **Figure 26.** Example of a 4-adjacency cross-aura map, shown at right, generated in linear time
1610   from a two-level (binary) image shown at left.

1611   **Table 7**. The SIAM computer program (release 88 version 7) is an EO system of systems
1612   scalable to any past, existing or future MS imaging sensor provided with radiometric
1613   calibration metadata parameters. It encompasses the following subsystems. (i) 7-band
1614   Landsat-like SIAM™ (L-SIAM™), with input channels Blue (B), Green (G), Red (R), Near Infra-
1615   Red (NIR), Medium IR1 (MIR1), Medium IR2 (MIR2), and Thermal IR (TIR). (ii) 4-band
1616   (channels G, R, NIR, MIR1) SPOT-like SIAM™ (S-SIAM™). (iii) 4-band (channels R, NIR,
1617   MIR1, and TIR) Advanced Very High Resolution Radiometer (AVHRR)-like SIAM™ (AV-
1618   SIAM™). (iv) 4-band (channels B, G, R, and NIR) QuickBird-like SIAM™ (Q-SIAM™) [10, 11,
1619   12, 76, 78, 79, 91, 113, 114, 138, 139, 151].

SIAM, r88v7	Input bands	Prior knowledge-based color map legends: Number of output spectral categories = Vocabulary of multi-spectral (MS) color names			
		Fine discretization levels	Intermediate discretization levels	Coarse discretization levels	Inter-sensor discretization levels (*)
L-SIAM	7 – B, G, R, NIR, MIR1, MIR2, TIR	96	48	18	33 (*): employed for inter-sensor post-classification change/no-change detection
S-SIAM	4 – G, R, NIR, MIR1	68	40	15	
AV-SIAM	4 – R, NIR, MIR1, TIR	83	43	17	
Q-SIAM	4 – B, G, R, NIR	61	28	12	

1620
1621   **Table 8**. Legend (vocabulary) of the prior knowledge-based color map generated from a 7-
1622   band MS image (consisting of Landsat-like bands B, G, R, NIR, MIR1, MIR2 and TIR),
1623   radiometrically calibrated into TOARF, SURF or surface albedo values, by the Landsat-like
1624   SIAM (L-SIAM™, release 88 version 7) implementation, also refer to Table 7. For the sake of
1625   representation compactness, pseudo-colors of the 96 spectral categories are gathered along the
1626   same raw if they share the same parent spectral category in the decision tree, e.g., "strong"
1627   vegetation, equivalent to a spectral end-member. The pseudo-color of a spectral category
1628   (color name) is chosen as to mimic natural colors of pixels belonging to that spectral category.

1629

1630

1631   II.   Required input data set: RGB image, either true- or false-color, not provided with
1632   radiometric calibration metadata parameters, but submitted to color constancy.
1633   The RGB Image Automatic Mapper (RGBIAM) is a lightweight computer program
1634   capable of color naming, superpixel detection and VQ quality assessment in non-
1635   calibrated RGB imagery, either true- or false-color, submitted to color constancy
1636   as a mandatory non-calibrated RGB image pre-processing stage for image
1637   harmonization through space, time and sensors. RGBIAM comprises a novel
1638   expert system capable of partitioning a three-band RGB data cube, either true- or
1639   false-color, into a pre-defined vocabulary of RGB color names at two different
1640   quantization levels of color granularity, specifically 50 and 11 color names, see
1641   Figure 27 and Table 9 [10, 174, 175].

1642
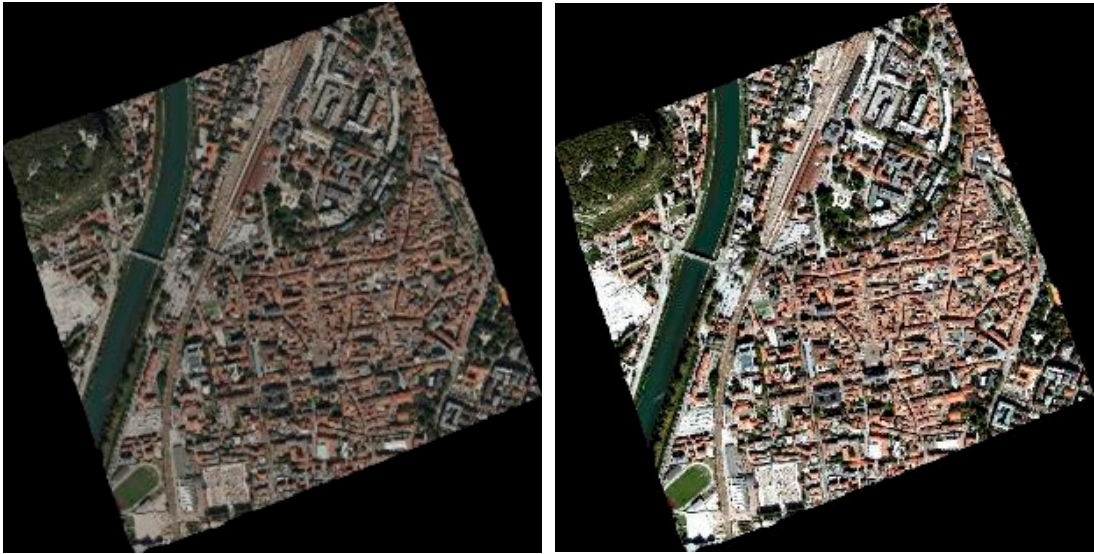
(a)   (b)

(c)   (d)

Figure 27. (a) Airborne 10 cm resolution true-color RGB orthophoto of Trento, Italy, 4017 x 4096 pixels in size x 3 bands, acquired in 2014 and provided with no radiometric calibration metadata file. No histogram stretching is applied for visualization purposes. (b) Same RGB orthophoto subject to self-organizing statistical color constancy. (c) RGBIAM polyhedralization of the RGB color space and prior color map of the RGB image subject to color constancy. The RGBIAM map legend, consisting of 50 spectral categories, is depicted in pseudocolors. Map legend, shown in Table 9: . Input parameters: none. Processing time (one-pass, IDL implementation) = 2 min. (d) To visualize contours of image-segments automatically detected in the multi-level RGBIAM color map-domain by a deterministic two-pass connected-component multi-level image labeling algorithm [16, 176], see Figure 25, an automatic 4- or 8-adjacency cross-aura measure is estimated in linear time, see Figure 26.

Table 9. Legend (vocabulary) of the prior knowledge-based color map generated from a 3-band RGB image, in either true- or false-color and submitted to a color constancy pre-processing stage, by the RGBIAM (release 6 version 2) implementation at fine color quantization with 50 color names (versus 11 basic color names at coarse color space partitioning). For the sake of representation compactness, pseudo-colors of the 50 spectral categories are gathered along the same raw if they share the same parent spectral category in the decision tree. The pseudo-color of a spectral category (color name) is chosen as to mimic natural colors of pixels belonging to that spectral category.

(iii)   Second stage for image-contour detection and image-segmentation (raw primal sketch) [10, 69]. Based on an original physical model-based multi-scale multi-orientation 2D wavelet-based spatial filter bank [10], equivalent to a prior knowledge-based (deductive) CNN alternative to inductive learning-from-data DCNNs currently dominating the CV literature and whose architecture is based on heuristics, the proposed physical model-

1669   based CNN is consistent with constraint 'Human vision → CV ⊃ EO-IU', see Figure 5. In
1670   particular, a CV ⊃ EO-IU subsystem is tested on complex EO spaceborne/airborne images
1671   if and only if it performs in agreement with human visual perception on test cases at
1672   increasing levels of signal complexity, e.g., 1D synthetic signal, (2D) synthetic image,
1673   natural panchromatic imagery and natural color imagery whose "ground truth" is
1674   intuitive to understand, etc. Perceptual criteria to comply with are: (I) the Mach bands
1675   visual illusion [133], see Figure 9, and (II) the perceptual true-fact that human
1676   panchromatic and chromatic vision mechanisms are nearly as effective in scene-from-
1677   image reconstruction and understanding (refer to Section 2). The proposed physical
1678   model-based multi-scale multi-orientation CNN design and implementation satisfy these
1679   perceptual requirements. To reduce computation time, each 2D wavelet-based spatial
1680   filter, $2D\_f(\cdot)$, assumed to be $W \times W$ pixels in size, is implemented as a 2D separable filter,
1681   such that $2D\_f(x,y) = 1D\_g(x) \times 1D\_g(y)$, where the 1D wavelet-based spatial filter, $1D\_g(\cdot)$,
1682   is W pixels in size [140]. Hence, computational complexity of separable per-filter image
1683   convolution is $2W \times$ image size in pixels, rather than $W \times W \times$ image size in pixels. On
1684   theory, four filter orientations (0°, 45°, 90° and 135°) and four dyadic spatial scales, $s = 0$,
1685   …3, are employed, where filter size $W_0 = 2^0 \times 3 = 3$ pixels, $W_1 = 2^1 \times 3 \approx 7$ pixels, $W_2 = 2^2 \times 3$
1686 ≈ 13 pixels and $W_3 = 2^3 \times 3 \approx 25$ pixels. In practice, the same W_0 filter is applied
1687   hierarchically upon the raw image at scale 0 and on three low-pass filtered images,
1688   downscaled by a factor of 2 at scales 1 to 3 [140]. The implemented CNN is capable of: (a)
1689   near-orthogonal image analysis/decomposition and lossless image
1690   synthesis/reconstruction, in analogy with the well-known multi-scale Gaussian and
1691   Laplacian pyramid proposed in [140], (b) automated (requiring no human-machine
1692   interaction) zero-crossing (ZX) image-contour detection ([10]), in line with the biologically
1693   plausible CV system proposed by Marr [69], and (c) automated ZX image-segment (blob,
1694   closed-contour) detection [10], never accomplished by Marr in his seminal work [69], see
1695   Figure 28. Such a deductive CNN implementation is alternative to inductive learning-
1696   from-data algorithms for image-contour detection and image segmentation, either 2D
1697   image analysis approaches, such as DCNNs [31], or 1D image analysis approaches, e.g.,
1698   [134-136], which are inherently semi-automatic and site-specific [2].
1699

(a)   (b)   (c)

(p)   (q)

(r)   (s)   (t)

(u)   (v)
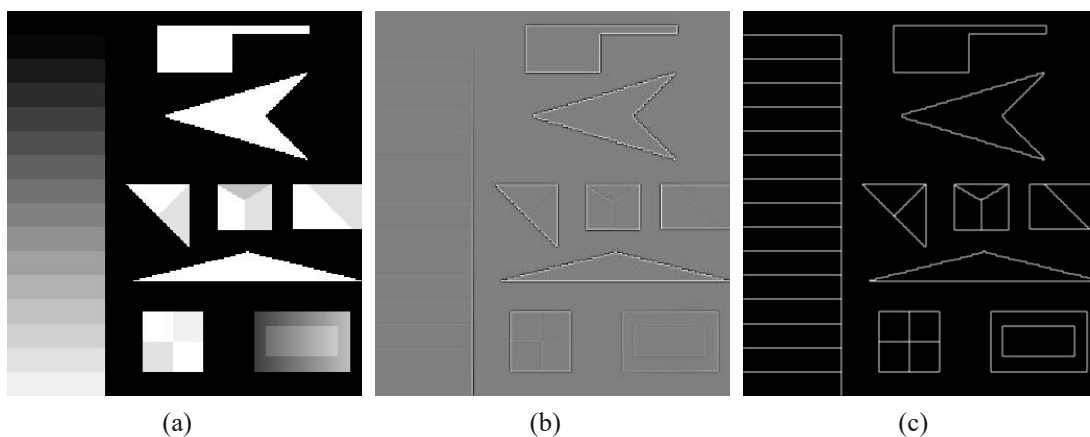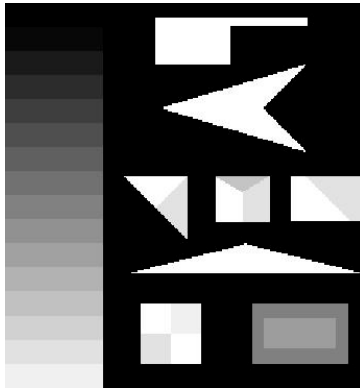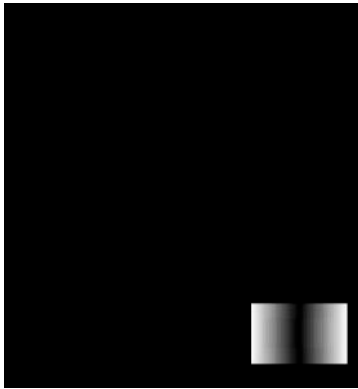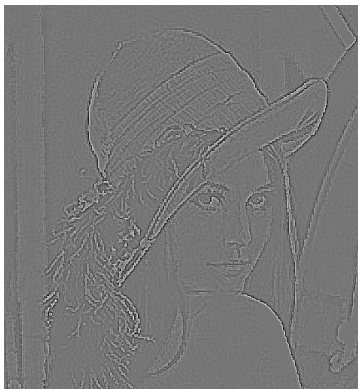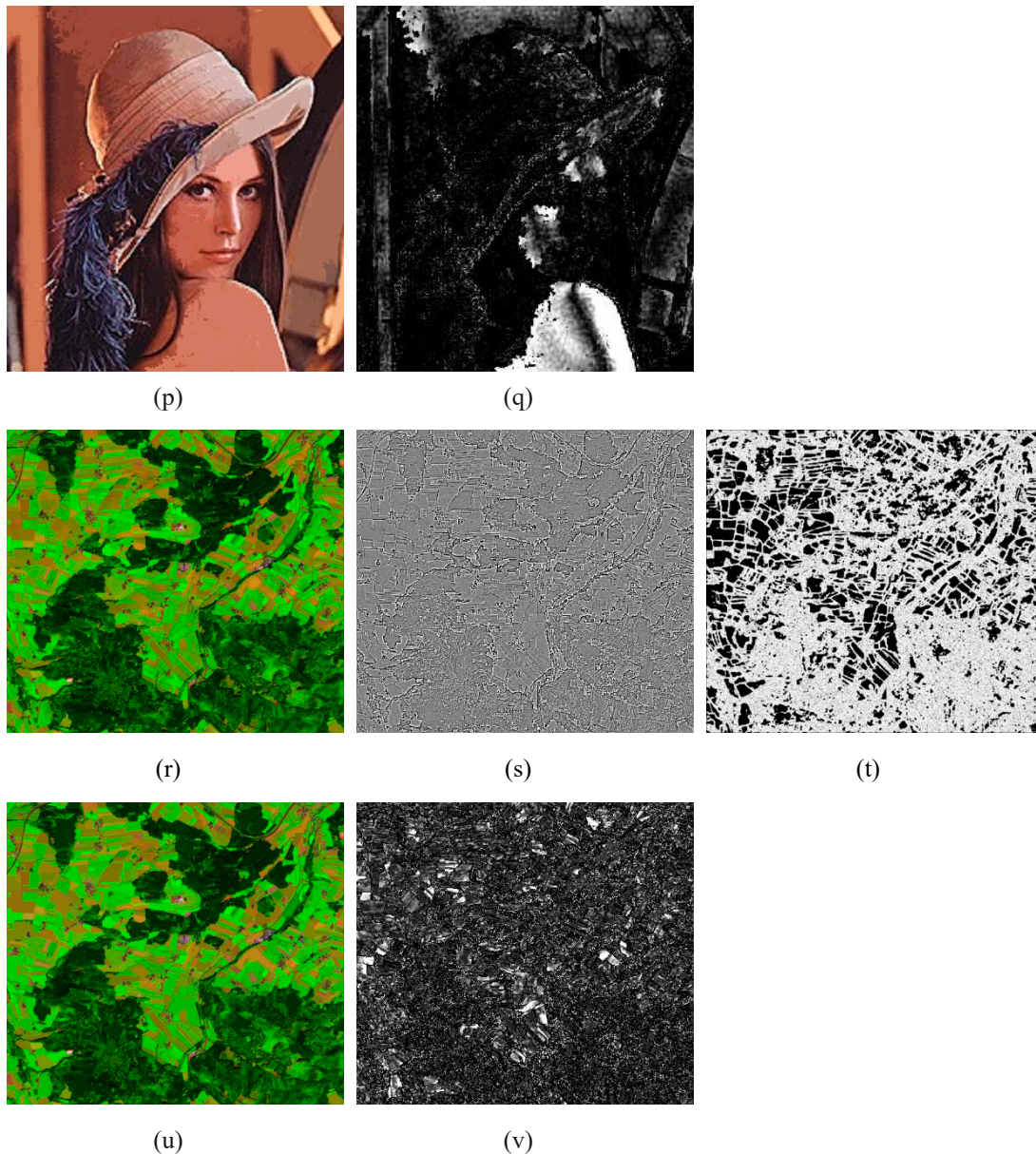
Figure 28. To comply with constraint 'Human vision → CV ⊃ EO-IU', see Figure 5, an EO-IU subsystem for image-contour detection and image segmentation is tested on complex EO spaceborne/airborne images if and only if it performs in agreement with human visual perception, such as: (1) the Mach bands visual illusion [133] and (2) the perceptual true-fact that human panchromatic and chromatic vision mechanisms are nearly as effective in scene-from-image reconstruction and understanding, starting from simpler test of increasing signal complexity, e.g., 1D synthetic signal, 2D synthetic image, natural panchromatic and natural chromatic images of intuitive "ground truth", etc. (a) SUSAN synthetic panchromatic image, byte coded in range {0, 255}. Step edges and ramp edges at known locations (the latter forming the two inner rectangles visible at the bottom right corner) form angles from acute to obtuse. According to human vision, 31 image-segments can be detected as reference "ground-truth". (b) Sum (synthesis) of the wavelet-based near-orthogonal multi-scale multi-orientation image decomposition. Filter value sum in range [-255, +255]. (c) Automated (requiring no human-machine interaction) image segmentation into zero-crossing (ZX) segments generated from ZX pixels detected by a multi-scale multi-orientation spatial filter bank, equivalent to a prior knowledge-based CNN, different from Marr's single-scale isotropic ZX pixel detection ([69]). Exactly 31 image-segments are detected with 100% contour accuracy. Segment contours depicted with 8-adjacency cross-aura values in range {0, 8}, see Figure 26. (d) Image-object mean view = object-wise constant input image reconstruction. (e) Object-wise constant input

1719   image reconstruction compared with the input image, per-pixel root mean square error
1720   (RMSE) in range [0, 255]. (f) Natural panchromatic image of Lenna. (g) Same as (b). (h) Same
1721   as (c), there is no CV system's free- parameter to be user-defined. (i) Same as (d). (l) Same as
1722   (e). (m) Natural RGB-color image of Lenna. (n) Same as (b). (o) Same as (c), there is no CV
1723   system's free- parameter to be user-defined. (p) Same as (d). (q) Same as (e). (r) Zoom-in of a
1724   Sentinel-2A MSI Level-1C image of the Earth surface south of the city of Salzburg, Austria.
1725   Acquired on 2015-09-11. Spatial resolution: 10 m. Radiometrically calibrated into top-of-
1726   atmosphere reflectance (TOARF) values in range {0, 255}, it is depicted as a false color RGB
1727   image, where: R = Medium InfraRed (MIR) = Band 11, G = Near IR (NIR) = Band 8, B = Blue =
1728   Band 2. Standard ENVI histogram stretching applied for visualization purposes. (s) Same as
1729   (b). (t) Same as (c), there is no CV system's free- parameter to be user-defined. (u) Same as (d).
1730   (v) Same as (e).

1731 (iv)   Third stage for planar shape indexing. An original minimally dependent and maximally
1732   informative (mDMI) set of planar shape (geometric) indexes was conceived and
1733   implemented as described in [10, 163]. The proposed mDMI set of geometric functions
1734   comprises scale-invariant roundness (compactness and no holiness) ∈ [0, 1], elongatedness
1735   (and no holiness) ≥ 1, multi-scale straightness of boundaries ∈ [0, 1], simple connectivity
1736   (no holiness) ∈ [0, 1], rectangularity (and no holiness) ∈ [0, 1] and convexity (and no
1737   holiness) ∈ [0, 1], to be estimated per image-object in addition to size and orientation, see
1738   Figure 29.

1739

1740   **Figure 29.** Screenshot of a graphic user interface (GUI) specifically developed to show a human
1741   expert values of the proposed minimally dependent and maximally informative (mDMI) set
1742   of geometric attributes. In this GUI, darker cells correspond to: (i) higher values of geometric
1743   attributes and (ii) lower values of photometric attributes, like the panchromatic mean intensity
1744   shown at the rightest column. In this figure, for reasons of readability only nine segments are
1745   shown simultaneously for comparison. Detected in the spaceborne VHR test image of an urban
1746   area, segments 1 through 6 correspond to buildings or parts of buildings while segments 7
1747   through 9 belong to roads. These two families of segments appear easy to discriminate based
1748   on different combinations of ranges of change of their geometric attributes.

1749 (v)   Fourth stage for texture segmentation (full primal sketch), synonym of perceptual spatial
1750   grouping of texture elements, texels [10, 16, 164-166] or tokens [69]. Based on a multi-scale
1751   texture binary profile accomplished in linear time complexity via multi-scale window-
1752   based analysis of the spatial distribution of binary image-contours [10]. To date, automated
1753   image-texture segmentation is an open problem [20, 68, 141, 177].

1754 (vi)   Fifth stage for general-purpose, user- and application-independent ESA EO Level 2
1755   product generation (refer to Section 1), based on a 2D convergence-of-visual-evidence
1756   approach, according to Equation (2) [10], where the proposed ESA EO Level 2 SCM
1757   product taxonomy consists of a standard 3-level 8-class FAO LCCS-DP legend augmented
1758   with quality layers cloud and cloud-shadow, see Table 2 and Figure 1.

1759 (vii)   Sixth stage for user- and application-dependent FAO LCCS-MHP classification (see Figure
1760   1), based on a 2D convergence-of-visual-evidence approach, according to Equation (2) [10].

1761   At the levels of system understanding of information/knowledge representation, system
1762   architecture, algorithm and implementation, the AutoCloud+ subsystem requirements
1763   specification is considered a specialized version of the aforementioned six-stage hybrid
1764   feedback CV system baseline. In greater detail, the AutoCloud+ flow chart, algorithm and
1765   implementation are specialized as follows [10, 36, 67], see Figure 30.
1766
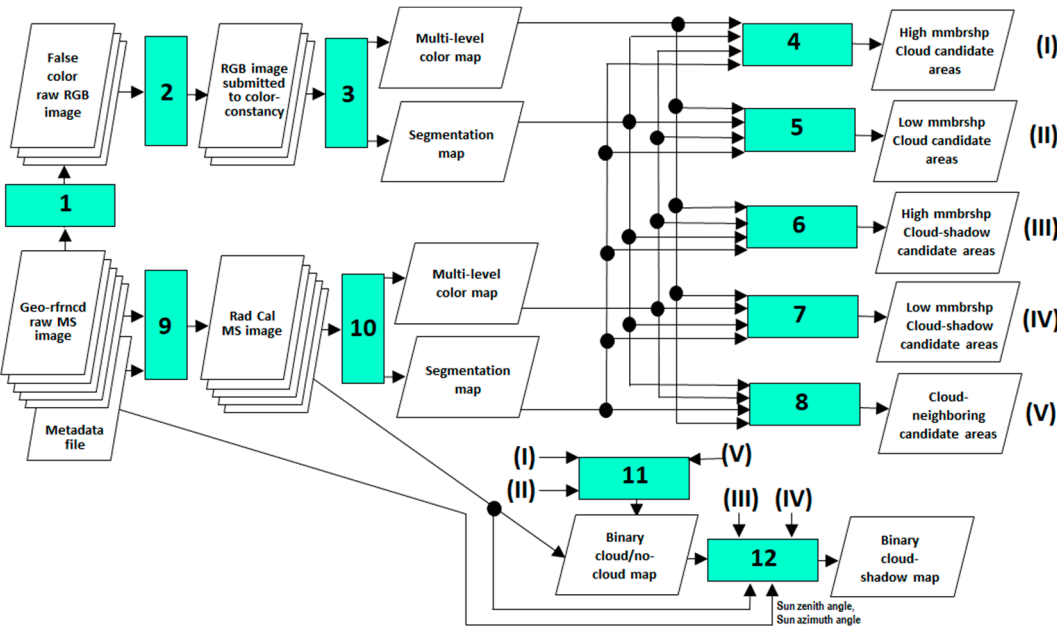
1767   **Figure 30.** AutoCloud+ hybrid (combined physical model-based and statistical model-based)
1768   2D image analysis system design (architecture) for spatial context-sensitive and spatial
1769   topology-preserving cloud/cloud-shadow detection. (1) True- or false-color RGB channel
1770   selection. (2) Statistical self-organizing color constancy algorithm. (3) RGBIAM lightweight
1771   computer program for RGB color space polyhedralization into color names, superpixel
1772   detection and vector quantization (VQ) quality assessment. (4) Candidate cloud areas, based
1773   on convergence-of evidence. (5) Candidate no-cloud areas, based on convergence-of evidence.
1774   (6) Candidate cloud-shadow areas, based on convergence-of evidence. (7) Candidate no-cloud-
1775   shadow areas, based on convergence-of evidence. (8) Candidate cloud neighboring areas,
1776   based on convergence-of evidence. (9) Radiometric calibration of digital numbers (DNs) into
1777   TOARF, SURF or surface albedo values. (10) SIAM lightweight computer program for MS
1778   reflectance space hyperpolyhedralization into color names, superpixel detection and vector
1779   quantization (VQ) quality assessment. (11) Spatial cloud modeler: Clouds detected from
1780   candidate cloud and cloud neighboring areas. (12) Spatial bidirectional cloud and cloud-

shadow modeler: Physical model-based cloud shadow detection, moving from cloud to cloud-shadow candidates and vice versa, for mutual reinforcement learning.

First, the two SIAM and RGBIAM lightweight computer programs for color space discretization into color names are combined to pursue convergence of photometric evidence, whether or not the color space is radiometrically calibrated. For example, when the input MS image is radiometrically calibrated into TOARF, SURF or surface albedo values, then SIAM and RGBIAM are run in parallel upon, respectively, the original input MS image (calibrated) and an RGB false-color selection of the input (calibrated) image pre-processed by the self-organizing algorithm for color constancy (similar to image enhancement by histogram stretching). The two output multi-level maps in color names generated as output by SIAM and RGBIAM can be deterministically segmented in linear time complexity with image size into labeled image-objects (super-pixels, connected sets of pixels featuring the same color label) by a well-known two-pass connected-component multi-level image labeling algorithm [16, 176], see Figure 25. In the SIAM and RGBIAM output segmentation map, each connected-component is labeled with one segment identifier (ID) together with one semi-symbolic color name. For example, an image-object, either (0D) pixel, (1) line or (2D) polygon [168], is provided with a segment ID, a MS color name 'green-as-Vegetation' by SIAM and an RGB color name 'Green' by RGBIAM.

Second, candidate cloud-objects and candidate cloud-shadow-objects are detected in the image-domain based on a convergence of spatial shape and size properties with SIAM and RGBIAM color names. Stratified (class-conditioned) by color names, a driven-by-knowledge shape-preserving dilation process is run to fill small spatial gaps within cloud/cloud-shadow candidate areas (e.g., due to self-occlusion and shadow-casting phenomena occurring in clouds, where solar luminance decreases) and along boundaries of candidate cloud areas.

Third, the cloud candidate image-objects can grow in the image-domain to include spatially adjacent image-objects whose color, shape and size properties are consistent with the hypothesis of belonging to class crown-of-cloud.

Finally, a bidirectional physical knowledge-based data modeler is run for spatial reasoning (see software blocks identified as 11 and 12 in Figure 30). Making use of OBIA concepts for spatial information modeling [178], it is capable of cloud/cloud-shadow image-object pair spatial matching in shape while accounting for the sun position, to reduce cloud and cloud-shadow false positives and false negatives. In the quest for a unidirectional cloud-to-cloud-shadow relationship, candidate cloud-shadows are searched for in the (2D) image-domain to be matched in shape by each individual candidate cloud-object adopted as starting position. This spatial search moves from the candidate cloud-object of interest, in the direction of the sun azimuth angle (known from the input EO image metadata file) with orientation away from the sun, for a spatial length estimated as a dependent variable of the cloud height, which is the sole unknown independent physical variable to cope with, estimated according to an *a priori* physical knowledge-based model of real-world cloud heights, in line with Sen2Cor [9]. The dual quest for object-pair matching in shape deals with the cloud-shadow-to-cloud unidirectional relationship, which is usually neglected in other cloud/cloud-shadow detectors, such as Sen2Cor [9] and MAJA ([39]). A simplified flow chart of the hybrid AutoCloud+ software toolbox for automated cloud/cloud-shadow detection is shown in Figure 31.

At the implementation level of system understanding, it is worth mentioning that candidate cloud/cloud-shadow image-object pairs are matched in shape according to the mDMI set of planar shape functions implemented in [10, 163]. The AutoCloud+ software blocks identified as data processing units 4 to 8, 11 and 12 in Figure 30 were implemented within the Trimble's eCognition Developer commercial software environment for fast prototyping OBIA solutions [179].
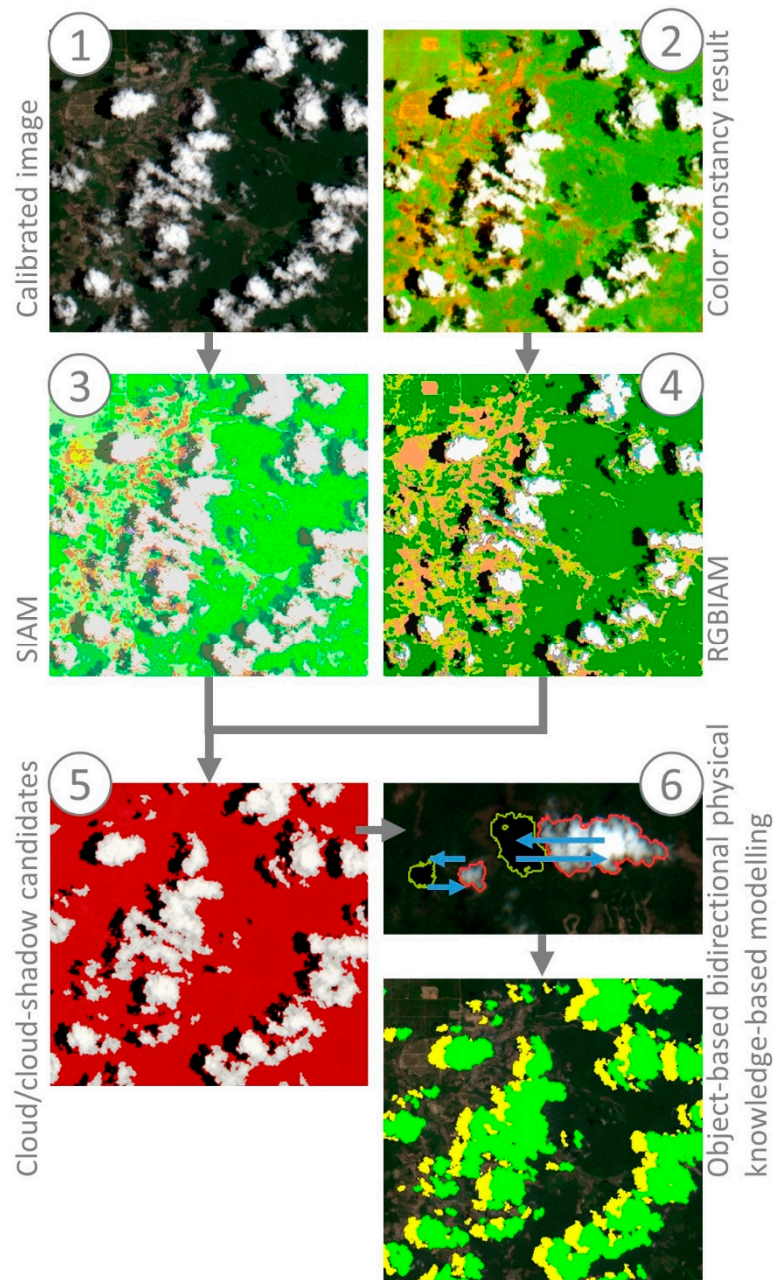
1831   **Figure 31.** Simplified flow chart of the hybrid AutoCloud+ software toolbox for automated
1832   cloud/cloud-shadow detection, see Figure 30. This intuitive workflow is depicted as a sequence
1833   of two input data sets (1) and (2), generated from the same input MS image, one submitted to
1834   radiometric *Cal* (when radiometric *Cal* metadata parameters are available) and the other
1835   submitted to statistical color constancy, followed by four intermediate information products
1836   (3) to (6), and one final output product, specifically, a three-level output map with semantic
1837   layers cloud/cloud-shadow/others (rest of the world), shown at bottom right.

1838   **5. Materials**

1839   For testing purposes, the novel AutoCloud+ algorithm for cloud/cloud-shadow detection
1840   in single-date MS imagery was compared in quantitative terms of outcome and process quality,
1841   in compliance with the mDMI set of EO OP-Q²Is proposed in Section 2, with alternative
1842   standard CV software solutions available open source or free of cost, specifically, the single-
1843   date Sen2Cor and multi-temporal MAJA software toolboxes.

1844   As proof of concept, AutoCloud+, Sen2Cor and MAJA (refer to Table 5) were compared
1845   upon two test images, selected to be representative of the complexity of the cloud/cloud-
1846   shadow detection problem in real-world situations.
1847   The first test image was selected as a Sentinel-2 A (S2A) Multi-Spectral Instrument (MSI)
1848   Level 1C image radiometrically calibrated into TOARF values, depicting an Earth-surface area
1849   located   in   Cambodia   (Product   ID:
1850   S2A_MSIL1C_20170421T031541_N0204_R118_T48PWV_20170421T033212), see Figure 32, for
1851   which Sen2Cor and MAJA results were available for download from the Copernicus Open
1852   Access Hub (https://scihub.copernicus.eu/dhus/#/home) and from the CNES website
1853   (https://theia.cnes.fr/atdistrib/rocket/#/search?collection=SENTINEL2) respectively. This first
1854   test image shows a large variety of cloud patterns, varying in shape, size and cloud height,
1855   together with typical critical elements in cloud and cloud-shadow detection, such as cloud-
1856   shadows projected over water and vegetated surface types, in addition to occluded cloud and
1857   cloud-shadow phenomena.
1858   A second test image was identified in a Sentinel-2 B (S2B) Level 1C image radiometrically
1859   calibrated into TOARF values, depicting an Earth-surface area located in the Alpine area
1860   between   Austria   and   Germany   (Product   ID:
1861   S2B_MSIL1C_20180616T102019_N0206_R065_T32TPT_20180616T154713), see Figure 32. In
1862   this second test image, potential critical elements in cloud/cloud-shadow detection are the
1863   presence of snow/ice patterns in high-elevation areas, eligible for confusion with ice clouds, of
1864   clouds located next to visible snow/ice surface types and of Earth surfaces affected by shadows
1865   casted by mountains rather than clouds. For this second test image no MAJA mapping result
1866   was available for download from the aforementioned CNES website.
1867
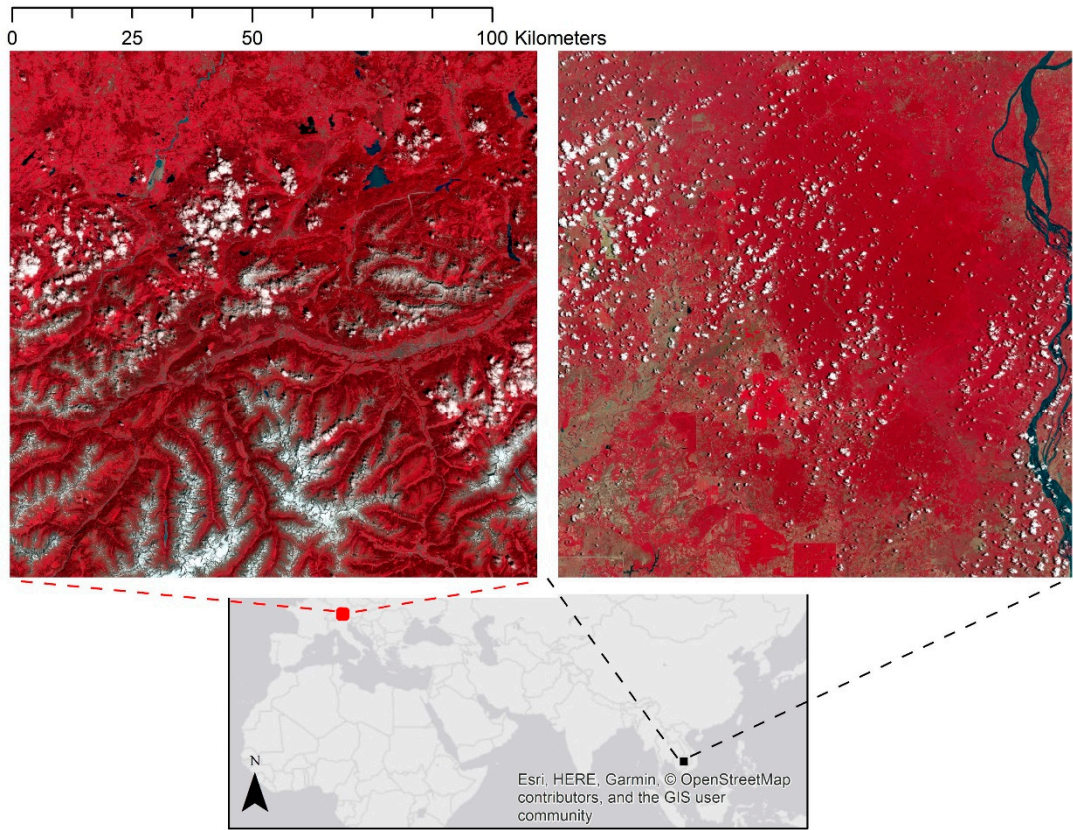
1868   **Figure 32.** Overview of the two study areas adopted for testing (Left: Cambodia test site, Right:
1869   Alpine test site located between Austria and Germany). EO images of these two test areas must
1870   be selected to be representative of the complexity of the cloud/cloud-shadow detection
1871   problem in real-world situations. At left, second test image, identified as a Sentinel-2 B Multi-
1872   Spectral Instrument (MSI) Level 1C image, radiometrically calibrated into TOARF values,

1873   depicted in false-colors: monitor-typical RGB channels are selected as R = Near InfraRed (NIR)
1874   channel, G = Visible Red channel, B = Visible Green channel. Histogram stretching is applied
1875   for   visualization   purposes.   Product   ID:
1876   S2B_MSIL1C_20180616T102019_N0206_R065_T32TPT_20180616T154713. At right, first test
1877   image, identified as Sentinel-2 B MSI Level 1C image, radiometrically calibrated into TOARF
1878   values, and depicted in false-colors as the second test image shown at left. Product ID:
1879   S2A_MSIL1C_20170421T031541_N0204_R118_T48PWV_20170421T033212.

1880   **6. Results**

1881   Alternative cloud/cloud-shadow output maps generated by the single-date AutoCloud+,
1882   single-date Sen2Cor and multi-temporal MAJA software toolboxes were compared in
1883   quantitative terms of outcome quality, as defined in the mDMI set of EO OP-Q²Is proposed in
1884   Section 2. In addition, the AutoCloud+ CV subsystem was assessed in quantitative terms of
1885   process quality, as defined in the mDMI set of OP-Q²Is proposed in Section 2. Noteworthy, this
1886   quality assurance strategy goes far beyond the traditional quantitative assessment policy of
1887   EO-IU systems presented in the RS literature, almost exclusively limited to mapping accuracy.
1888   With regard to process quality indicators defined in the mDMI set of OP-Q²Is proposed
1889   in Section 2, such as degree of automation and computation time, AutoCloud+ ran
1890   automatically (without human-machine interaction) upon the two test images, where Step 1 to
1891   Step 5 in Figure 31 were computed in near real-time, specifically, in linear time complexity
1892   with image size, equal to around 2 minutes per Sentinel-2 image in a standard laptop
1893   computer. The bidirectional object-based cloud/cloud-shadow spatial modeler, shown as Step
1894   6 in Figure 31 and prototyped in the Trimble eCognition software, depends on the number of
1895   cloud and cloud-shadow candidate image-objects detected in the image-domain at Step 5. For
1896   each of the two Sentinel-2 images selected for testing, the eCognition software prototype at
1897   Step 6 ran in a reasonable time frame, around 5 minutes per input image.
1898   With regard to outcome quality indicators defined in the mDMI set of OP-Q²Is proposed
1899   in Section 2, enhanced input images, either radiometrically calibrated into TOARF values or
1900   submitted to color constancy, and intermediate SIAM's and RGBIAM's output maps generated
1901   from the first Sentinel-2 test image are shown in Figure 33. Final cloud/cloud-shadow output
1902   maps generated by the single-date AutoCloud+, single-date Sen2Cor and multi-temporal
1903   MAJA computer programs are shown in Figure 34, zoomed-in in Figure 35 and extra zoomed-
1904   in in Figure 36. Table 10 reports on the total area of clouds and cloud-shadows detected by the
1905   three algorithms of interest in the first test image.
1906

(a)   (b)

(c)   (d)
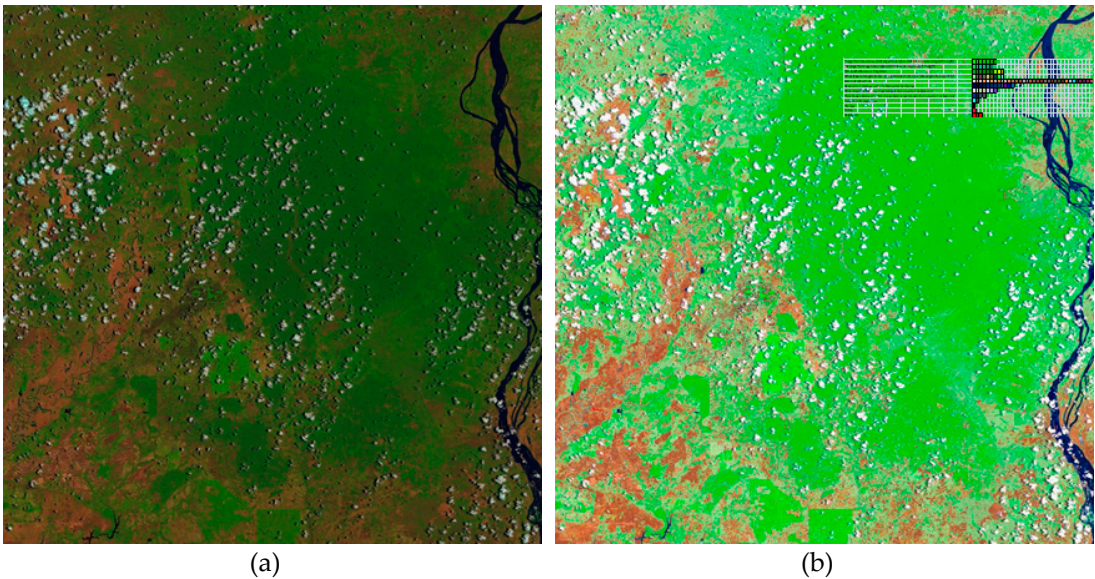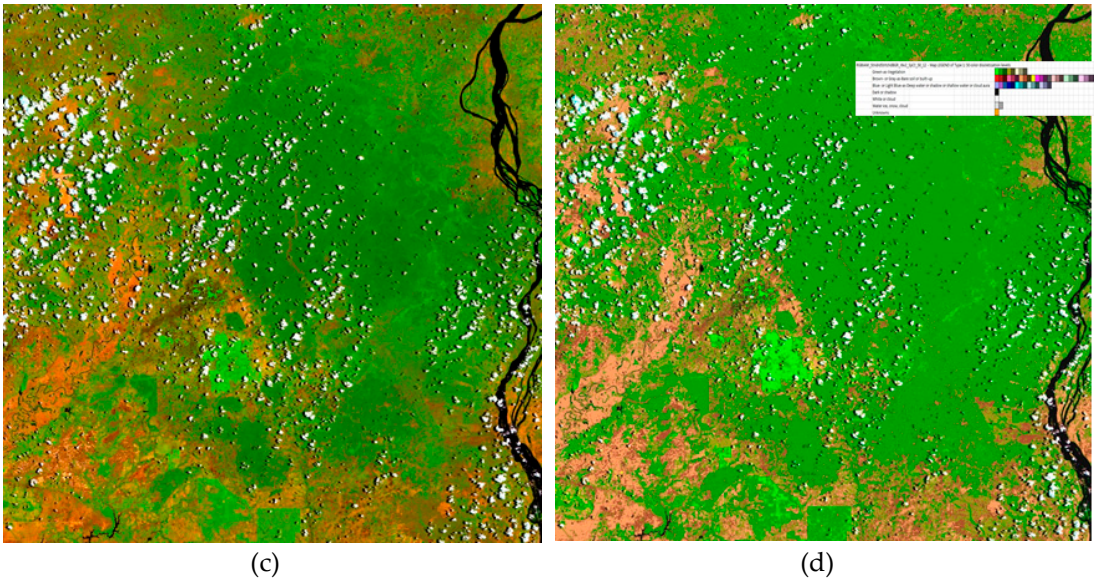
1907 **Figure 33.** (a) First test image of a Cambodia site. Sentinel-2 A Multi-Spectral Instrument (MSI)
1908 Level 1C image of Cambodia, radiometrically calibrated into TOARF values. Acquisition date:
1909 2018-06-16. Depicted in false-colors: monitor-typical RGB channels are selected as R = Medium
1910 InfraRed (MIR) channel, G = Near InfraRed (NIR) channel, B = Visible Blue channel. No
1911 histogram stretching is employed for visualization purposes. (b) SIAM map of the test S2
1912 image shown in (a). SIAM map legend: 96 color names, depicted in pseudocolors as follows
1913 (see Table 8):   (c) First test image, shown in (a), submitted to a
1914 self-organizing color constancy algorithm. Depicted in false-colors: monitor-typical RGB
1915 channels are selected as R = Medium InfraRed (MIR) channel, G = Near InfraRed (NIR)
1916 channel, B = Visible Blue channel. No histogram stretching is employed for visualization
1917 purposes. (d) RGBIAM map of the test S2 image shown in (c). RGBIAM map legend: 50 color
1918 names, depicted in pseudocolors as follows (see Table 9):   .
1919
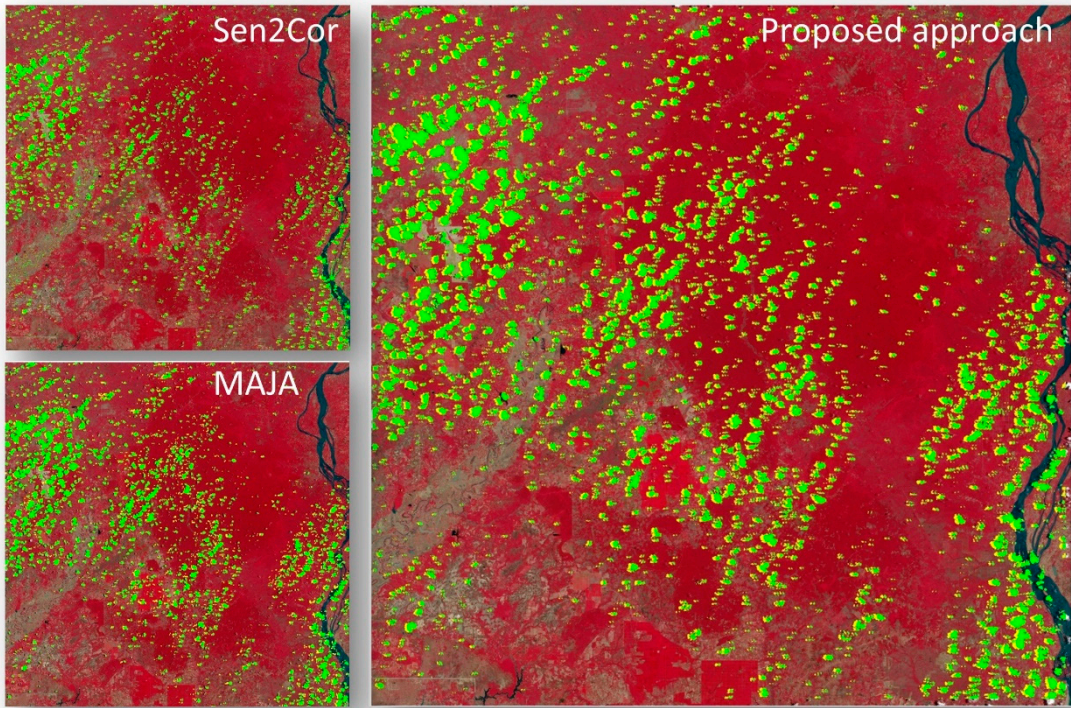
Figure 34. First test image of a Cambodia site. Final 3-level cloud/cloud-shadow/others maps generated by the three algorithms under comparison, specifically, single-date AutoCloud+, single-date Sen2Cor and multi-date MAJA, where class "others" is overlaid with the input Sentinel-2 A Multi-Spectral Instrument (MSI) Level 1C image, radiometrically calibrated into TOARF values and depicted in false-colors: monitor-typical RGB channels are selected as R = Near InfraRed (NIR) channel, G = Visible Red channel, B = Visible Green channel. Histogram stretching is applied for visualization purposes. Output class cloud is shown in a green pseudocolor, class cloud-shadow in a yellow pseudocolor.
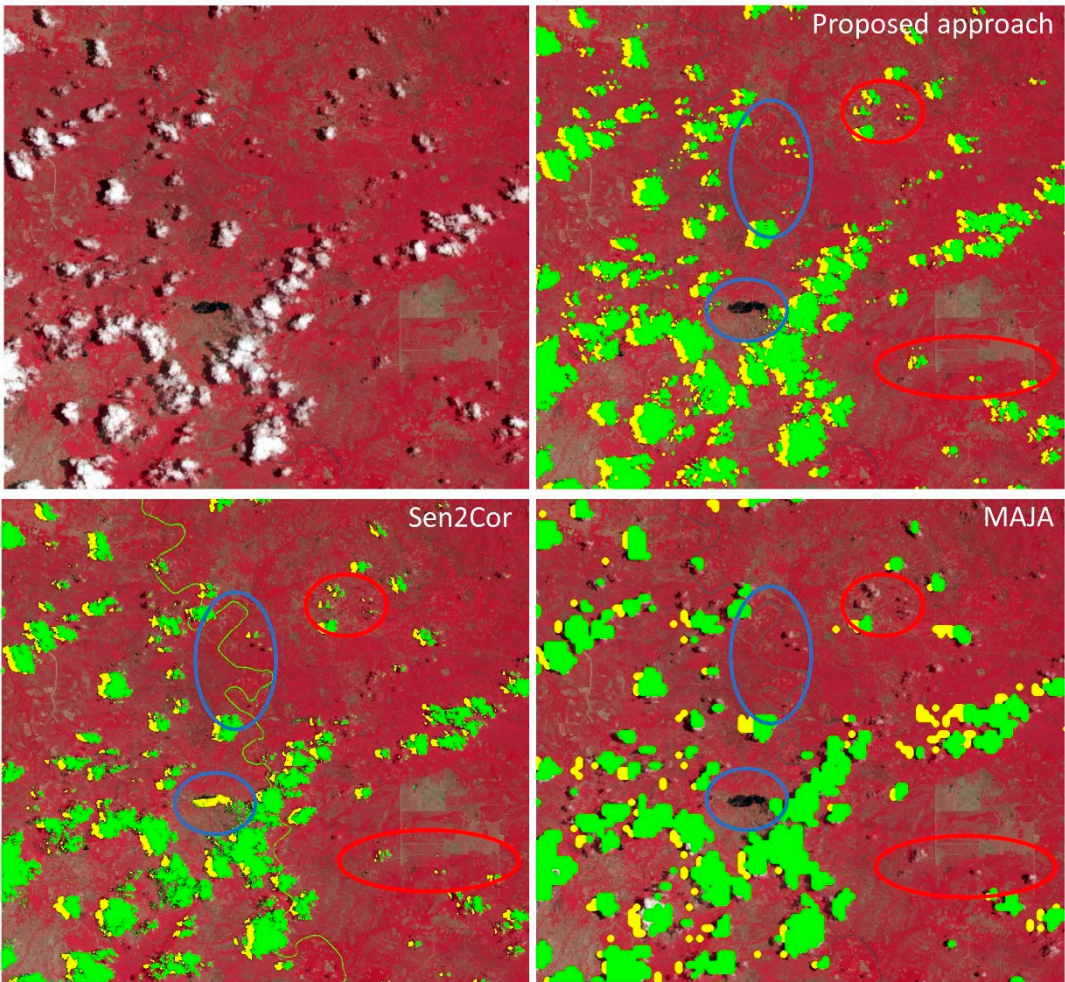
Figure 35. First test image of a Cambodia site. Zoom-in of the final 3-level cloud/cloud-shadow/others maps generated by the three algorithms under comparison, where class "others" is overlaid with the input Sentinel-2 A Multi-Spectral Instrument (MSI) Level 1C image, radiometrically calibrated into TOARF values and depicted in false-colors: monitor-typical RGB channels are selected as R = Near InfraRed (NIR) channel, G = Visible Red channel, B = Visible Green channel. Histogram stretching is applied for visualization purposes. Output class cloud is shown in a green pseudocolor, class cloud-shadow in a yellow pseudocolor. Based on qualitative photointerpetation, Sen2Cor appears to underestimate cloud-shadows, although some water areas are misclassified as cloud-shadows. In addition, some river/river beds are misclassified as clouds. These two cases of cloud false positives and cloud-shadow false positives are highlighted in blue circles. MAJA overlooks some clouds small in size (in relative terms), as highlighted in red circles.
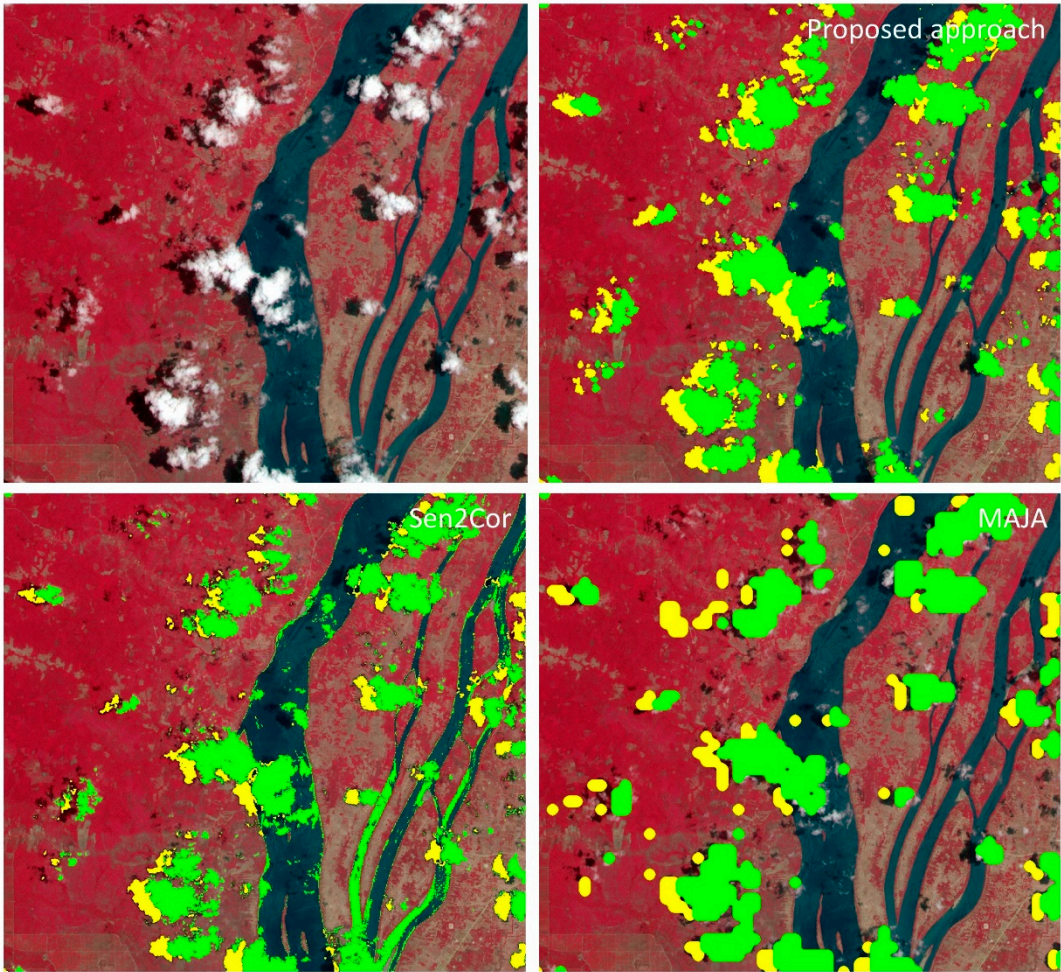
1942   **Figure 36.** First test image of a Cambodia site. Extra zoom-in of the final 3-level cloud/cloud-
1943   shadow/others maps generated by the three algorithms under comparison, where class
1944   "others" is overlaid with the input Sentinel-2 A Multi-Spectral Instrument (MSI) Level 1C
1945   image, radiometrically calibrated into TOARF values and depicted in false-colors: monitor-
1946   typical RGB channels are selected as R = Near InfraRed (NIR) channel, G = Visible Red channel,
1947   B = Visible Green channel. Histogram stretching is applied for visualization purposes. Output
1948   class cloud is shown in a green pseudocolor, class cloud-shadow in a yellow pseudocolor.
1949   Based on qualitative photointerpetation, Sen2Cor appears to underestimate cloud-shadows,
1950   although some detected cloud-shadows are false positives because of misclassified water
1951   areas. To reduce false positives in cloud-shadow detection, MAJA adopts a multi-date
1952   approach. Nevertheless, MAJA misses some instances of cloud-over-water. Overall, MAJA
1953   cloud/cloud-shadow results look more "blocky" (affected by artifacts in localizing true
1954   boundaries of target image-objects).

1955   **Table 10.** First test image of a Cambodia site. Comparison of cloud/cloud-shadow total areas
1956   detected by the three tested algorithms.

	Cloud area (ha)	Cloud-shadow (ha)
AutoCloud+	103811	49368
Sen2Cor*	82589	20296
MAJA	109373	25896

*including all cloud probability classes

1957

1958   Final cloud/cloud-shadow output maps generated from the second Sentinel-2 test image
1959   by the single-date AutoCloud+ and single-date Sen2Cor computer programs are shown in
1960   Figure 37, zoomed-in in Figure 38. Table 11 reports on the total area of clouds and cloud-
1961   shadows detected by the two algorithms of interest in the second test image.
1962
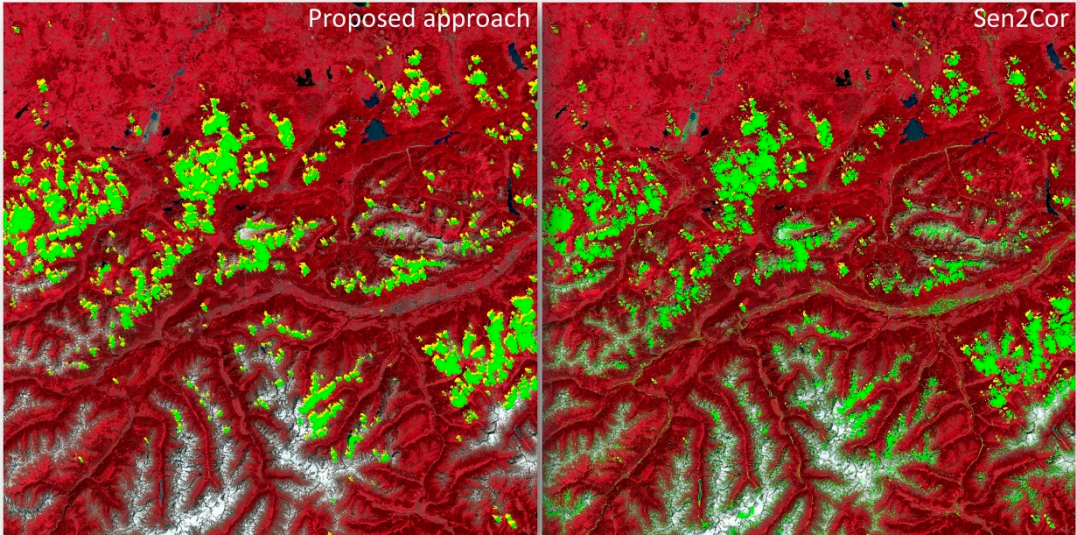
1963   **Figure 37.** Second test image of an Alpine site. Final 3-level cloud/cloud-shadow/others maps
1964   generated by the two algorithms under comparison, specifically, single-date AutoCloud+ and
1965   single-date Sen2Cor, where class "others" is overlaid with the input Sentinel-2 B Multi-
1966   Spectral Instrument (MSI) Level 1C image, radiometrically calibrated into TOARF values and
1967   depicted in false-colors: monitor-typical RGB channels are selected as R = Near InfraRed (NIR)
1968   channel, G = Visible Red channel, B = Visible Green channel. Histogram stretching is applied
1969   for visualization purposes. Output class cloud is shown in a green pseudocolor, class cloud-
1970   shadow in a yellow pseudocolor.
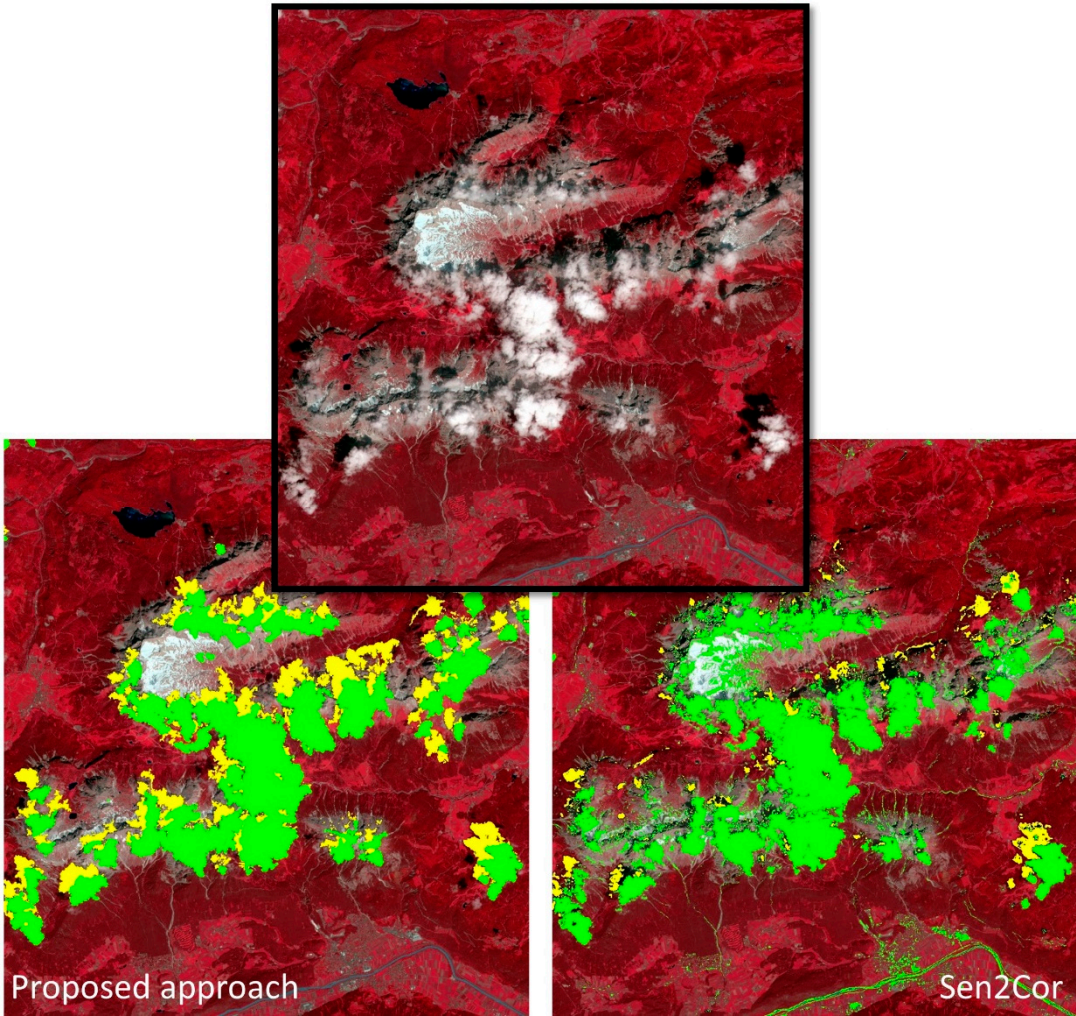
Figure 38. Second test image of an Alpine site. Zoom-in of the final 3-level cloud/cloud-shadow/others maps generated by the two algorithms under comparison, where class "others" is overlaid with the input Sentinel-2 A Multi-Spectral Instrument (MSI) Level 1C image, radiometrically calibrated into TOARF values and depicted in false-colors: monitor-typical RGB channels are selected as R = Near InfraRed (NIR) channel, G = Visible Red channel, B = Visible Green channel. Histogram stretching is applied for visualization purposes. Output class cloud is shown in a green pseudocolor, class cloud-shadow in a yellow pseudocolor. Based on qualitative photointerpetation, Sen2Cor appears to underestimate cloud-shadows, while some detected clouds are false positives because of misclassified water in river/river beds or misclassified snow/ice areas. AutoCloud+ avoids most of these cloud false positives and cloud-shadow false negatives by means of 2D spatial reasoning, specifically, by means of physical model-based modeling of cloud/cloud-shadow 2D shape properties and of bidirectional cloud/cloud-shadow 2D spatial relationships in the image-domain.

Table 11. Second test image of an Alpine site. Comparison of cloud/cloud-shadow total areas detected by the two tested algorithms.

	Cloud area (ha)	Cloud-shadow (ha)
AutoCloud+	106667	37905
Sen2Cor*	75180	14526

*including all cloud probability classes

7. Discussion

For the first Sentinel-2 test image of a Cambodia site, qualitative photointerpretation of the AutoCloud+ intermediate output products shown in Figure 33, in combination with quantitative vector quantization (VQ) error maps automatically generated as output by both the SIAM and RGBIAM software toolboxes (not shown), confirmed the validity of the SIAM and RGBIAM software solutions for color space quantization into categorical color names, in line with the existing literature [11, 12, 174], where SIAM was validated at continental scale on multi-year annual Landsat image mosaics. At first glance, qualitative photointerpretation of the output 3-level cloud/cloud-shadow/others thematic maps generated by the three AutoCloud+, Sen2Cor and MAJA algorithms under comparison, shown in Figure 34, look satisfactory. No cloud large in size (in relative terms) is missed by any algorithm. Actually, detected clouds appear somehow overestimated rather than underestimated in AutoCloud+ and MAJA. On a second glance, differences between the three approaches become notable. Table 10 reports on the total area of extracted clouds and cloud-shadows. AutoCloud+ and MAJA score similar values for the cloudy total area (~103 000 ha / 109 000 ha), but the former scores twice as much in the total amount of cloud-shadow areas (~50 000 ha). The Sen2Cor results reveal the lowest total area values (~ 82 500 ha / 20 000 ha) for both classes cloud and cloud-shadow respectively. These summary statistics are confirmed by visual analysis of zoomed-in subsets of Figure 34, as shown in Figure 35 and Figure 36. AutoCloud+ and MAJA appear to dilate (grow, on purpose) clouds at cloud boundaries to include an aura of thin cloud regions, if any, which are typically ignored by Sen2Cor. In this spatial neighboring analysis, MAJA results look more "blocky", i.e., affected by artifacts in localizing perceptually true boundaries of target image-objects, whereas the AutoCloud+ approach "naturally" follows the shape of clouds as they are perceived by a human photo interpreter. Sen2Cor largely underestimates cloud-shadows, although some water areas are misclassified as cloud-shadow, see Figure 35. In addition, some river/river beds are misclassified as clouds, see Figure 35 and Figure 36. To avoid such false positives in cloud and cloud-shadow detection affecting Sen2Cor, MAJA adopts a multi-temporal approach. Nevertheless, MAJA misses some instances of clouds small in size (in relative terms), which are detected quite well by the other two algorithms, see Figure 35. In addition, MAJA misses some instances of cloud-over-water, see Figure 36. Overall, on closer inspection of the first test case, single-date AutoCloud+ scores qualitatively "high" in cloud and cloud-shadow mapping accuracy, both affected by few false positives and few false negatives. Hence, single-date AutoCloud+ is considered superior to single-date Sen2Cor in mapping accuracy and superior to multi-date MAJA in mapping accuracy as well as ease-of-use and timeliness, since the former requires less input data to run.

For the second Sentinel-2 test image of an Alpine site, qualitative photointerpretation of the output 3-level cloud/cloud-shadow/others thematic maps generated by the two AutoCloud+ and Sen2Cor algorithms under comparison, shown in Figure 37 and zoomed-in Figure 38, confirm conclusions drawn from the first test case. Sen2Cor appears to underestimate cloud-shadows, while some detected clouds are false positives because of misclassified water in river/river beds or misclassified snow/ice areas. AutoCloud+ avoids most of these cloud false positives and cloud-shadow false negatives. Image-wide statistics collected in Table 11 confirm that AutoCloud+ tends to detect 30% to 40% more cloud-affected areas (in ha) and 50% more areas affected by cloud-shadow phenomena than Sen2Cor.

To be validated in future works at large spatial scale and multiple time samples according to the GEO-CEOS *Val* guidelines [180], these preliminary results confirm the well-groundedness of our working hypothesis (see Figure 3) in the multi-disciplinary domain of cognitive science (see Figure 5), starting from the AutoCloud+ project requirements specification summarized in Section 4 at the levels of system understanding of information/knowledge representation, system architecture, algorithm and implementation.

AutoCloud+ process quality indicators belonging to the mDMI set of EO OP-Q^{2}Is proposed in Section 2, but not investigated in this experimental session are robustness to changes in input data, at large spatial scale and time span in agreement with the GEO-CEOS

Val guidelines [180], and scalability to changes in imaging sensor's spatial and spectral resolutions. In agreement with theory (refer to Section 2 and Section 3), AutoCloud+ is expected to score "high" in all EO OP-Q²Is proposed in Section 2.

8. Conclusions

To contribute toward filling an analytic and pragmatic information gap from EO *big data,* characterized by the five Vs of volume, variety, veracity, velocity and value [4], to timely, comprehensive and operational EO data-derived value-adding products and services (VAPS), in compliance with the GEO-CEOS QA4EO Calibration/Validation (*Cal/Val*) requirements [3] and with the yet-unaccomplished visionary goal of a GEO's implementation plan for years 2005-2015 of a Global Earth Observation System of Systems (GEOSS) [5], the present research and technological development (RTD) work provides several original contributions.

Conceptual in nature and pertaining to the interdisciplinary domain of cognitive science, see Figure 5, our first original contribution coincides with our working hypothesis, see Figure 3. In symbols of the standard Unified Modeling Language (UML) for graphical modeling of object-oriented software [81], our working hypothesis reads as:

'Human vision $\rightarrow$ CV $\supset$ EO-IU in operating mode $\supset$ NASA EO Level 2 product $\rightarrow$ ESA EO Level 2 product $\rightarrow$ [EO-SCBIR + SEIKD = AI4DIAS] $\rightarrow$ GEOSS',

where symbol '$\rightarrow$' means *part-of* dependence, pointing from the supplier to the client, whereas symbol '$\supset$' means *subset-of* relationship (with inheritance), pointing from the superset to the subset. This working hypothesis postulates that necessary not sufficient pre-condition for multi-sensor EO *big data* cube analytics is systematic generation of ESA EO Level 2 product [8, 9] (for definition, refer to Section 1), encompassing cloud and cloud-shadow quality layer detection in operating mode (for definition, refer to Section 2). In greater detail, systematic ESA EO Level 2 product generation was regarded as necessary not sufficient pre-condition for developing timely, comprehensive and operational EO data-derived VAPS, such as semantic content-based image retrieval (SCBIR) + semantics-enabled information/knowledge discovery (SEIKD) = artificial intelligence (AI) for Data and Information Access Services at the ground segment (AI4DIAS), in multi-sensor, multi-temporal and multi-angular EO *big data* cubes as *part-of* the GEO-CEOS visionary goal of a GEOSS, never accomplished to date by the RS community. This dependence relationship means that the GEOSS open problem, whose *part-of* are the still-unsolved (open) subproblems of SCBIR and SEIKD, cannot be accomplished until the necessary not sufficient pre-condition of computer vision (CV) $\supset$ EO image understanding (EO-IU) in operating mode, specifically, systematic ESA EO Level 2 product generation, is accomplished in advance.

Generation of an ESA EO Level 2 product from MS imagery is a CV $\supset$ EO-IU task. Synonym of scene-from-image reconstruction and understanding [20], vision is a cognitive *(information-as-data-interpretation)* problem [15] very difficult to solve because (i) non-polynomial (NP)-hard in computational complexity [88, 89], (ii) and inherently ill-posed [20, 68], because affected by: (I) a 4D-to-2D data dimensionality reduction, from the scene-domain to the image-domain, and (II) a semantic information gap, from the sub-symbolic (quantitative, unequivocal) image-domain to the symbolic (qualitative, uequivocal) scene-domain [15, 20]. Hence, vision $\supset$ CV $\supset$ ESA EO Level 2 product generation are inherently ill-posed problems very difficult to solve, that require *a priori* knowledge in addition to sensory data to become better conditioned for numerical solution [30]. If dependence 'ESA EO Level 2 product $\rightarrow$ [EO-SCBIR + SEIKD = AI4DIAS] $\rightarrow$ GEOSS' holds, according to our working hypothesis, then the complexity of GEOSS $\geq$ complexity of [SCBIR + SEIKD] $\geq$ complexity of ESA EO Level 2 product, which is inherently ill-posed and NP-hard. This conclusion is a derived conjecture. It highlights, first, the potential relevance of ESA EO Level 2 product as information primitive for EO data-derived VAPS development in Space Economy 4.0 [59]. Second, it justifies the present work, whose overarching goal is systematic ESA EO Level 2

product generation, starting from cloud and cloud-shadow quality layer detection in operating mode.

Our second original contribution is both conceptual and pragmatic in the codification of RS best practice, which is the focus of efforts made by, for example, intergovernmental organizations such as GEO and CEOS. ESA EO Level 2 product is regarded as baseline information primitive suitable for an "augmented" EO Analysis Ready Data (ARD) format specification, more restrictive (in terms of output product requirements specification) and more informative (in terms of physical and conceptual/semantic quality of numeric and categorical output products, respcetively), but more difficult to be inferred from EO sensory data than the U.S. Landsat ARD [120, 121] and CEOS ARD for Land (CARD4L) formats [119].

To contribute toward filling an analytic and pragmatic information gap from EO *big data* to timely, comprehensive and operational EO data-derived VAPS, starting from the necessary not sufficient pre-condition of systematic ESA EO Level 2 product generation, our third original contribution deals with the RTD and the preliminary quality assessment of AutoCloud+, a "universal" software toolbox for cloud and cloud-shadow quality layer detection in multi-sensor multi-angular EO single-date MS imagery, either uncalibrated or radiometrically calibrated into TOARF, SURF or surface albedo values.

Noteworthy, jointly detection of cloud and cloud-shadow is a typical example of physical model-based cause-effect relationship, expected to be very difficult to solve by inductive machine learning-from-data algorithms, such as increasingly popular DCNNs [31], suitable for learning complex correlations between input and output features, but capable of no inherent representation of causality ([57]; [27]), in agreement with the well-known dictum that correlation does not imply causation and vice versa ([10]; [30]; [57]; [27]; [58]; [16]).

In comparison with standard cloud/cloud-shadow software toolboxes available either open source or free of cost, such as FMask, Sen2Cor and MAJA, AutoCloud+ features several degrees of novelty at the Marr's four levels of system understanding, specifically, information/knowledge representation, system architecture, algorithm and implementation. For example, at the levels of abstraction of information/knowledge representation and system architecture, typically considered the linchpin of success of an information processing system, AutoCloud+ is the sole hybrid (combined physical and statistical model-based) 2D image analysis (spatial context-sensitive and spatial topology-preserving) approach provided with feedback loops, in agreement with biological cognitive systems [71, 77, 89].

In a proof-of-concept conducted by qualitative photointerpretation of two Sentinel-2 test images, AutoCloud+ outperformed the standard single-date Sentinel-2 sensor-specific Sen2Cor and the multi-date MAJA computer program in terms of cloud and cloud-shadow mapping quality indicators, such as true positive, false positive, true negative and false negative occurrences.

With regard to an mDMI set of EO OP-Q^{2}Is proposed in Section 2, potential advantages of the proposed hybrid feedback 2D image analysis approach for cloud and cloud-shadow detection are summarized below.

(1) The AutoCloud+ computer program is "fully automated".

    i.   It requires no system's free-parameter to be user-defined based on heuristics, unlike mainstream CV and EO-IU algorithms, such as inductive DCNNs, where *a priori* knowledge is encoded by design based on empirical criteria, a.k.a. trial-and error. Hence, its ease of use cannot be surpassed by alternative algorithms.

    ii.   It requires no supervised data set for inductive learning-from-data. Hence, its costs in manpower for collecting training data samples are zero and its timeliness from data collection to output product generation is reduced to computation time.

(2) It employs a known hybrid feedback CV system design (architecture, see Figure 21) whose processing units have been to a large degree implemented in operating mode and tested/validated in previous works, e.g., refer to the SIAM and RGBIAM lightweight computer programs for color space partitioning into color names, superpixel detection and

2141   VQ quality assessment ([10]; [11], [12]; [174]). Hence, its RTD costs in manpower are greatly
2142   reduced.

2143   (3)   In line with biological vision, the AutoCloud+ CV subsystem exploits dominant spatial
2144   topological and spatial non-topological information components in combination with
2145   secondary color information, discretized into color names, according to a convergence-of-
2146   evidence approach consistent with symbolic human reasoning, where potentially weak
2147   independent sources of evidence are typically combined to infer strong conjectures. For
2148   example, in two Sentinel-2 test images selected for proof-of-concept, the single-date
2149   AutoCloud+ computer program scored better than standard software toolboxes, such as
2150   the single-date Sen2Cor and the multi-date MAJA, in both cloud and cloud-shadow
2151   detection in terms of true positive, false positive, true negative and false negative
2152   estimates. In addition to showing a superior mapping accuracy, based on theory
2153   AutoCloud+ is expected to score also "high" in robustness to changes in input data and in
2154   scalability to changes in MS imaging sensor's specifications.

2155   To underpin the operational readiness of the AutoCloud+ software toolbox in support of
2156   systematic ESA EO Level 2 product generation, a complete AutoCloud+ software
2157   transcodification into the C programming language is planned for efficiency reasons, together
2158   with GEO-CEOS stage 3 and stage 4 *Val* campaigns to be conducted by independent means at
2159   large spatial extent and time span with multiple MS imaging sensors, in compliance with the
2160   GEO-CEOS *Val* guidelines [180] and the GEO-CEOS QA4EO *Cal/Val* requirements [3].

2161   **Author Contributions:** Conceptualization, A.B. and D.T.; Methodology, A.B. and D.T.; Software, A.B.
2162   and D.T.; Validation, D.T.; Formal Analysis, A.B. and D.T.; Investigation, A.B. and D.T.; Resources, A.B.
2163   and D.T.; Data Curation, D.T.; Writing-Original Draft Preparation, A.B.; Writing-Review & Editing, A.B.
2164   and D.T.; Visualization, A.B. and D.T.; Supervision, D.T.; Project Administration, D.T.; Funding
2165   Acquisition, D.T.

2166   **Funding:** This research was funded in part by the Austrian Science Fund (FWF) through the Doctoral
2167   College GIScience (DK W1237- N23) and by the Austrian Research Promotion Agency (FFG) with regard
2168   to project Sentinel-2 Semantic Data Cube (Sen2cube).

2169   **Acknowledgments:** Andrea Baraldi thanks Prof. Raphael Capurro for his hospitality, patience, politeness
2170   and open-mindedness. The authors wish to thank the Editor-in-Chief, Associate Editor and reviewers
2171   for their competence, patience and willingness to help.

2172   **Conflicts of Interest:** The authors declare no conflict of interest. The funders had no role in the design of
2173   the study; in the collection, analyses, or interpretation of data; in the writing of the manuscript, and in
2174   the decision to publish the results.

2175   **References**

2176   1.   [1] G. Schaepman-Strub, M. E. Schaepman, T. H. Painter, S. Dangel, and J. V. Martonchik,
2177   "Reflectance quantities in optical remote sensing - Definitions and case studies," Remote Sens.
2178   Environ., vol. 103, pp. 27–42, 2006.
2179   2.   [2] Liang, S. 2004. Quantitative Remote Sensing of Land Surfaces. Hoboken, NJ, USA: John Wiley
2180   and Sons.
2181   3.   [3] Group on Earth Observation / Committee on Earth Observation Satellites (GEO-CEOS). (2010).
2182   A Quality Assurance Framework for Earth Observation, version 4.0.
2183   http://qa4eo.org/docs/QA4EO_Principles_v4.0.pdf
2184   4.   [4] Yang, C., Huang, Q., Li, Z., Liu K. & Hu, F., (2017). Big Data and cloud computing: innovation
2185   opportunities and challenges, International Journal of Digital Earth. 10:1, p.13-53, DOI:
2186   10.1080/17538947.2016.1239771
2187   5.   [5] Group on Earth Observation (GEO). (2005). The Global Earth Observation System of Systems
2188   (GEOSS) 10-Year Implementation Plan. Available online:
2189   http://www.earthobservations.org/docs/10-Year%20Implementation%20Plan.pdf (accessed on 19
2190   January 2012).

2191   6.   [6] Blaschke, T. and Lang, S. (2006). Object based image analysis for automated information
2192   extraction-a synthesis. Measuring the Earth II ASPRS Fall Conference, 6-10.
2193   7.   [7] Blaschke, T., G. J. Hay, M. Kelly, S. Lang, P. Hofmann, E. Addink, R. Queiroz Feitosa, F. van der
2194   Meer, H. van der Werff, F. van Coillie, and D. Tiede. 2014. "Geographic object-based image analysis
2195   - towards a new paradigm." ISPRS J. Photogram. Remote Sens. 87: 180–191.
2196   8.   [8] European Space Agency (ESA). 2015. Sentinel-2 User Handbook, , Standard Document, Issue 1
2197   Rev 2.
2198   9.   [9] Deutsches Zentrum für Luft- und Raumfahrt e.V. (DLR) and VEGA Technologies. 2011. Sentinel-
2199   2 MSI – Level 2A Products Algorithm Theoretical Basis Document. Document S2PAD-ATBD-0001,
2200   European Space Agency.
2201   10.   [10] Baraldi, A. 2017. "Pre-processing, classification and semantic querying of large-scale Earth
2202   observation spaceborne/airborne/terrestrial image databases: Process and product innovations".
2203   Ph.D. dissertation in Agricultural and Food Sciences, University of Naples "Federico II",
2204   Department of Agricultural Sciences, Italy. Ph.D. defense: 16 May 2017. DOI:
2205   10.13140/RG.2.2.25510.52808. Accessed 30 Jan. 2018.
2206   https://www.researchgate.net/publication/317333100_Pre-
2207   processing_classification_and_semantic_querying_of_large-
2208   scale_Earth_observation_spaceborneairborneterrestrial_image_databases_Process_and_product_i
2209   nnovations
2210   11.   [11] Baraldi, A., Humber, M. L., Tiede, D., & Lang, S. (2018a). GEO-CEOS stage 4 validation of the
2211   Satellite Image Automatic Mapper lightweight computer program for ESA Earth observation Level
2212   2 product generation – Part 1: Theory. Cogent Geoscience, Accepted manuscript, 1467357.
2213   https://doi.org/10.1080/23312041.2018.1467357
2214   12.   [12] Baraldi, A., Humber, M. L., Tiede, D., & Lang, S. (2018b). GEO-CEOS stage 4 validation of the
2215   Satellite Image Automatic Mapper lightweight computer program for ESA Earth observation Level
2216   2 product generation – Part 2: Validation. Cogent Geoscience, Accepted manuscript, 1467254.
2217   https://doi.org/10.1080/23312041.2018.1467254
2218   13.   [13] Di Gregorio, A., and L. Jansen. 2000. Land Cover Classification System (LCCS): Classification
2219   Concepts and User Manual. FAO: Rome, Italy, FAO Corporate Document Repository. Accessed 10
2220   February 2015. http://www.fao.org/DOCREP/003/X0596E/X0596e00.htm
2221   14.   [14] Swain, P. H., & Davis, S.M. (1978). Remote Sensing: The Quantitative Approach. New York:
2222   McGraw-Hill.
2223   15.   15] Capurro, R. & Hjørland, B. (2003). The concept of information. Annual Review of Information
2224   Science and Technology, 37, 343-411.
2225   16.   [16] Sonka, M., Hlavac, V., & Boyle, R. (1994). Image Processing, Analysis and Machine Vision.
2226   London, U.K.: Chapman & Hall.
2227   17.   [17] Fonseca, F., Egenhofer, M., Agouris, P. & Camara, G. (2002). Using ontologies for integrated
2228   geographic information systems, *Trans. in GIS*, 6, 231–257.
2229   18.   [18] Growe, S. (1999). Knowledge-based interpretation of multisensor and multitemporal remote
2230   sensing images. *Int. Archives of Photogrammetry and Remote Sensing*, 32, Part 7–4–3 W6, Valladolid,
2231   Spain, 3–4 June, 1999.
2232   19.   [19] Laurini, R. & Thompson, D. (1992*). Fundamentals of Spatial Information Systems*. London, UK:
2233   Academic Press.
2234   20.   [20] Matsuyama, T., and V. S. Hwang. (1990). SIGMA – A Knowledge-based Aerial Image
2235   Understanding System. New York, NY: Plenum Press.
2236   21.   [21] Sowa, J. (2000). Knowledge representation: Logical, philosophical, and computational
2237   foundations, Brooks Cole Publishing Co., Pacific Grove (CA).
2238   22.   [22] Ahlqvist, O. 2005. "Using uncertain conceptual spaces to translate between land cover
2239   categories." *Int. J. Geographic. Info. Science* 19: 831–857.
2240   23.   [23] Bossard, M., J. Feranec and J. Otahel. 2000. "CORINE land cover technical guide – Addendum
2241   2000, Technical report No 40." European Environment Agency.
2242   24.   [24] Lillesand, T., & Kiefer, R. (1979). *Remote Sensing and Image Interpretation*, New York: John Wiley
2243   & Sons.

25. [25] Belward, A., Ed. 1996. The IGBP-DIS Global 1Km Land Cover Data Set "DISCover": Proposal and Implementation Plans. IGBP-DIS Working Paper 13. International Geosphere Biosphere Programme. European Commission Joint Research Center, Ispra, Varese, Italy.

26. [26] Dumitru C. O., S. Cui, G. Schwarz, and M. Datcu. 2015. "Information content of very-high-resolution SAR images: Semantics, geospatial context, and ontologies." IEEE J. Selected Topics Applied Earth Obs. Remote Sens. 8(4): 1635 – 1650.

27. [27] Marcus, G. 2018. "Deep Learning: A Critical Appraisal." arXiv: 1801.00631. Accessed: 16 Jan. 2018. https://arxiv.org/ftp/arxiv/papers/1801/1801.00631.pdf

28. [28] Gutman, G., A. C. Janetos, C. O. Justice, E. F. Moran, J. F. Mustard, R. R. Rindfuss, D. Skole, B. L. Turner, M. A. Cochrane, Eds. 2004. *Land Change Science*. Dordrecht, The Netherlands: Kluwer.

29. [29] Bishop, C. M. 1995. Neural Networks for Pattern Recognition. Oxford, U.K.: Clarendon.

30. [30] Cherkassky, V., and F. Mulier. 1998. Learning from Data: Concepts, Theory, and Methods. New York, NY: Wiley.

31. [31] Cimpoi M., S. Maji, I. Kokkinos I., and A. Vedaldi. 2014. "Deep filter banks for texture recognition, description, and segmentation," CoRR, abs/1411.6836.

32. [32] Lipson, H. 2007. "Principles of modularity, regularity, and hierarchy for scalable systems," Journal of Biological Physics and Chemistry, 7, 125–128.

33. [33] Wolpert, D. H. (1996). The lack of a priori distinctions between learning algorithms. Neural Computation, 8(7), 1341–1390.

34. [34] Wolpert, D. H., & Macready, W. G. (1997). No free lunch theorems for optimization. IEEE Trans on Evolutionary Computation, 1(1), 67–82.

35. [35] Zhaoxiang, Z.; Iwasaki, A.; Guodong, X.; Jianing, S. Small Satellite Cloud Detection Based On Deep Learning and Image Compression. Preprints 2018, 2018020103 (doi: 10.20944/preprints201802.0103.v1. Available online: https://www.preprints.org/manuscript/201802.0103/v1 (accessed on 7 Aug. 2018).

36. [36] Baraldi, A. (2015). "Automatic Spatial Context-Sensitive Cloud/Cloud-Shadow Detection in Multi-Source Multi-Spectral Earth Observation Images – AutoCloud+," Invitation to tender ESA/AO/1-8373/15/I-NB – "VAE: Next Generation EObased Information Services", DOI: 10.13140/RG.2.2.34162.71363. arXiv: 1701.04256. Date: 8 Jan. 2017. Available online: https://arxiv.org/ftp/arxiv/papers/1701/1701.04256.pdf

37. [37] Gascon, F., Bouzinac, C., Thépaut, O., Jung, M., Francesconi, B., Louis, J., Lonjou, V., Lafrance, B., Massera, S., Gaudel-Vacaresse, A., Languille, F., Alhammoud, B., Viallefont, F., Pflug, B., Bieniarz, J., Clerc, S., Pessiot, L., Trémas, T., Cadau, E., De Bonis, R., Isola, C., Martimort, P., Fernandez, V., (2017). Copernicus Sentinel-2A Calibration and Products Validation Status. Remote Sens. Vol. 9, no. 6, 584. doi:10.3390/rs9060584

38. [38] Goodwin, N.R., Collett, L.J., Denham, R.J., Flood, N., Tindall, D., (2013). Cloud and cloud-shadow screening across Queensland, Australia: An automated method for Landsat TM/ETM+ time series. Remote Sensing of Environment, 134, p.50–65. http://dx.doi.org/10.1016/j.rse.2013.02.019.

39. [39] Hagolle, O., Huc, M., Desjardins, C., Auer, S., Richter, R., (2017a). *MAJA Algorithm Theoretical Basis Document*, Available at: https://zenodo.org/record/1209633#.W2ffFNIzZaQ.

40. [40] Olivier Hagolle, Bastien Rouquié, Camille Desjardins, Aliaksei Makarau, Magdalena Main-knorn, Guillaume Rochais, Bringfried Pug, 2017b. Recent advances in cloud detection and atmospheric correction applied to time series of high resolution images, RAQRS, 19 Sept 2017. Available online: https://www.researchgate.net/profile/Olivier_Hagolle2/publication/320402521_Recent_advances_in_cloud_detection_and_atmospheric_correction_applied_to_time_series_of_high_resolution_images/links/59eeee074585154350e83669/Recent-advances-in-cloud-detection-and-atmospheric-correction-applied-to-time-series-of-high-resolution-images.pdf (accessed on 8 Aug. 2018)

41. [41] Hagolle, O., Huc, M., Pascual, D.V., Dedieu, G., (2010). A multi-temporal method for cloud detection, applied to FORMOSAT-2, VENμS, LANDSAT and SENTINEL-2 images. Remote Sensing of Environment, 114(8), p.1747–1755. doi:10.1016/j.rse.2010.03.002

42. [42] Hollstein, A., Segl, K., Guanter, L., Brell, M., Enesco, M., (2016). Ready-to-use methods for the detection of clouds, cirrus, snow, shadow, water and clear sky pixels in Sentinel-2 MSI images. Remote Sensing. 8, p. 1–18. doi:10.3390/rs8080666

43. [43] C. Huang, N. Thomas, S. N. Goward, J. G. Masek, Z. Zhu, J. R. G. Townshend, and J. E. Vogelmann, "Automated masking of cloud and cloud shadow for forest change analysis using Landsat images," International Journal of Remote Sensing, vol. 31, no. 20, pp. 5449-5464, 2010.

44. [44] Hughes M.J. & Hayes, D.J. (2014). Automated detection of cloud and cloud shadow in single-date Landsat imagery using neural networks and spatial post-processing. Remote Sensing, 6(6), 4907–4926. doi:10.3390/rs6064907

45. [45] R. R. Irish, J. L. Barker, S. N. Goward, and T. Arvidson, "Characterization of the Landsat-7 ETM+ Automated Cloud-Cover Assessment (ACCA) Algorithm," Photogrammetric Engineering & Remote Sensing, vol. 72, no. 10, pp. 1179–1188, October 2006.

46. [46] Ju, J.; Roy, D.P. The availability of cloud-free Landsat ETM+ data over the conterminous United States and globally. Remote Sens. Environ. 2008, 112, 1196–1211.

47. [47] K. V. Khlopenkov and A.P. Trishchenko, "SPARC: New cloud, snow, and cloud shadow detection scheme for historical 1-km AVHRR data over Canada," Journal of Atmospheric and Oceanic Technology, vol. 24, pp. 322–343, 2007.

48. [48] S. Le Hégarat-Mascle and C. André, "Reduced false alarm automatic detection of clouds and shadows on SPOT images using simultaneous estimation," Proc. SPIE, 6748-46, vol. 1, p. 1-12, 2010.

49. [49] Lück W., and A. van Niekerk. 2016. "Evaluation of a rule-based compositing technique for Landsat-5 TM and Landsat-7 ETM+ images," Int. J. of Applied Earth Observation and Geoinformation 47: 1–14.

50. [50] Luo, Y., Trishchenko, A.P. & Khlopenkov, K. V., (2008). Developing clear-sky, cloud and cloud-shadow mask for producing clear-sky composites at 250-meter spatial resolution for the seven MODIS land bands over Canada and North America. Remote Sensing of Environment, 112(12), p.4167–4185. http://dx.doi.org/10.1016/j.rse.2008.06.010.

51. [51] Zhu, Z. & Woodcock, C.E., (2012). Object-based cloud and cloud-shadow detection in Landsat imagery. Remote Sensing of Environment, 118, p.83–94.

52. [52] Zhu, Z., Wang, S. & Woodcock, C.E., (2015). Improvement and expansion of the Fmask algorithm : cloud , cloud-shadow , and snow detection for Landsats 4 – 7 , 8 , and Sentinel 2 images. Remote Sensing of Environment, 159, p.269–277. http://dx.doi.org/10.1016/j.rse.2014.12.014

53. [53] Zhe Zhu and Woodcock, C. E. 2014. Automated cloud, cloud shadow, and snow detection in multitemporal Landsat data: An algorithm designed specifically for monitoring land cover change. Remote Sens. Environ., vol. 152, pp. 217–234, 2014.

54. [54] Main-Knorn, M., Louis, J., Hagolle, O., Müller-Wilm, U., and Alonso, K., The Sen2Cor and MAJA cloud masks and classification products, 2nd Sentinel-2 Validation Team Meeting, 29-31 Jan. 2018, ESA-ESRIN, Frascati (Rome), Italy.

55. [55] Foga, S., P. Scaramuzza, S. Guo, Z. Zhu, R.Dilley Jr, T. Beckmann, G. Schmidt, J. Dwyer, M. Hughes, and B. Laue. 2017. "Cloud detection algorithm comparison and validation for operational Landsat data products." Remote Sens. Environ. 194: 379–390.

56. [56] U.S. Geological Survey (USGS), 2018d. U.S. Landsat Analysis Ready Data (ARD) Artifacts. Available online: https://landsat.usgs.gov/us-landsat-ard-artifacts (accessed on 15 July 2018).

57. [57] Chomba Bupe, Is Deep Learning fundamentally flawed and hitting a wall? Was Gary Marcus correct in pointing out Deep Learning's flaws?, Quora, 2018. Available online: https://www.quora.com/Is-Deep-Learning-fundamentally-flawed-and-hitting-a-wall-Was-Gary-Marcus-correct-in-pointing-out-Deep-Learnings-flaws. Accessed 7 Aug. 2018.

58. [58] Pearl, J. 2009. Causality: Models, Reasoning and Inference. New York (NY): Cambridge University Press.

59. [59] Mazzuccato M. and D. Robinson. (2017). Market Creation and the European Space Agency. European Space Agency (ESA) Report. Available at: https://marianamazzucato.com/wp-content/uploads/2016/11/Mazzucato_Robinson_Market_creation_and_ESA.pdf

60. [60] A. Baraldi, "Impact of radiometric calibration and specifications of spaceborne optical imaging sensors on the development of operational automatic remote sensing image understanding systems," IEEE J. Sel. Topics Appl. Earth Observ. Remote Sens., vol. 2, no. 2, pp. 104-134, June 2009.

61. [61] Pacifici, F. Atmospheric Compensation in Satellite Imagery. US Patent 9396528B2, 19 July 2016.

62. [62] F. Pacifici, N. Longbotham, and W. J. Emery, "The Importance of Physical Quantities for the Analysis of Multitemporal and Multiangular Optical Very High Spatial Resolution Images," IEEE Trans. Geosci. Remote Sens., 2014.

63. [63] Richter, R., & Schläpfer, D. (2012a). Atmospheric / Topographic Correction for Satellite Imagery – ATCOR-2/3 User Guide, Version 8.2 BETA. Available online: http://www.dlr.de/eoc/Portaldata/60/Resources/dokumente/5_tech_mod/atcor3_manual_2012.pdf. Accessed 12 April 2013.

64. [64] Richter, R., & Schläpfer, D. (2012b). Atmospheric / Topographic correction for airborne imagery – ATCOR-4 User Guide, Version 6.2 BETA. Available online: http://www.dlr.de/eoc/Portaldata/60/Resources/dokumente/5_tech_mod/atcor4_manual_2012.pdf. Accessed 12 April 2013.

65. [65] Dorigo, W., Richter, R., Baret, F., Bamler, R., & Wagner, W. (2009). Enhanced automated canopy characterization from hyperspectral data by a novel two step radiative transfer model inversion approach. Remote Sens., 1, 1139-1170.

66. [66] Schläpfer, D., Richter, R., & Hueni, A. (2009). Recent developments in operational atmospheric and radiometric correction of hyperspectral imagery, in Proc. 6th EARSeL SIG IS Workshop, 16-19 March 2009. Retrieved July, 14, 2012 from http://www.earsel6th.tau.ac.il/~earsel6/CD/PDF/earsel-PROCEEDINGS/3054%20Schl%20pfer.pdf

67. [67] Andrea Baraldi and Dirk Tiede, "AutoCloud+, a "universal" single-date multi-sensor physical and statistical model-based spatial context-sensitive cloud/cloud-shadow detector in multi-spectral Earth observation imagery," GEOBIA 2018, Montpellier, France, June 18-22, 2018.

68. [68] M. Bertero, T. Poggio, and V. Torre, "Ill-posed problems in early vision," Proc. of the IEEE, vol. 76, no. 8, pp. 869–889, Aug. 1988.

69. [69] Marr, D. (1982). Vision. New York, NY: Freeman and C.

70. [70] Serra, R. and Zanarini, G. (1990). Complex Systems and Cognitive Processes, Berlin: Springer-Verlag.

71. [71] D. Parisi, "La scienza cognitiva tra intelligenza artificiale e vita artificiale," in Neurosceinze e Scienze dell'Artificiale: Dal Neurone all'Intelligenza, Bologna, Italy: Patron Editore, 1991.

72. [72] G. A. Miller, "The cognitive revolution: a historical perspective", in Trends in Cognitive Sciences, vol. 7, pp. 141-144, 2003.

73. [73] F. J. Varela, E. Thompson, and E. Rosch, The Embodied Mind: Cognitive Science and Human Experience. Cambridge, MA: MIT Press, 1991.

74. [74] F. Capra and P. L. Luisi, The Systems View of Life: A Unifying Vision. Cambridge, UK: Cambridge University Press, 2014.

75. [75] Castelletti, D., Pasolli, L,. Bruzzone, L., Notarnicola, C., & Demir, B. (2016). A novel hybrid method for the correction of the theoretical model inversion in bio/geophysical parameter estimation. *IEEE Trans. Geosci. Remote Sens.*, XX(Y), 1–11.

76. [76] Baraldi, A., Gironda, M., & Simonetti, D. (2010c). Operational two-stage stratified topographic correction of spaceborne multi-spectral imagery employing an automatic spectral rule-based decision-tree preliminary classifier. IEEE Trans. Geosci. Remote Sensing, 48(1), 112-146.

77. [77] J. Piaget, Genetic Epistemology, New York: Columbia University Press, 1970.

78. [78] A. Baraldi and L. Boschetti, "Operational automatic remote sensing image understanding systems: Beyond Geographic Object-Based and Object-Oriented Image Analysis (GEOBIA/GEOOIA) - Part 1: Introduction," Remote Sens., vol. 4, no. 9, pp. 2694-2735, 2012.

79. [79] A. Baraldi and L. Boschetti, "Operational automatic remote sensing image understanding systems: Beyond Geographic Object-Based and Object-Oriented Image Analysis (GEOBIA/GEOOIA) - Part 2: Novel system architecture, information/knowledge representation, algorithm design and implementation," Remote Sens., vol. 4, no. 9, pp. 2768-2817, 2012.

80. [80] National Aeronautics and Space Administration (NASA). (2016). Data Processing Levels. [Online]. Available: https://science.nasa.gov/earth-science/earth-science-data/data-processing-levels-for-eosdis-data-products. Accessed on December 20, 2016.

81. [81] Fowler, M. (2003). UML Distilled Third Edition. Boston, MS, USA: Addison-Wesley.

82. [82] A. Baraldi, D. Tiede, M. Sudmanns, M. Belgiu, and S. Lang, "Automated near real-time Earth observation Level 2 product generation for semantic querying," GEOBIA 2016, 14-16 Sept. 2016,

University of Twente Faculty of Geo-Information and Earth Observation (ITC), Enschede, The Netherlands.

83. [83] A. Baraldi, D. Tiede, M. Sudmanns, and S. Lang, 2017a. "Systematic ESA EO Level 2 product generation as pre-condition to semantic content-based image retrieval and information/knowledge discovery in EO image databases," 2017 Conf. on Big Data From Space, BiDS'17, Toulouse, France, 28-30 March, 2017.

84. [84] D. Tiede, A. Baraldi, M Sudmanns, M. Belgiu and S. Lang, "Architecture and prototypical implementation of a semantic querying system for big earth observation image bases," European Journal of Remote Sensing, vol. 50, no. 1, pp. 452-463, Aug. 2017. DOI: 10.1080/22797254.2017.1357432

85. [85] Augustin, H., Sudmanns, M., Tiede, D., and Baraldi, A., 2018. A semantic Earth observation data cube for monitoring environmental changes during the Syrian conflict. AGIT 2018, Salzburg, Austria, July 3-6, 2018, GI_Forum Journal, vol. 1, pp. 214–227. doi:10.1553/giscience2018_01_s214

86. [86] M. Sudmanns, D. Tiede, S. Lang and A. Baraldi, "Semantic and syntactic interoperability in online processing of big Earth observation data", Int. J. of Digital Earth, vol. 11, no. 1, pp. 95-112, 2018. DOI: 10.1080/17538947.2017.1332112.

87. [87] Smeulders, A., Worring, M., Santini, S., Gupta, A., & Jain, R. (2000). Content-based image retrieval at the end of the early years. *IEEE Trans. Pattern Anal. Machine Intell.*, 22(12), 1349-1380.

88. [88] Frintrop, S. (2011). Computational visual attention. In *Computer Analysis of Human Behavior, Advances in Pattern Recognition*, A. A. Salah and T. Gevers, Eds,. Springer .

89. [89] Tsotsos, J. K. (1990). Analyzing vision at the complexity level. *Behavioral and Brain Sciences*, 13, 423-469.

90. [90] Hadamard, J. 1902. "Sur les problemes aux derivees partielles et leur signification physique," Princet. Univ. Bull. 13: 49–52.

91. [91] Baraldi, A., L. Boschetti, and M. Humber. 2014. "Probability sampling protocol for thematic and spatial quality assessments of classification maps generated from spaceborne/airborne very high resolution images." IEEE Trans. Geosci. Remote Sens. 52(1): 701-760.

92. [92] J. D. Shepherd and J. R. Dymond, "BRDF correction of vegetation in AVHRR imagery," Remote Sens. Environ., vol. 74, no. 3, pp. 397–408, Dec. 2000.

93. [93] T. Danaher, "An empirical BRDF correction for landsat TM and ETM+ imagery," in Proc. 11th Aust. Remote Sens. Photogramm. Conf., Brisbane, Australia, 2002, pp. 2654–2657.

94. [94] A. Wu, Z. Li, and J. Cihlar, "Effects of land cover type and greenness on advanced very high resolution radiometer bidirectional reflectances: Analysis and removal," J. Geophys. Res., vol. 100, no. D5, pp. 9179–9192, Jan 1995.

95. [95] Ghahramani, Z. (2011). Bayesian nonparametrics and the probabilistic approach to modelling. *Phil. Trans. R. Soc. A*, 1–27.

96. [96] Wikipedia (2017). Bayesian inference. [Online]. Available: https://en.wikipedia.org/wiki/Bayesian_inference. Accessed 14 March 2017.

97. [97] DiCarlo, J. (2017). The Science of Natural intelligence: Reverse engineering primate visual perception. Keynote, CVPR17 Conference. Date 5 Jan. 2018. Available online: https://www.youtube.com/watch?v=ilbbVkIhMgo

98. [98] du Buf ,H., & Rodrigues, J. (2007). Image morphology: from perception to rendering. In *IMAGE - Computational Visualistics and Picture Morphology*.

99. [99] Kosslyn, S. M. (1994). *Image and Brain*. Cambridge, MA: MIT Press.

100. [100] Serre, T., Wolf, L., Bileschi, S., Riesenhuber, M., & Poggio, T. (2007). Robust object recognition with cortex-like mechanisms, *IEEE Trans. Pattern Anal. Machine Intell.*, 29(3), 411–426.

101. [101] Sylvester, J., & Reggia, J. (2016). Engineering neural systems for high-level problem solving. Neural Networks, 79, 37–52.

102. [102] Vecera, S., & Farah, M. (1997). Is visual image segmentation a bottom-up or an interactive process?. *Percept. Psychophys.*, 59, 1280–1296.

103. [103] P. Quinlan, "Marr's Vision 30 years on: From a personal point of view", Perception, vol. 41, pp. 1009 – 1012, 2012.

104. [104] Duke University, (2016). Measurement: Process and Outcome Indicators, Duke Center for Instructional Technology. [Online] Available: http://patientsafetyed.duhs.duke.edu/module_a/measurement/measurement.html

105. [105] Boschetti, L., S. P. Flasse, and P. A. Brivio. 2004. "Analysis of the conflict between omission and commission in low spatial resolution dichotomic thematic products: The Pareto boundary." Remote Sens. Environ. 91: 280–292.

106. [106] Couclelis, H. (2012). What GIScience is NOT: Three theses. Invited speaker, GIScience '12 Int. Conf., Columbus, Ohio, Sept. 18-21, 2012.

107. [107] Etzioni, O. (2017). What shortcomings do you see with deep learning?. Quora. Date: 8 Jan. 2018. Available online: https://www.quora.com/What-shortcomings-do-you-see-with-deep-learning

108. [108] C. Shannon, "A mathematical theory of communication," Bell System Technical Journal, vol. 27, pp. 379–423 and 623–656, 1948.

109. [109] Tobler, W.R., 1970, A computer movie simulating urban growth in the Detroit Region. Economic Geography, 46, pp. 234–240.

110. [110] P. A. Longley, M. F. Goodchild, D. J. Maguire D. W. Rhind, Geographic Information Systems and Science, Second Edition. New York: Wiley, 2005.

111. [111] Andrea Baraldi, Stefan Lang, Dirk Tiede, and Thomas Blaschke, 2018c. "Earth observation big data analytics in operating mode for GIScience applications – The (GE)OBIA acronym(s) reconsidered," GEOBIA 2018, Montpellier, France, June 18-22, 2018.

112. [112] Stefan Lang, Andrea Baraldi, Dirk Tiede, Geoffrey Hay and Thomas Blaschke, "Towards a (GE)OBIA 2.0 manifesto – Achievements and open challenges in information & knowledge extraction from big Earth data," GEOBIA 2018, Montpellier, France, June 18-22, 2018.

113. [113] Baraldi, A., Durieux, L., Simonetti, D., Conchedda, G., Holecz, F., & Blonda, P. (2010a). Automatic spectral rule-based preliminary classification of radiometrically calibrated SPOT-4/-5/IRS, AVHRR/MSG, AATSR, IKONOS/QuickBird/OrbView/GeoEye and DMC/SPOT-1/-2 imagery – Part I: System design and implementation," IEEE Trans. Geosci. Remote Sensing, 8(3), 1299 - 1325.

114. [114] Baraldi, A., Durieux, L., Simonetti, D., Conchedda, G., Holecz, F., & Blonda, P. (2010b). "Automatic spectral rule-based preliminary classification of radiometrically calibrated SPOT-4/-5/IRS, AVHRR/MSG, AATSR, IKONOS/QuickBird/OrbView/GeoEye and DMC/SPOT-1/-2 imagery – Part II: Classification accuracy assessment," IEEE Trans. Geosci. Remote Sensing, vol. 48, no. 3, pp. 1326 - 1354, March 2010.

115. [115] Goodchild, M. F., Yuan M., & Cova, T. J. (2007). Towards a general theory of geographic representation in GIS, International Journal of Geographical Information Science, 21:3, 239-260.

116. [116] Bernus P., and O. Noran. 2017. Data Rich – But Information Poor. In: Camarinha-Matos L., Afsarmanesh H., Fornasiero R. (eds) *Collaboration in a Data-Rich World*: PRO-VE 2017. IFIP Advances in Information and Communication Technology, 506: 206-214.

117. [117] European Union, Copernicus Observer - The upcoming Copernicus Data and Information Access Services (DIAS), 26/05/2017. Available online: http://copernicus.eu/news/upcoming-copernicus-data-and-information-access-services-dias (accessed on 15 July 2018).

118. [118] European Union, The DIAS: User-friendly Access to Copernicus Data and Information, June 2018. Available online: http://copernicus.eu/sites/default/files/Data_Access/Data_Access_PDF/Copernicus_DIAS_Factsheet_June2018.pd (accessed on 15 July 2018).

119. [119] Committee on Earth Observation Satellites (CEOS), 2018. CEOS Analysis Ready Data – CEOS Analysis Ready Data for Land (CARD4L) products. Available online: http://www.ceos.org/ard/ (accessed on 4 May 2018).

120. [120] U.S. Geological Survey (USGS), 2018b. U.S. Landsat Analysis Ready Data (ARD). Available online: https://landsat.usgs.gov/ard (accessed on 15 July 2018).

121. [121] U.S. Geological Survey (USGS), 2018a. U.S. LANDSAT ANALYSIS READY DATA (ARD) DATA FORMAT CONTROL BOOK (DFCB) Version 4.0, January 2018. Available online: https://landsat.usgs.gov/sites/default/files/documents/LSDS-1873_US_Landsat_ARD_DFCB.pdf (accessed on 15 July 2018).

2509 122. [122] Guoqing Zhou, Architecture of Future Intelligent Earth Observing Satellites (FIEOS) in 2010
2510   and Beyond, National Aeronautics and Space Administration Institute of Advanced Concepts
2511   (NASA-NIAC), Technical Report, 2001.
2512 123. [123] GISCafe News, Earth-i led consortium secures grant from UK Space Agency, July 19, 2018.
2513   Available   online:
2514   https://www10.giscafe.com/nbc/articles/view_article.php?section=CorpNews&articleid=1600936
2515   (accessed on 15 July 2018).
2516 124. [124] Vermote, E., and N. Saleous. 2007. "LEDAPS surface reflectance product description - Version
2517   2.0." University of Maryland at College Park /Dept Geography and NASA/GSFC Code 614.5
2518 125. [125] D. Riaño, E. Chuvieco, J. Salas, and I. Aguado, "Assessment of different topographic
2519   corrections in Landsat TM data for mapping vegetation types," IEEE Trans. Geosci. Remote Sens.,
2520   vol. 41, no. 5, pp. 1056–1061, May 2003.
2521 126. [126] C. Leprieur, J. M. Durand, and J. L. Peyron, "Influence of topography on forest reflectance
2522   using Landsat Thematic Mapper and digital terrain data," Photogramm. Eng. Remote Sens., vol. 54,
2523   pp. 491–496, 1988.
2524 127. [127] A. G. Thomson and C. Jones, "Effects of topography on radiance from upland vegetation in
2525   North Wales," Int. J. Remote Sens., vol. 11, pp. 829–840, 1990.
2526 128. [128] Bishop, M. P. & Colby, J. D. 2002. Anisotropic reflectance correction of SPOT-3 HRV imagery.
2527   Int. J. Remote Sens., 23(10), 2125-2131.
2528 129. [129] Bishop, M. P., Shroder, J. F., & Colby, J. D. 2003. Remote sensing and geomorphometry for
2529   studying relief production in high mountains," Geomorphology, 55(1–4), 345-361.
2530 130. [130] N. Hunt and S. Tyrrell, Stratified Sampling. Coventry University, 2012. [Online] Available:
2531   http://www.coventry.ac.uk/ec/~nhunt/meths/strati.html
2532 131. [131] T. Poggio, "The Levels of Understanding framework, revised," Computer Science and
2533   Artificial Intelligence Laboratory, Technical Report, MIT-CSAIL-TR-2012-014, CBCL-308, May 31,
2534   2012.
2535 132. [132] Q. Iqbal and J. K. Aggarwal, "Image retrieval via isotropic and anisotropic mappings," in Proc.
2536   IAPR Workshop Pattern Recognit. Inf. Syst., Setubal, Portugal, Jul. 2001, pp. 34–49.
2537 133. [133] Pessoa, L. (1996). Mach Bands: How Many Models are Possible? Recent Experimental Findings
2538   and Modeling Attempts. *Vision Res.*, 36(19), 3205–3227.
2539 134. [134] Baatz, M. & Schäpe, A. (2000). Multiresolution Segmentation: An Optimization Approach for
2540   High   Quality   Multi-Scale   Image   Segmentation.   In   Angewandte   Geographische
2541   Informationsverarbeitung XII; Strobl, J., Ed.; Herbert Wichmann Verlag: Berlin, Germany, 58, 12–
2542   23.
2543 135. [135] Espindola, G. M., Camara, G., Reis, I. A., Bins, L. S., & Monteiro, A. M. (2006). Parameter
2544   selection for region-growing image segmentation algorithms using spatial autocorrelation, Int. J.
2545   Remote Sens., 27(14), 3035–3040.
2546 136. [136] Canny, J. (1986). A computational approach to edge detection. *IEEE Trans. Pattern Anal. Mach.
2547   Intell.*, 8(6), 679–698.
2548 137. [137] U.S. Geological Survey (USGS), 2018c. Landsat Surface Reflectance Code (LaSRC) v1.2.0.
2549   Available   online: https://github.com/USGS-EROS/espa-surface-reflectance/tree/lasrc_v1.2.0/
2550   (accessed on 15 July 2018).
2551 138. [138] Baraldi, A., & Humber, M. (2015). Quality assessment of pre-classification maps generated
2552   from spaceborne/airborne multi-spectral images by the Satellite Image Automatic Mapper™ and
2553   Atmospheric/Topographic Correction™-Spectral Classification software products: Part 1 – Theory.
2554   *IEEE J. Sel. Topics Appl. Earth Observ. Remote Sens.*, 8(3), 1307-1329.
2555 139. [139] Baraldi, A., Humber, M., & Boschetti, L. (2013). Quality assessment of pre-classification maps
2556   generated from spaceborne/airborne multi-spectral images by the Satellite Image Automatic
2557   Mapper™ and Atmospheric/Topographic Correction™-Spectral Classification software products:
2558   Part 2 – Experimental results. *Remote Sens.*, 5, 5209-5264.
2559 140. [140] Burt, P. and Adelson, E. (1983). The laplacian pyramid as a compact image code. IEEE Trans.
2560   Commun. 31(4): 532–540.
2561 141. [141] Jain, A. & Healey, G. (1998). A multiscale representation including opponent color features for
2562   texture recognition. IEEE Trans. Image Process., 7, 124–128.

142. [142] Axios (2017), Artificial intelligence pioneer, Geoffrey Hinton, says we need to start over, Sept. 15, 2017. Date: 8 Jan. 2018. Available online: https://www.axios.com/artificial-intelligence-pioneer-says-we-need-to-start-over-1513305524-f619efbd-9db0-4947-a9b2-7a4c310a28fe.html

143. [143] Meer, P. (2012). Are we making real progress in computer vision today?, Image and Vision Computing, 30, 472–473.

144. [144] Nguyen, A., Yosinski, J., & Clune, J. (2014). Deep Neural Networks are Easily Fooled: High Confidence Predictions for Unrecognizable Images. arXiv: 1412.1897. Date: 8 Jan. 2018. Available online: https://arxiv.org/pdf/1412.1897.pdf

145. [145] Szegedy, C., Zaremba, W., Sutskever, I., Bruna, J., Erhan, D., Goodfellow, I., Fergus, R. (2013). Intriguing properties of neural networks. arXiv: 1312.6199. Date: 8 Jan. 2018. Available online: https://arxiv.org/pdf/1312.6199.pdf

146. [146] Bartoš, M. 2017. Cloud and Shadow Detection in Satellite Imagery. Master Thesis in Computer Vision and Image Processing, Faculty of Electrical Engineering, Department of Cybernetics, Czech Technical University in Prague.

147. [147] Martinetz, T., Berkovich, G., & Schulten, K. (1994). Topology representing networks. Neural Networks, 7(3), 507–522.

148. 148] Berlin, B., and P. Kay. 1969. "Basic color terms: their universality and evolution." Berkeley: University of California.

149. [149] Griffin, L. D. 2006. "Optimality of the basic color categories for classification." *J. R. Soc. Interface* 3: 71–85.

150. [150] Chavez, P. (1988). An improved dark-object subtraction technique for atmospheric scattering correction of multispectral data. *Remote Sens. Environ*. 24:459–479.

151. [151] Baraldi, A., V. Puzzolo, P. Blonda, L. Bruzzone, and C. Tarantino. (2006). Automatic spectral rule-based preliminary mapping of calibrated Landsat TM and ETM+ images. IEEE Trans. Geosci. Remote Sens. 44, p. 2563-2586.

152. [152] Adams, J. B., Donald, E. S., Kapos, V., Almeida Filho, R., Roberts, D. A., Smith, M. O., & Gillespie, A. R. (1995). Classification of multispectral images based on fractions of endmembers: Application to land-cover change in the Brazilian Amazon. Remote Sens. Environ. 52, 137-154.

153. [153] Kuzera, K., and R. G. Pontius jr. 2008. "Importance of matrix construction for multiple-resolution categorical map comparison." *GIScience and Remote Sens*. 45: 249–274.

154. [154] Pontius Jr., R.G., and J. Connors. 2006. "Expanding the conceptual, mathematical and practical methods for map comparison," in Caetano, M. and Painho, M. (Eds). Proceedings of the 7th International Symposium on Spatial Accuracy Assessment in Natural Resources and Environmental Sciences, Lisbon. Instituto Geográfico Português, 5 – 7 July 2006, 64-79.

155. [155] Stehman, S. V., and R L. Czaplewski. 1998. "Design and analysis for thematic map accuracy assessment: Fundamental principles." Remote Sens. Environ. 64: 331-344.

156. [156] Congalton, R. G., and K. Green. 1999. *Assessing the Accuracy of Remotely Sensed Data*. Boca Raton, FL, USA: Lewis Publishers.

157. [157] Lunetta, R., and D. Elvidge. 1999. *Remote Sensing Change Detection: Environmental Monitoring Methods and Applications*. London, UK: Taylor & Francis.

158. [158] Tyagi, V. (2017). Content-Based Image Retrieval Ideas, Influences, and Current Trends, Singapore: Springer.

159. [159] Nagao, M., & Matsuyama, T. (1980). *A Structural Analysis of Complex Aerial Photographs*. Plenum Press, New York.

160. [160] Shackelford, K., and C. H. Davis. 2003a. "A combined fuzzy pixel-based and object-based approach for classification of high-resolution multispectral data over urban areas, " IEEE Trans. Geosci. Remote Sens. 41(10): 2354 – 2363.

161. [161] Shackelford, K., and C. H. Davis. 2003b. "A hierarchical fuzzy classification approach for high-resolution multispectral data over urban areas," IEEE Trans. Geosci. Remote Sens. 41(10): 1920–1932.

162. [162] Wenwen Li, M. F. Goodchild and R. L. Church. 2013. "An efficient measure of compactness for 2D shapes and its application in regionalization problems." Int. J. of Geographical Info. Science 1-24.

163. [163] Andrea Baraldi, João V. B. Soares, "Multi-Objective Software Suite of Two-Dimensional Shape Descriptors for Object-Based Image Analysis," Subjects: Computer Vision and Pattern Recognition

(cs.CV), arXiv:1701.01941. Date: 8 Jan. 2017. [Online] Available: https://arxiv.org/ftp/arxiv/papers/1701/1701.01941.pdf

164. [164] Julesz, B. 1986. "Texton gradients: The texton theory revisited," in *Biomedical and Life Sciences Collection*, Springer, Berlin / Heidelberg, 54(4-5).

165. [165] Julesz, B., E. N. Gilbert, L. A. Shepp, and H. L. Frisch, 1973. "Inability of humans to discriminate between visual textures that agree in second-order statistics – revisited," *Perception* 2: 391-405.

166. [166] Yellott, J. (1993). Implications of triple correlation uniqueness for texture statistics and the Julesz conjecture. *Optical Society of America*, 10(5), 777-793.

167. [167] Zadeh, L.A. 1965. "Fuzzy sets," *Inform. Control* 8: 338–353.

168. [168] Open Geospatial Consortium (OGC) Inc. 2015. *OpenGIS® Implementation Standard for Geographic information - Simple feature access - Part 1: Common architecture*. Accessed 8 March 2015. http://www.opengeospatial.org/standards/is

169. [169] Shotton, J., Winn, J., Rother, C. and Criminisi, A. 2009. "Texton-Boost for Image Understanding: Multi-Class Object Recognition and Segmentation by Jointly Modeling Texture, Layout, and Context," Int. J. Comp. Vision. 81(1): 2–23.

170. [170] Wikipedia, 2018. Latent variable. Accessed 30 Jan. 2018. Available: https://en.wikipedia.org/wiki/Latent_variable.

171. [171] Gijsenij, A., Gevers, T., & van de Weijer, J. (2010). Computational color constancy: Survey and experiments. *IEEE Trans. Image Proc.*, 20(9), 2475-2489.

172. [172] Finlayson, G. D., Hordley, S. D., & Hubel, P. M. (2001). Color by correlation: A simple, unifying framework for color constancy. *IEEE Trans. Pattern Anal. Machine Intell.*, 23(11), 1209-1221.

173. [173] Gevers, T., Gijsenij, A., van de Weijer, J., & Geusebroek, J-M. (2012). *Color in Computer Vision*. Hoboken, New Jersey, USA: Wiley.

174. [174] Vo, A.-V., Truong-Hong, L., Laefer, D. F., Tiede, D., d'Oleire-Oltmanns, S., Baraldi, A., & Shimoni, M. (2016). Processing of extremely high resolution LiDAR and optical data: Outcome of the 2015 IEEE GRSS Data Fusion Contest. Part–B: 3D contest. *IEEE J. Selected Topics Applied Earth Obs. Remote Sens*. 9(12): 5560-5575.

175. [175] Baraldi, A., Tiede, D., & Lang, S. (2017b). Automated Linear-Time Detection and Quality Assessment of Superpixels in Uncalibrated True- or False-Color RGB Images. arXiv:1701.01940. Date: 8 Jan. 2017. [Online] Available: https://arxiv.org/ftp/arxiv/papers/1701/1701.01940.pdf

176. [176] Dillencourt, M. B., H. Samet, and M. Tamminen. 1992. "A general approach to connected component labeling for arbitrary image representations," *J. Association for Computing Machinery* 39: 253-280.

177. [177] Purdue University, 2018. Perceptual Grouping,. Available online: http://cs.iupui.edu/~tuceryan/research/ComputerVision/perceptual-grouping.html (accessed on 10 August 2018).

178. [178] Tiede, D., (2014). A new geospatial overlay method for the analysis and visualization of spatial change patterns using object-oriented data modeling concepts. Cartography and Geographic Information Science, 41(3), p.227–234. http://dx.doi.org/10.1080/15230406.2014.901900

179. [179] Trimble (2015). eCognition® Developer 9.0 Reference Book.

180. [180] Group on Earth Observation / Committee on Earth Observation Satellites (GEO-CEOS) - Working Group on Calibration and Validation (WGCV). 2015. *Land Product Validation* (LPV). Accessed March 20, 2015. http://lpvs.gsfc.nasa.gov/

181. [181] Slotnick, S. D., Thompson, W. L., & Kosslyn, S. M. (2005). Visual mental imagery induces retinotopically organized activation of early visual areas, *Cerebral Cortex*, 15, 1570-1583.